Double differential IVLEED spectra of HOPG

Philipp Ziegler

September 1, 2022

1 Abstract

Over the past few decades the interest in quasi two dimensional Van der Waals materials such as highly oriented pyrolytic graphite (HOPG) increased significantly, especially the electronic structure is of great interest for many applications. This work aims to investigate the unoccupied band structure above the vacuum level of HOPG by means of double differential inelastic very low energy electron diffraction (IVLEED) measurements in the energy range of 0 to 200eV primary energy in 30° and 60° specular reflection geometry. This allows to study the band structure with elastically and inelastically back scattered primary electrons as well as measuring the secondary electron emission. Using the matching formalism, a correlation between the elastic peak intensities and the band structure was established. The link with inelastic intensities provides a qualitative description of the penetration depth of the primary electrons in the crystal. The acquired IVLEED data revealed the existence of a novel and atypical feature, in which primary electrons occupy a preferred final state, resulting in the emission of electrons with fixed energy. Two kinetic models for inelastic diffraction of electrons on crystals have been implemented, in which the sequence of inelastic and elastic diffraction lead to Bragg peaks at different energies. The results are in good agreement with quantum field theory models and experimental data for high energies [1–5].

Contents

2 Introduction

Over the past few decades and especially after the discovery of graphene in 2004, the interest in quasi two-dimensional Van der Waals (VdW) materials such as highly oriented pyrolytic graphite (HOPG) increased vastly. The possible applications range from microelectronic devices, material science, applied chemistry and medicine to biology. A quasi 2D VdW material consists of stacked atomic layers, which are bound by weak Van der Waals forces. This results in a high symmetry along the c-axis of the crystal, which allows one to reduce the dimensionality of the investigated system [6].

The electronic band structure of a material is of vital interest regarding its potential applications. It provides information about the allowed energies that electrons can have within the crystal and thus which electronic transitions are allowed. This allows for an understanding, for instance, of the electrical resistance, superconductivity, molecular adsorption and optical absorption processes. The band structure also provides the foundation for solid state devices like transitors, optoelectronics and solar cells. This work is dedicated to the investigation of the unoccupied band structure above the vacuum level of HOPG. For this purpose, inelastic very low energy electron diffraction (IVLEED) experiments were performed in the energy range up to 200eV in two geometries. The data were collected at the secondary electron energy loss coincidence spectrometer (SE2ELCS) at the Technical University Vienna.

The main goal of this work is to investigate the unoccupied band structure above the vacuum level. The investigation is based on a theoretical treatment and on experimentally collected data. The theoretical analysis includes in chapter 3.1 the matching formalism, which describes how the wave functions of incoming electrons couple with allowed Bloch wave functions inside the crystal. Essentially, Bloch states must exist in the solid whose Fourier coefficients match the Fourier coefficients of the incoming particles. If not, in a first approximation, the electrons cannot penetrate the solid. By including higher order approximations, it is shown that electrons can indeed penetrate the solid, but their wave function is exponentially damped in the solid. Chapter 3.3 deals with the diffraction phenomena of electrons that are inelastically as well as elastically scattered. Two kinetic models were created in which the primary electron is assumed to be scattered either elastically or inelastically first and followed by the opposite type of scattering. These models describe the expected positions of Bragg peaks for primary electrons that suffer energy loss in the

4

solid. Good agreement is found with theoretical and experimental studies at high primary energies [1–5]. Furthermore, in chapter 4.2 the influence of the electron source on the energy scale in experiments is demonstrated [7–14]. It was found that the work function differneces between two surfaces and the electron generation processes can severely change the energy scale of reference by up to 1eV and therefore, it is not negligible especially in the study of very low energy electrons (VLEE).

The experimental data in this work were collected with a time-of-flight (TOF) analyser in 30° specular reflection geometry and with a hemispherical mirror analyser (HMA) in 60° specular reflection geometry, respectively. In each case, full range energy spectra were measured at landing energies between 3 and 200eV. The TOF analyser achieves a high energy resolution for low-energy electrons. The HMA provides a constant energy resolution in the full energy range, which enables one to investigate discrete energy losses, for instance, energy losses caused by the excitation of plasmons. In chapter 5.2 the intensity of the elastic peak is interpreted with the matching formalism. This allows one to determine areas in the band structure in which primary electrons cannot penetrate the solid surface. Furthermore, it is shown by using single reflected electron energy loss spectra (REELS) that electrons can also penetrate into forbidden regions of the band structure (i.e. band gaps), but are strongly damped. In chapter 5.3 the double differential inelastic very low energy electron diffraction (IVLEED) spectra are analysed and discussed. In particular, a qualitative description of the penetration depth of primary electrons into different regions of the band structure and the secondary electron emission are discussed.

3 Theory

3.1 General considerations

Since the discovery of the electron in 1897 by Joseph John Thomson, the interest in beams of electrons remained high. In the past century, electron beams (EBs) played a vital role in many areas of scientific and daily life. For example, the electron tube radio receivers (invented in 1924) and the tube television (black-white TV invented 1926) rapidly established themselves in many households. With the invention of the electron microscope in 1931 it was possible to achieve better resolution by orders of magnitude than with regular light microscopes [15]. Nowadays, beams of electrons are used in countless

technical, analytical, and medical applications. On an industrial scale, EBs are used, for instance, to produce high-purity metals and in some cases exotic alloys in electron beam furnaces. In the semiconductor sector, EBs are used to create fine structures in wafer disks by means of lithography. Medical applications are the sterilisation of health-care products or the treatment of cancer using small electron accelerators (linacs) [16]. EBs are an excellent tool for many analytical techniques. Their properties, such as energy, direction, intensity, and beam-diameter, are easily manipulated and controlled, since charged particles can be controlled by electromagnetic fields. Due to the small penetration depth of slow electrons, they can be used to study the electronic and crystalline structure near the surface and hence, are used in this work to study the surface of a graphite sample.

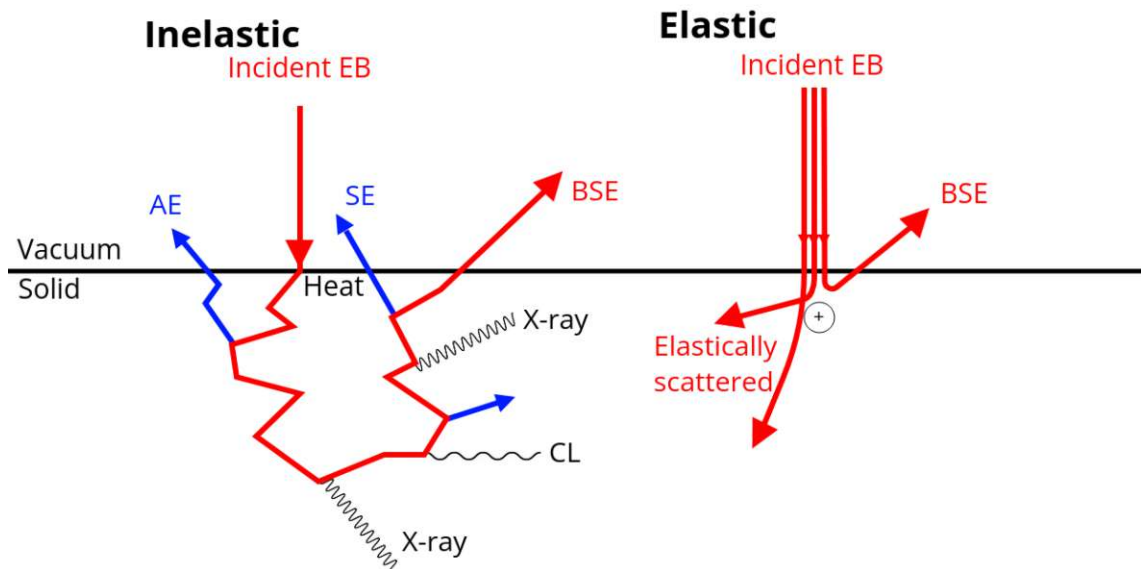The bombardment of surfaces with electron beams gives rise to some particles

Figure 1: Electron beam trajectories and interaction mechanisms of inelastically (left) and elastically scattered electrons. The left side shows an example trajectory of an incoming electron, while undergoing a sequence of elastic an inelastic collisions. It should be noted that Auger electrons (AE) and secondary electrons (SE)can only leave the target in the outermost few atomic layers. The deeper in the solid such an electron was generated, the less likely it is to still have sufficient energy on its way to the surface to overcome the surface barrier. The unlabeled blue arrow designates such an electron. Inelastic collisions can also lead to the generation of characteristic x-ray radiation via x-ray fluorescence or cathodoluminescence (CL). The right side schematically illustrates the elastic scattering on a single atom.

of the beam to transmit through, to scatter back from or to be absorbed within the solid. Inside the solid, impinging electrons interact with the nuclei and
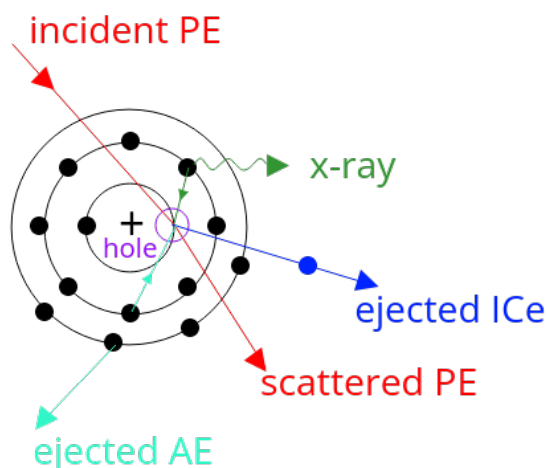
Figure 2: Process of excitation of an inner-shell electron. A primary electron(red) excites an inner-core electron (blue) and the vacancy can be reoccupied by two competing effects: x-ray fluorescence (green) or Auger-Meitner effect, as explained in the main text.

atomic and solid state electrons via a sequence of elastic and inelastic collisions, as seen in figure 1. In an elastic collision, the electron will be scattered on the electrostatic potential of the screened positively charged nuclei. The energy transfer from the electron to the nucleus can be neglected, since the mass of an electron is atleast three to four orders of magnitudes smaller than the mass of the nucleus. However, elastic collisions give rise to large directional changes of the impinging electrons [17]. In single crystals, elastic scattering on the lattice causes the creation of constructive interference patterns, a phenomenon known as Bragg scattering. Inelastic collisions cause a transfer of energy and momentum from the impinging electron to the collision partner. Figure 2 shows the process of such collisions. First, an incoming primary electron (red) liberates an inner-shell electron (blue), leaving an inner-shell hole (purple) behind. Now, the vacancy can be reoccupied by a higher shell electron in two competing ways, the emission of a characteristic x-ray photon (green) or the emission of an Auger electron (AE) (cyan). In the first case, the energy difference $\hbar\omega = E_2 - E_1$ between the inner (1) and outer (2) shell determines the energy of the photon. Within the Auger-Meitner effect[1], the released energy is not transferred to a photon, but to a third bound electron, which will then escape from the atom. Solid state electron can acquire energy through inelastic collisions with primary electrons. If the energy is sufficient to overcome the surface barrier, the solid state electron can leave the target as secondary electron (SE). However, if the energy of the solid state electron is too low, it will remain inside the solid as a so called hot electron. A

---

[1]The effect is named after Lise Meitner and Pierre Victor Auger. Although this effect was first discovered by Meitner, most of the credit was given to Auger. Only in more recent publications does Meitner also receive some of her deserved recognition.

further possibility for the incoming primary electron to interact with the solid is the excitation of plasmons. When a charged particle enters a solid, it attracts oppositely charged particles and repels equally charged ones. This results in a displacement of the charge carriers in relation to each other. The repulsive force causes oscillations in the charge density with associated quasi-particles called plasmons. In the case of incoming electrons, the plasmons can thus be seen as a collective oscillation of the solid state electrons. Most of the energy of the incoming electron is eventually lost in the form of phonons and heat in a cascade of inelastic collisions [18]. Because of strong inelastic scattering, the inelastic mean free path of low energy electrons ($E < 10keV$) is only in the order of the atomic spacing in crystals. Therefore, the penetration depth of electron beams in this energy range is only a few atomic layers and hence, EB's are highly sensitive to the surface properties

In the following section, several analytical techniques will be presented.

Low energy electron diffraction

The wave-particle dualism is one of the most important theories in modern physics. Its founder is Louis de Broglie, who in his dissertation in 1924 postulated that electrons are particle waves with a wavelength $\lambda = \frac{p}{h}$, where p is their momentum and h is Planck's constant. Only three years later, in 1927, Clinton Davison and Lester Halbert Germer confirmed his hypothesis by measuring different electron diffraction patterns of poly-crystalline nickel with and without an oxide layer. In such experiments, an electron beam is focused on the surface of a crystal. The acquired intensity of the elastically scattered electrons measured as a function of the incident energy is referred to as the (elastic) IV-curve. In the following, the diffraction of electrons in the energy range of a few 100eV to keV will be briefly discussed. The measurement of the IV curve is also known as low-energy electron diffraction (LEED). Due to the small penetration depth of only a few atomic layers in this energy range, this technique is very sensitive to the chemical and crystalline composition of the surface [19]. As so often in scientific history, the discovery of Davison and Germer was based on an accident. They measured a change in the IV curve, since an oxide layer formed on the nickel surface. This was caused by a leak in the vacuum chamber. [20].

From interference studies of crystals with X-rays, it is known that constructive interference occurs when the path difference between two waves is an n-fold multiple of the wavelength λ. Figure 3 shows that the path difference of a
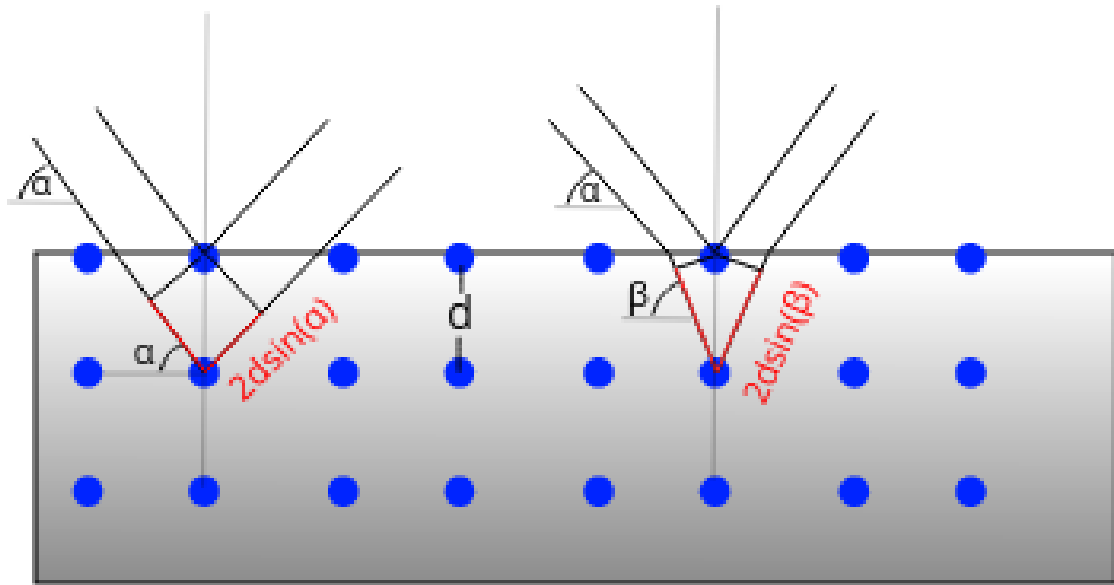
Figure 3: Illustration of scattering of x-rays (left) and electrons (right) from a crystalline surface. While photons of sufficient energy are not refracted at the vacuum-solid interface, electrons feel the inner potential and change their perpendicular component of the momentum.

diffracted wave corresponds to the well-known Bragg condition for constructive interference $2dsin(\alpha) = n\lambda$. Because of the wave character of electrons, it was expected that they would also follow Bragg's condition. However, numerous experiments in the late 1920s showed this was not the case, but that the diffraction maxima were shifted towards lower energies. In 1928, Hans Albrecht Bethe solved this issue by introducing an electrostatic potential energy step between vacuum and the inside of a crystal [21]. According to Schrödinger's equation, electrons change their momentum when they travel through areas with different potentials. This means the momentum shifts when penetrating the surface of the crystal. Bethe called the potential difference between vacuum and solid inner potential U_i with values of the order of the valence band width (~15eV). LEED is a well-established technique to study the inner potential. Chapter 3.2 deals with this topic in more detail.

Very low energy electron diffraction

For energies in the range of 1-100eV, one speaks of very low energy electron diffraction (VLEED). With VLEED, the kinematic models used in LEED lose their applicability and quantum mechanical effects, such as the band structure of the target, must be considered. VLEED measurements provide information about the allowed and forbidden states in the unoccupied band structure. A section later in this chapter deals with the band structure of graphite in more detail.

9

Very low energy electron diffraction is a well-established technique to investigate the electronic structure $E(\vec{k})$ above the vacuum level and is usually done at perpendicular incidence angle of the electron beam. Elastically scattered electrons are used to create a link between the wave functions in vacuum and the Bloch wave functions in a crystalline solid [22–24]. Schrödinger's equation describes particles in vacuum as plane waves and in periodic potential wells as Bloch waves. Therefore, penetrating the surface changes the wave function of electrons. An impinging free electron enters the target as a plane wave and is forced to adapt a Bloch state in the solid and vice versa, for secondary electrons. This is also called coupling of the wave functions and is described by the matching formalism.

Matching formalism

The matching formalism is a simple and straight-forward method for creating a causal link between the band structure and the elastic reflectivity of an electron beam. It uses the fact that free electrons in vacuum are described as plane waves and in periodic crystalline potentials as Bloch waves. Both wave functions must satisfy certain boundary conditions at the solid-vacuum interface for an external electron to be allowed to enter the solid. The following derivation is based on the text book "Solid Surfaces, Interfaces and Thin Films" written by Hans Lüth [25].

In the simplest case, a surface can be described by a step-like potential barrier, where the space is divided into two sections: $z < 0$, the vacuum half space and, $z > 0$, the crystal half space consisting of a semi-infinite periodic potential. An incident electron beam is refracted at the potential barrier changing its momentum, as shown in figure 4. However, the total particle current I is conserved at the transition from vacuum into the solid (primed variables):

$$I = I' \quad , \quad \vec{j}A = \vec{j}'A \quad , \tag{1}$$

where A is the area of the beam and $\vec{j}$ is the particle density. The quantum mechanical probability flux can be written as

$$\vec{j} = \frac{\hbar}{2im}(\psi^* \nabla \psi - \psi \nabla \psi^*). \tag{2}$$
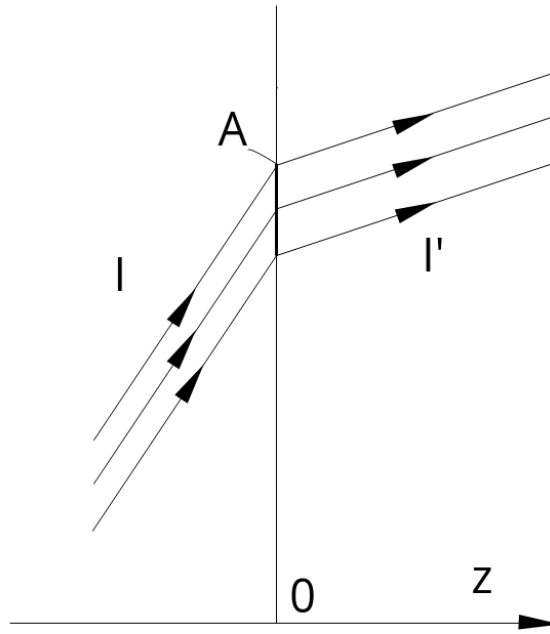
Figure 4: Illustration of a plane wave hitting the interface to a crystal at $z = 0$. The momentum changes in presence of the inner potential. The total electron flux remains conserved at this transition.[25]

By combining both equations, the boundary and continuity conditions for the wave functions ψ_{vac} and ψ_{sol} in vacuum and in the solid are obtained:

$$\psi_{vac}(z = 0) = \psi_{sol}(z = 0) \tag{3a}$$

$$\frac{\partial}{\partial n}\psi_{vac}(z = 0) = \frac{\partial}{\partial n}\psi_{sol}(z = 0) \quad . \tag{3b}$$

In the next step, the wave functions ψ_{vac} and ψ_{sol} still have to be characterised. An incoming primary electron can be described as a plane wave with the energy $E = \frac{\hbar^2}{2m}$ and the mass m as follows

$$\phi_{vac} = e^{i(\vec{k}_\parallel \cdot \vec{r}_\parallel + k_\perp z)}, \tag{4}$$

where the $\parallel$ components are in the (x, y) plane and $k_\perp$ points in the z direction. The wave function in a vacuum consists of both the incoming wave ϕ_{vac} as well as the diffracted waves. For the diffracted waves, the 2D periodicity of the surface potential can be employed. This conserves $k_\parallel$ within the reciprocal vector $\vec{G}_\parallel = \vec{G}_{hk} = h\vec{b}_1 + k\vec{b}_2$, where $\vec{b}_1$ and $\vec{b}_2$ are the reciprocal lattice vectors parallel to the surface and h, k the Miller indices. The total wave function in the vacuum reads:

$$\psi_{vac} = \phi_{vac} + \sum_{hk} A_{hk} e^{i((\vec{k}_\parallel + \vec{G}_{hk}) \cdot \vec{r}_\parallel - k_{\perp,hk} z)} \tag{5}$$

11

where A_{hk} is the amplitude of the scattered waves. From the conservation of energy

$$E = \frac{\hbar^2}{2m}(|\vec{k}_{\parallel} + \vec{G}_{hk}|^2 + k^2_{\perp,hk}),$$ (6)

the components of the wave vector can be obtained. Within the solid, the wave functions of the electrons are described as Bloch waves, which represent solutions of Schrödinger's equation in a periodic potential

$$V(\vec{r}) = \sum_{\vec{G}} V_G e^{i\vec{G}\vec{r}} \quad .$$ (7)

Thereby, $V_{\vec{G}}$ are the Fourier coefficients of the potential and $\vec{G}$ is a reciprocal lattice vector. The Bloch waves are plane waves modulated by a function $u(\vec{r})$, where u has the same periodicity as the potential. This gives the wave function of the electron inside the crystal:

$$\psi_{sol} = u_{\vec{k}}(\vec{r})e^{\vec{k}\cdot\vec{r}} = \sum_{\vec{G}} c_{\vec{G}}(\vec{k})e^{(i((\vec{k}+\vec{G})\cdot\vec{r}))},$$ (8)

where $c_{\vec{G}}(\vec{k})$ are the Fourier components of $u_{\vec{k}}(\vec{r})$.

The matching conditions of equation (3) for the wave functions (equation 5 & 8) show that the external electron with primary energy E can only enter the solid, if allowed electronic states exist in the crystal at this energy. Moreover, the match in Fourier components of the Bloch states with the incoming wave determines how well an electronic state couples with vacuum. Essentially, Bloch states must exist whose Fourier coefficients correspond to those of the incoming electron. At this point, the assumption that an incoming particle represents a plane wave can be dropped and generally replaced by a wave packet. Solid states electrons in well-coupling states can more easily leave the solid and external electrons can easily penetrate the into the target in such states. Primary electrons in well-coupling states can travel far into the solid and therefore have a high probability of undergoing inelastic scattering, resulting in a low elastic reflectivity. However, Slater suggested that the surface barrier can also be a complex quantity. The real part of the inner potential causes refraction of electrons on the surface and the imaginary part causes expoential wave damping, similar to Lambert-Beer's law.

In quasi 2 dimensional (2D) Van der Waals (VdW) materials like graphite, electrons can occupy a unique state, the so-called interlayer state. An interlayer state can be understood as a quasifree electron constantly bouncing between

adjacent layers. Therefore, the electron will be reflected on and transmitted through the lattice planes, similar to light in a Fábry-Perot interferometer. Recently, simulations of n-layered graphene (*n* refers to the number atomic layers) were performed by Geelen et al. and Ziegler to create a link between the reflectivity of elastically back scattered electrons and the interlayer states [26, 27]. The results of the simulation by Ziegler are shown in figure 5, where the interlayer states produce n-1 resonances in the reflectivity. Each added layer reduces the waviness of the curve, yielding a smooth curve for macroscopic samples (*n* > 100). The Fourier components of an interlayer state are similar to those of free charged particles, since the electrons can travel quasifreely through the lattice planes. If the energy of the primary electron coincides with a band
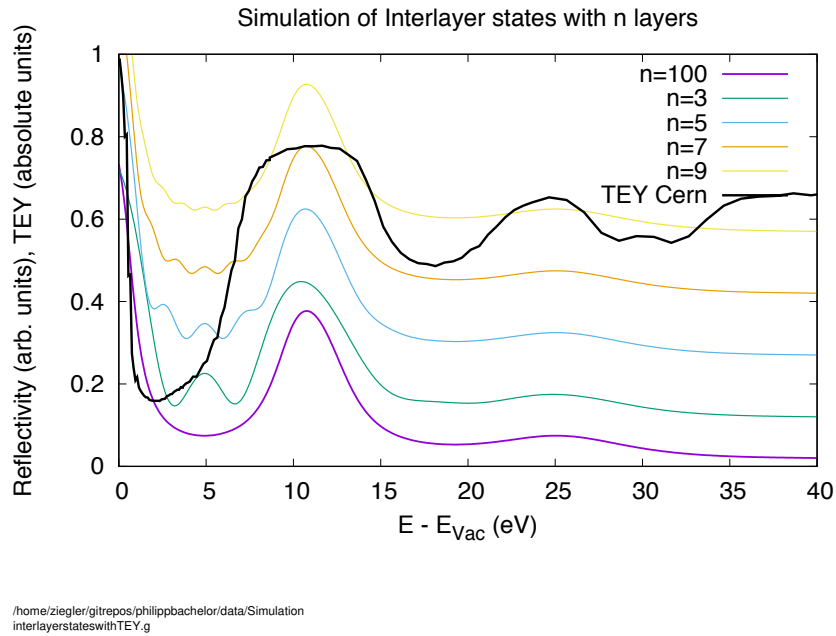

/home/ziegler/gitrepos/philippbachelor/data/Simulation
interlayerstateswithTEY.g

Figure 5: Simulation for the reflectivity of n-layered graphene as presented in [26, 27] compared to the total electron yield (TEY) curve from A. Bellissimo [28, 29] (TEY curves are discussed in the following section). For n-layered graphene, n-1 nodes are formed. This highlights, that electrons in an interlayer state act similar to light in a Fábry-Perot interferometer. Each added layer reduces the waviness of the curve, leading to a smooth curve for thick samples (e.g. *n*=100).

gap, the wave functions can no longer be matched, as no Bloch states are available in forbidden areas. As a consequence, external electrons cannot enter the solid at all, resulting in a high reflectivity. According to aforementioned matching formalism, in I-V measurements, band gaps are characterised by a reflectivity of about unity. By extending the assumption that the interface transitions from a semi-infinite crystal to vacuum in a step function, and moving to a more realistic

representation with a surface layer, one obtains states localised at the surface whose wave functions decrease exponentially into the crystal. The external electron can couple with the surface state, resulting in an exponential damping of the wave function of the primary electron. This behaviour is characterised by a complex $\vec{k}$ and a complex surface potential. Such electron wave damping was first described by John Clarke Slater in 1937 and has since been widely adapted in the literature, for instance in [25, 30–34]. For the I-V measurements, the presence of these surface states means that electrons can indeed penetrate the crystal, but are strongly damped. The reflectivity in a band gap is therefore expected to be less than unity. The small but finite penetration depth of the electrons is characterised by the imaginary part of the perpendicular component of the wave vector $\text{Im}(k_\perp)$.

3.1.1 Electron yield

For many applications, the secondary electron yield (SEY) δ_{SE} is of paramount importance, as it describes the total amount of SE generated per impacting primary particle. For instance, a high SEY (greater than 1) is desirable in particle detectors, such as in photo multipliers, where a series of dynodes lead to a cascading increase in signal strength . In contrast, a SEY much less than one is sought after in many applications where secondary electrons are seen as an undesired effect. For example, the accelerator walls of the large hadron collider (LHC) at CERN must be coated with a material with low SEY ($\delta_{SE} < 1$) to avoid the generation of an electron cloud because of the synchrotron radiation. Therefore, controlling SE emission materials is an active area of research, especially in view of the imminent launch of the LHC's high-luminosity mode [35]. In addition to the SEY, i.e., the amount of SE generated per incident particle, the energy distribution of the emitted SE $j_{SE}(E)$ is also of interest.

Both quantities just mentioned are frequently modeled via Monte-Carlo calculations. Especially in the medium and high energy ranges ($E >$ few keV to 100keV) there is a reasonable agreement between theoretical and experimental values. However, most theories and models fail in the low energy regime because they are mostly based on the particle character of electrons only while neglecting the wave character [29]. Moreover, in this energy range the band structure of the target becomes crucial for the reflectivity and transmittivity of impinging electrons.

From a technical point of view, measurements of both δ_{SE} and $j_{SE}(E)$ are very difficult, as it is impossible to experimentally distinguish properly between SE
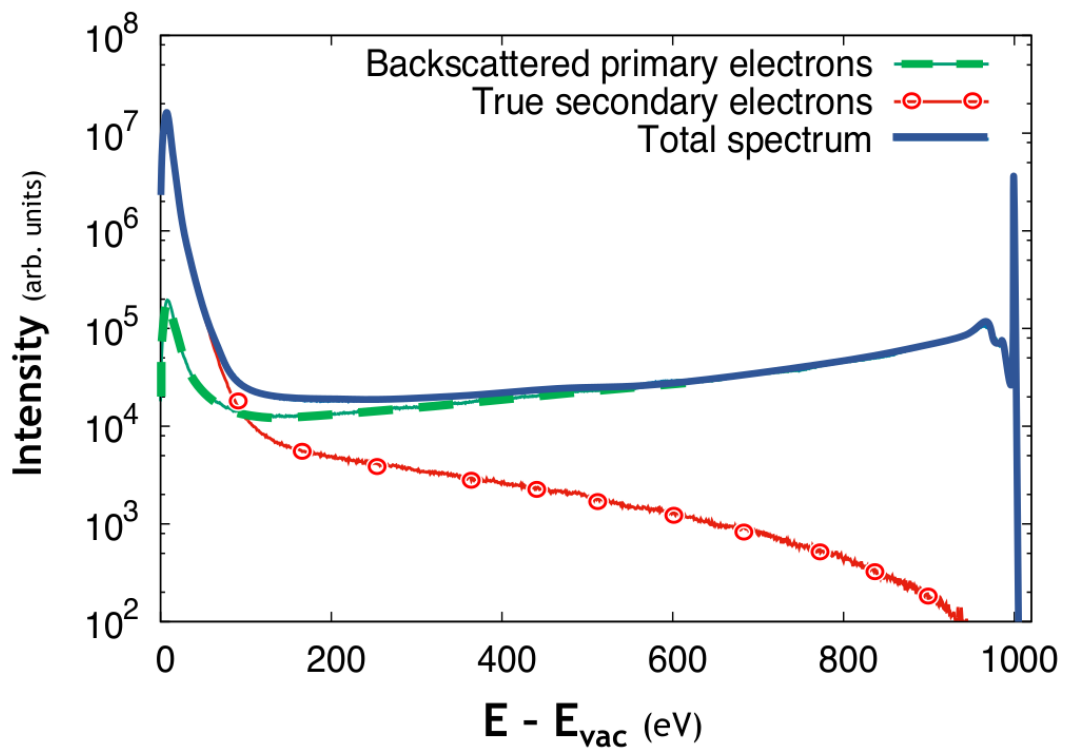
Figure 6: Simulation of an electron energy spectrum for a polycrystalline gold surface with a primary energy of 1keV. This simulation is based on a Monte Carlo calculation by Werner [36, 37]. The blue curve is the sum of the (elastic and inelastic) backscattered primary electrons and secondary electrons[29].

and PE in the acquired spectra, as shown in figure 6. However, what can be measured is the total electron yield (TEY), which is the sum of the emitted secondary electrons and the reflected electrons (RE) per impinging particle: $\delta_T = \delta_{SE} + \delta_{RE}$. For energies lower than 50eV, the TEY consists mostly of primary backscattered electrons, since the energy of the PE is not sufficient to emit SE in substantial amounts. The TEY in the energy range E <50eV is highly influenced by the band structure of the target and hence, can be used to study it.

3.1.2 Band structure of graphite

In a single atom, electrons can only occupy certain Eigenstates with discrete energy levels. For molecules with N atoms, each atomic energy level splits into N molecular energy levels. In macroscopic solids with $N = 10^{23}$ atoms, it leads to 10^{23} energy levels, which are so close together that one can speak of a continuous energy band. These bands thus provide information about the states that an electron is to allowed occupy in the solid. The representation of the allowed states in momentum space is called dispersion relation $E(k)$ or band structure.
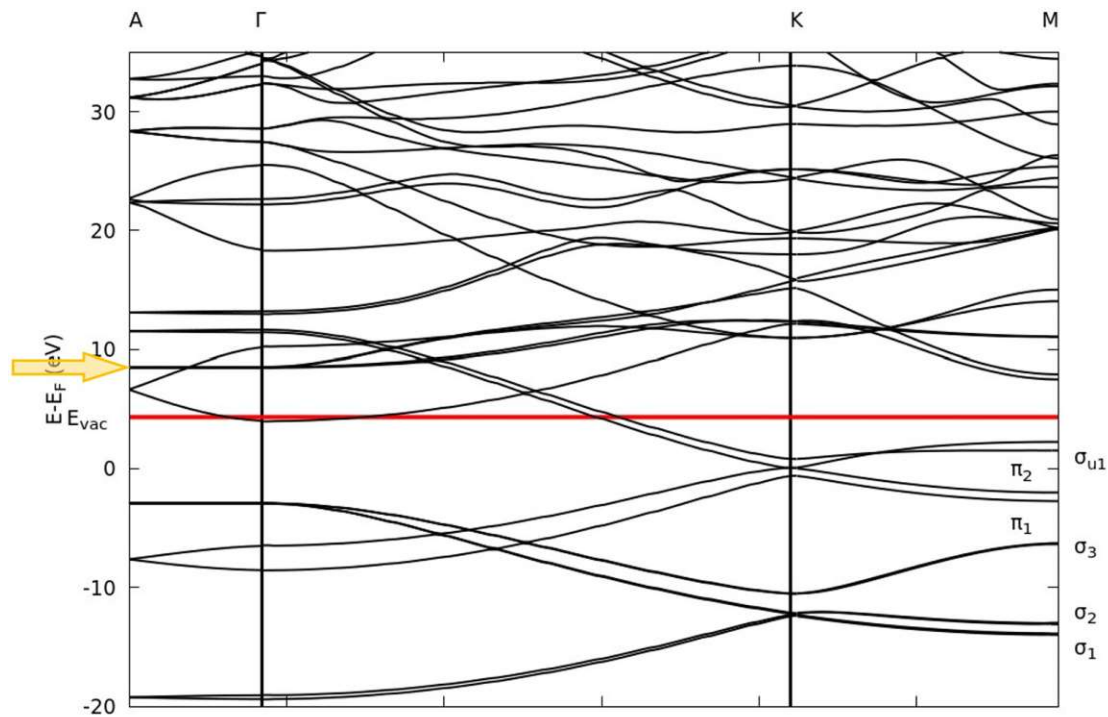

Figure 7: Band structure of highly oriented pyrolytic graphite (HOPG) along the main crystalline directions (see figure 22b) calculated by Riccardi using DFT[38].

The band structure of highly oriented pyrolytic graphite (HOPG) is shown in figures 7 and 8. This band structure is calculated by Pierfrancesco Riccardi et al. using density functional theory (DFT) based on the local density approximation for the exchange and correlation part of the Hamiltonian. This approach is
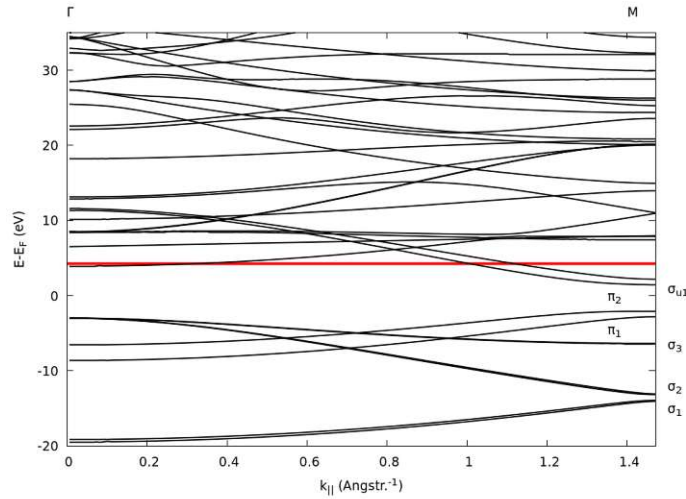
Figure 8: Band structure of highly oriented pyrolytic graphite (HOPG) along the ΓM direction (see figure 22b) calculated by Riccardi using DFT[38].

considered as the current state of the art. The horizontal red line indicates the vacuum level of HOPG and is located at $E - E_F = \phi = 4.6$eV, where ϕ is the work function. From the shape of the individual bands one can infer their properties. For example, the first derivative of a band relates to the mobility, and the second derivative relates to the effective mass of the electrons. The effective mass is a semi-classical model that describes the effect of external forces on electrons inside the crystal. Heavy electrons are strongly bound to the cores and therefore have low mobility and vice versa for light electrons.

The yellow arrows in figure 7 indicate the overlap of a broad interlayer band and a flat atom-like band in the ΓA region at about $E - E_{Vac} = 3.7$eV. From the previous considerations, it follows for the interlayer band that it has a high mobility and a low effective mass. Thus, electrons in such bands can move almost freely along the ΓA direction, i.e. between the atomic layers of graphite. In contrast, the atom-like band is very flat and thus has hardly any dispersion. Electrons in such a state have only discrete allowed energies, similar to electrons in single atoms.

3.2 The surface barrier

In order to understand the kinematics at the vacuum-solid interface, one must first consider the different energy levels in a solid. Figure 9 schematically shows a model energy level diagram of a metal at the vacuum-solid interface. Low energy electrons with discrete energies $\epsilon_0, \epsilon_1, ...$ are bound to their nucleus and strongly localised close to the core. Thus, they do not interact with electrons from neighbouring atoms. At higher energies, the discrete energy levels start
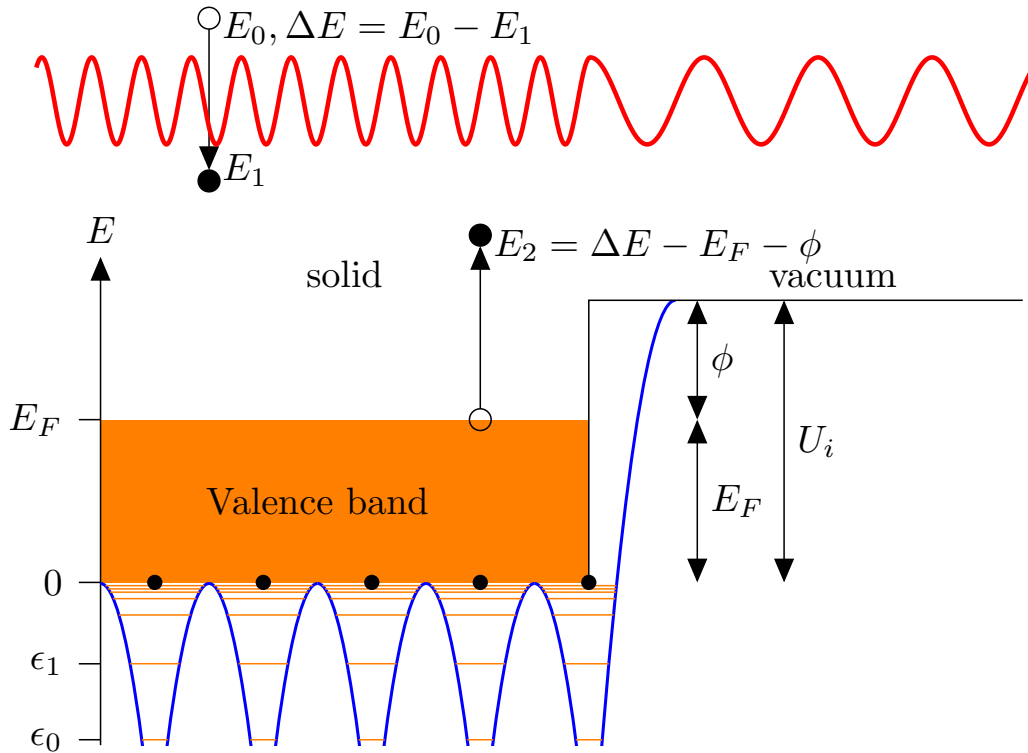
Figure 9: Energy level diagram of a metal close to the vacuum-solid interface defining the inner potential U_i. The red wave indicates different wavelengths inside and outside the solid. Orange: allowed electron states. Blue: overlapping core potentials, resulting in the work function on the outermost layer. An impinging primary electron with energy E_0 transfers ΔE to a bound solid state electron and leaves the solid with $E_1 = E_0 - \Delta E$. The bound solid state electron has the energy $E_2 = \Delta E - E_f - \phi$ after the energy transfer. Originally published in [39].

to form a continuum, where electrons interact with each other. Due to the nature of fermions, each state will be occupied by two electrons (one spin up and one spin down), starting from the lowest energy ϵ_0. At temperature $0K$, the energy of the highest occupied state will be referred to as Fermi energy E_F. According to Schrödinger's equation and as indicated by figure 9, the energy and momentum of an incoming electron wave changes on the vacuum-solid interface, influenced by the potential energy step U_i between the vacuum potential and the mean core potential. U_i is referred to as the inner potential and is defined by the constant $U_i = E_F + \Phi$, where Φ is the work function of the solid. This is a conventional definition, used in many surface science and solid state science studies. In general, the inner potential is by no means such a trivial quantity, since many factors, e.g. the exchange correlation between the electrons, need to be considered as well. However, for many applications and for this work, it is sufficient to treat U_i as a constant. When entering the solid, the energy of an electron is increased by the inner potential. Its energy and momentum in vacuum (v) and in the solid (s) are given by:

$$E_s = E_v + U_i \tag{9a}$$

$$|\vec{k_s}| = \sqrt{2(E_v + U_i)} \quad , \tag{9b}$$

when atomic units are used. Since the parallel component of the momentum is conserved[2] during the penetration of the surface barrier, the perpendicular component changes, resulting in a change of direction. Figure 10 shows a trajectory of an incoming electron with $\vec{k_v}, E_v$ at the transition, highlighting the change in direction. This transition is in analogy to the behavior of light following Snell's law. In the following derivation, it will be shown, that Snell's law also applies for electrons, however, in a slightly different manner.

Assuming an incoming electron with energy E_v and momentum $\vec{k_v}$ in vacuum:

$$\vec{k_v} = \begin{pmatrix} k_{v,\parallel} \\ k_{v,\perp} \end{pmatrix} = |\vec{k_v}| \begin{pmatrix} \sin(\alpha) \\ \cos(\alpha) \end{pmatrix} \tag{10a}$$

$$|\vec{k_v}| = \sqrt{2E_v} \tag{10b}$$

hits the surface of the crystal under an incident polar angle α with respect to the surface normal. Now the electron experiences the presence of the inner potential

---

[2]This fact can be understood with Noethers theorem, named after Amalie Emmy Noether : each symmetry corresponds to a conserved quantity. Since it does not matter where exactly the electron hits the surface, a translation symmetry exists parallel to the surface. As a result, the parallel component of the momentum is conserved.
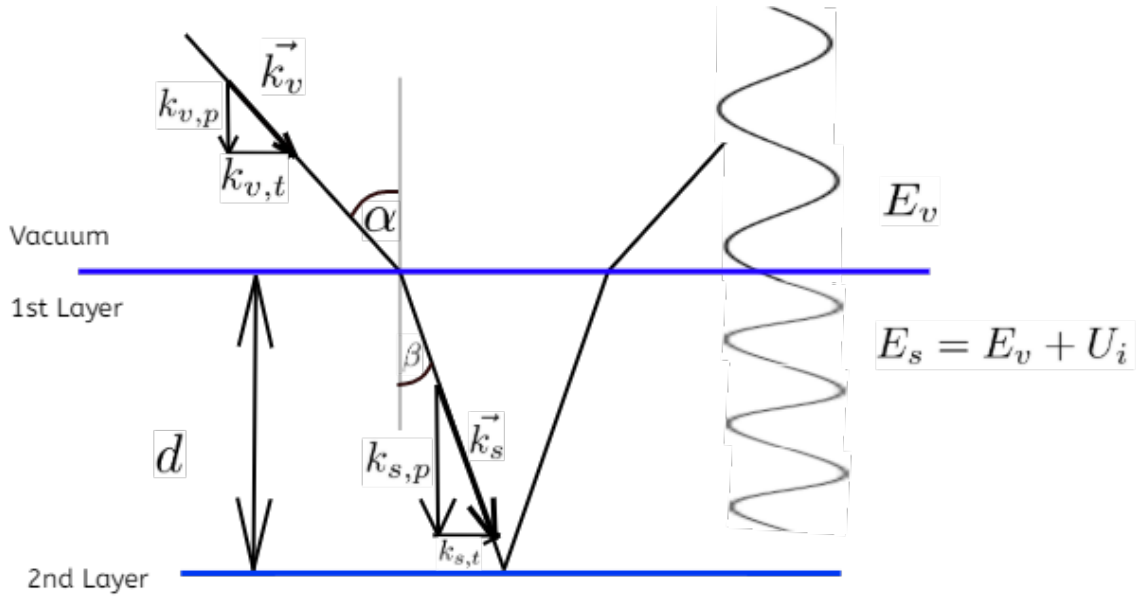
Figure 10: Schematic trajectory of an incoming electron, impacting under the polar angle α w.r.t. the surface normal. Note that the terminology is given for light waves, where the transversal (t) component refers to parallel component of the momentum for electrons. Originally published in [27].

U_i and changes its momentum and energy to:

$$E_s = E_v + U_i \tag{11a}$$

$$\vec{k_s} = \begin{pmatrix} k_{s,\parallel} \\ k_{s,\perp} \end{pmatrix} = |\vec{k_s}| \begin{pmatrix} \sin(\beta) \\ \cos(\beta) \end{pmatrix} \tag{11b}$$

$$|\vec{k_s}| = \sqrt{2E_s} \, . \tag{11c}$$

Since parallel component of the momentum is conserved during this transition, $k_{s,\parallel} = k_{v,\parallel}$. Snell's law for electrons can be derived:

$$|\vec{k_s}| \sin(\beta) = |\vec{k_v}| \sin(\alpha) \tag{12a}$$

$$\frac{\sin(\alpha)}{\sin(\beta)} = \frac{|\vec{k_s}|}{|\vec{k_v}|} = \sqrt{\frac{E_v + U_i}{E_v}} \, . \tag{12b}$$

To obtain the angle β, under which the electron propagates within the solid, equation 12 can be rearranged to:

$$\beta = \arcsin\left(\sqrt{\frac{E_v}{E_v + U_i}} \sin(\alpha)\right) . \tag{13}$$

Using the trigonometric identity $\cos(\arcsin(x)) = \sqrt{1 - x^2}$ on equation (27b) one can derive an expression for the perpendicular component of the momentum in

the solid.

$$k_{s,\perp} = \sqrt{2(E_v + U_i)}\cos(\beta) \tag{14a}$$

$$= \sqrt{2(E_v + U_i)(1 - \frac{E_v}{E_v + U_i}\sin^2(\alpha))} \tag{14b}$$

$$= \sqrt{2E_v(1 - \sin^2(\alpha)) + 2U_i} \tag{14c}$$

$$= \sqrt{2E_v\cos^2(\alpha) + 2U_i} \ . \tag{14d}$$

As presented in the following sub-chapter, the perpendicular component of the momentum is used to obtain information at which energies constructive interference peaks are to be expected. This can be accomplished by using both the von Laue as well as the Bragg condition.

3.2.1 Laue and Bragg theorem

The formation of constructive interference peaks of electrons in crystalline materials can be understood and described via the von Laue as well as via Bragg condition [40]. In the following section the von Laue condition is derived and subsequently the equivalence between both conditions is proven.

First, it is assumed that an incident wave, more specifically an electron wave, is elastically scattered on point-like scattering centres arranged in a lattice. The scattering centres are the atoms in the crystal lattice and therefore the distance between two points is determined by the lattice vector $\vec{R}$. In figure 11 a scattering event at two points with distance vector $\vec{R}$ is shown. The incident wave has the wave vector $\vec{k} = k\hat{n}$ and the scattered wave $\vec{k}' = k'\hat{n}'$ respectively. This results in the path difference

$$R\cos(\theta) + R\cos(\theta) = \vec{R}\cdot(\hat{n} - \hat{n}') \quad . \tag{15}$$

Constructive interference occurs if and only if the path difference of two waves with identical magnitude of the wave vectors ($k = k'$[3]) is a $2\pi m$ multiple of the wavelength λ with an integer $m \in \mathbb{Z}$. Hence the condition for constructive interference is

$$\vec{R}\cdot(\hat{n} - \hat{n}') = 2\pi m\lambda \ . \tag{16}$$

Substituting $k = \frac{2\pi}{\lambda}$ into equation (16) results in

$$\vec{R}\cdot(\vec{k} - \vec{k}') = 2\pi m \ . \tag{17}$$

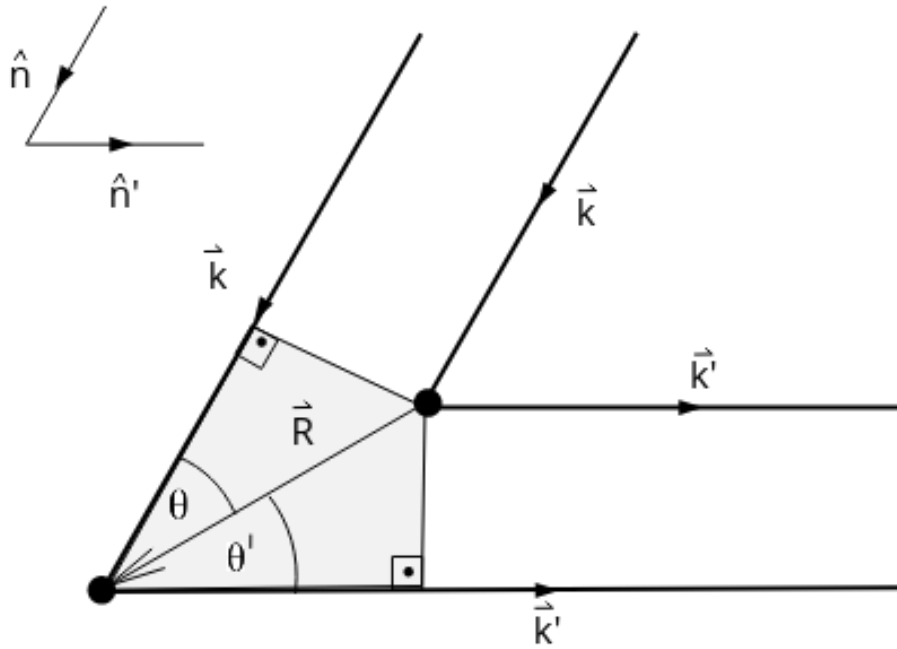
[3]This implies elastic scattering

Figure 11: Schematic illustration of travel length difference of an incoming electron wave. Note: This graph was drawn based on [40]

This equation is equivalent with the notation

$$e^{i(\vec{k'}-\vec{k})\cdot\vec{R}} = 1 \; ,$$ (18)

which corresponds exactly to the definition of the reciprocal lattice vector $\vec{G}$:

$$e^{i\vec{G}\cdot\vec{R}} = 1 \; .$$ (19)

Therefore constructive interference occurs, if the difference of the wave vectors equals a reciprocal lattice vector [40, 41]:

$$\vec{k'} - \vec{k} = \vec{G} \; .$$ (20)

Equation (20) represents the first formulation of the von Laue condition. An equivalent formulation follows by using

$$\vec{k'} = \vec{k} - \vec{G} \; .$$ (21)

With the condition for elastic scattering (i.e. $k = k'$) one obtains by squaring both sides of equation (21):

$$k'^2 = k^2 = k^2 + G^2 - 2\vec{k} \cdot \vec{G} \qquad (22a)$$

$$\vec{k} \cdot \vec{G} = \frac{1}{2}G^2 \qquad (22b)$$

$$\vec{k} \cdot \hat{G} = \frac{1}{2}G. \qquad (22c)$$

The von Laue condition, i.e. the condition for constructive interference, is satisfied if the projection of the wave vector $\vec{k}$ onto the reciprocal lattice vector $\vec{G}$ is exactly half of the magnitude of $\vec{G}$. As mentioned at the beginning, both the
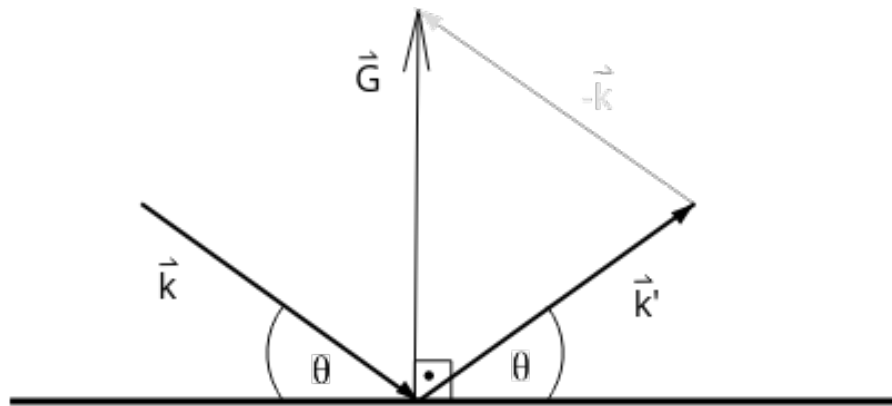

Figure 12: Illustration of Laue condition and that the incoming and outgoing wave vector share the same angle with respect to the normal plane to the reciprocal lattice vector. Note: this graph was drawn based on [40]

von Laue and the Bragg condition are equivalent to each other. The following section is devoted to the proof of this statement.

Suppose, $\vec{k}$ and $\vec{k}'$ fulfill the von Laue condition and elastic scattering shall be assumed ($k = k'$). Figure 12 schematically illustrates an incoming wave, which will be elastically scattered on a normal plane to $\hat{G}$. Due to the elastic scattering assumption, the incoming and the outgoing wave each enclose the same angle θ with respect to the normal plane, leading to an angle $\frac{\pi}{2} - \theta$ between $\vec{k}$ nad $\hat{G}$. The magnitude of a reciprocal lattice vector $|G|$ can also be written as the n-fold multiple of the shortest reciprocal lattice vector $G_0 = n\frac{2\pi}{d}$, where d is the distance between two atomic layers in real space and n is an integer. Using $|\vec{k}| = \frac{2\pi}{\lambda}$ and

$G = n\frac{2\pi}{d}$, Bragg's law can be derived from equation 22c:

$$\vec{k} \cdot \hat{G} = \frac{1}{2}|G| \tag{23a}$$

$$|\vec{k}||\hat{G}|\cos(\frac{\pi}{2} - \theta) = n\frac{2\pi}{d} \tag{23b}$$

$$\frac{\sin(\pi)}{\lambda} = n\frac{2}{d} \tag{23c}$$

$$2d\sin(\theta) = n\lambda \quad , \tag{23d}$$

where λ is the wavelength of the wave.

3.2.2 Determination of the inner potential of HOPG

As aforementioned, the von Laue and Bragg condition are equivalent to each other and determine the circumstances under which a wave constructively interferes with itself. In contrast to light, for electrons the Bragg condition is not sufficient to predict interference phenomena, since Snell's law must be considered as well.

Considering Snell's law for electrons from equation 12, one can obtain the equivalent expression:

$$\frac{\sin(\alpha)}{\sin(\beta)} = \sqrt{\frac{E_v}{E_v + U_i}} \tag{24a}$$

$$\frac{1 - \cos^2(\beta)}{1 - \cos^2(\alpha)} = \frac{E_v}{E_v + U_i} \tag{24b}$$

$$\cos^2(\beta) = 1 - \frac{E_v\cos^2(\alpha) + U_i}{E_v + U_i} \quad . \tag{24c}$$

The wavelength inside the solid is given the de Broglie wave length $\lambda_{dB} = \frac{2\pi}{k_s}$ with $k_s = \sqrt{2(E_v + U_i)}$, as shown figure 10. Substituting λ_{dB} into the Bragg condition from equation 23d and using $\beta = \frac{\pi}{2} - \theta$ yield:

$$2d\cos(\beta) = n\frac{2\pi}{\sqrt{2(E_v + U_i)}} \quad . \tag{25}$$

Finally, combing equation 24 with equation 25 results in an expression, in which only known quantities appear

$$E_v = \frac{1}{\cos^2(\alpha)}\left(n^2\frac{\pi^2}{2d^2} - U_i\right) \quad . \tag{26}$$

24

Therefore it is possible to determine the inner potential experimentally by measuring the Bragg diffraction maxima $E_v(n)$, when the interlayer distance d and the angle of incidence α are known. In this way, we determined recently a value for the inner potential of highly oriented pyrolytic graphite of $U_i = 16.8 \pm 1.6\,eV$[27].

3.3 Inelastic constructive interference
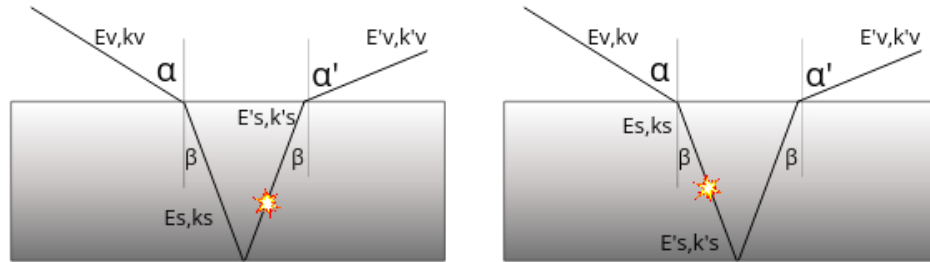
(a) Schematic Trajectory of the D+L model with the incident angle α, the refracted angle β, the energy E and the momentum k , the notation of the subscripts is given in the main text. The inelastic scattering event is represented by an explosion symbol.

(b) Same as in (a), but for the L+D model.

Figure 13

It has been recognised that diffraction phenomena of inelastically scattered electrons are strongly influenced by the diffraction of elastically scattered electrons. By calculating the inelastic cross section for discrete energy losses of $1 < \Delta E < 30$ eV using a quantum field theory model (QFT), in the early 1970's Duke et al. [2–5] showed, that inelastic diffraction gives rise to two solutions for constructive interference. More specifically, if constructive interference occurs for elastically scattered electrons at an energy $E_v(n)$, then for inelastically scattered electrons it occurs at energies $E_v(n)$ as well as $E_v(n)+\Delta E$. Such a relation between the modulation of elastically and inelastically diffracted electrons has been observed experimentally, for instance in 1999 by Ruocco et al. [1]. One of the main goals in this work is to describe inelastic interference phenomena using two semi-classical models in which only the crystal structure and the inner potential of the target is considered.

In a specular reflection geometry, an inelastic event is always linked to an elastic collision, mostly independent on the type or the magnitude of energy loss[1, 42, 43]. This results in two possible channels: elastic before inelastic (Diffraction +

Loss) and inelastic before elastic (Loss+Diffraction), as shown in figure 13. In both models, the electron beam with energy E_v hits the surface at the angle α with respect to the surface normal. The beam is deflected by the inner potential and continues to propagate at the angle β in the solid (see chapter 3.2). Now, the electron can scatter inelastically either before or after the elastic diffraction on the lattice. Each path gives rise to two different outcomes, as described in the following sections.

3.3.1 Diffraction before loss (D+L)

In this section, the case is studied where the incoming is first scattered elastically and subsequently inelastically. This is shown in figure 13a. An electron beam (black trajectory) with energy E_v and momentum $\vec{k_v}$ hits the surface of the target at angle α. The beam is deflected by the inner potential U_i and continues to propagate inside the solid with:

$$E_s = E_v + U_i \tag{27a}$$

$$\vec{k_s} = \begin{pmatrix} k_{s,\parallel} \\ k_{s,\perp} \end{pmatrix} = |\vec{k_s}| \begin{pmatrix} \sin(\beta) \\ \cos(\beta) \end{pmatrix} \tag{27b}$$

$$|\vec{k_s}| = \sqrt{2E_s} \ . \tag{27c}$$

Hence, the same kinematic conditions apply for purely elastically scattered electrons and for electrons in the D+L model. Therefore, such electrons, diffraction maxima occur at the energies $E_v(n)$ predicted in equation 26 for purely elastically scattered electrons.

After the elastic diffraction, the electron collides inelastically with a solid-state electron. In such a process, both energy and momentum conservation must be taken into account. From energy and momentum conservation follows:

$$E_s' = E_s - \Delta E \tag{28a}$$

$$|k_s'| = \sqrt{2(E_s - \Delta E)} \tag{28b}$$

$$\vec{k'}_s = \vec{k}_s - \Delta\vec{K} \quad , \tag{28c}$$

where ΔE is the energy- and $\Delta\vec{K}$ is the momentum-transfer from the primary electron to a solid state electron and the primed symbols correspond to the quantities of the primary electron after the collision. However, without more precise knowledge about collision partner, a unique determination of $\Delta\vec{K}$ is impossible. In the literature, it is often assumed that the direction of the primary

electron is maintained during this process and thus the momentum transfer only occurs in the forward direction [1–3, 43, 44]. This assumption results in the momentum after the inelastic collision:

$$\beta' = \beta \tag{29a}$$

$$k'_{s,\perp} = k'_s \cos(\beta) \tag{29b}$$

$$k'_{s,\parallel} = k'_s \sin(\beta) \quad . \tag{29c}$$

Since the magnitude of the momentum has changed, the exit angle α' differs from the incidence angle α. Snell's law for the exit angle is given by

$$\frac{\sin(\alpha')}{\sin(\beta)} = \frac{k'_s}{k'_v} \tag{30}$$

where k'_s and k'_v are the momenta in the solid and in vacuum. By combining equation (12) with equation (30), one obtains:

$$\sin(\alpha') = \sin(\alpha)\sqrt{\frac{(E_v + U_i)(E_v - \Delta E)}{E_v(E_v + U_i - \Delta E)}} \tag{31}$$

It follows that the inelastic channel interferes constructively at the same energy as purely elastically scattered electrons but leaves the solid at a different angle. The limiting case for $\Delta E \to 0$ results in $\alpha' = \alpha$, which is consistent with the purely elastically scattered electrons.

3.3.2 Loss before Diffraction (L+D)

In the loss before diffraction (L+D) model (see figure 13b), the electron suffers the energy loss ΔE before it scatters elastically on the lattice. As in the previous model, it shall be assumed, that the momentum transfer $\Delta \vec{K}$ only occurs in the forward direction, so that the main kinematic properties after the event are given by:

$$E'_s = E_s - \Delta E \tag{32a}$$

$$|k'_s| = \sqrt{2(E_s - \Delta E)} \tag{32b}$$

$$k'_{s,\perp} = |k'_s| \cos(\beta) \tag{32c}$$

$$k'_{s,\parallel} = |k'_s| \sin(\beta) \quad . \tag{32d}$$

Consequentially, the kinematical circumstances under which elastic diffraction occurs at the lattice are no longer identical with those for purely elastically diffracted electrons. Thus, for the L+D model, the von Laue condition must be adapted to the new momentum. For this purpose, recall the von Laue condition from equation 22c:

$$\vec{k} \cdot \hat{G} = \frac{1}{2} G \tag{33}$$

with $\hat{G}$ pointing perpendicular to the surface and $G = n\frac{2\pi}{d}$. The left-hand side of this equation just gives the perpendicular component of the momentum, as the dot-product is the projection of the momentum onto the reciprocal lattice vector, which is perpendicular to the surface. Therefore, by substituting the left-hand with $k'_{s,\perp}$ one obtains:

$$k'_{s,\perp} = \frac{n\pi}{d} \tag{34a}$$

$$\sqrt{2(E_v + U_i - \Delta E)} \cos(\beta) = \frac{n\pi}{d} . \tag{34b}$$

One can substitute $\cos(\beta) = \sqrt{1 - \frac{E_v}{E_v + U_i} \sin^2(\alpha)}$ (see equation (13)), resulting in:

$$\sqrt{2(E_v + U_i - \Delta E)}\sqrt{1 - \frac{E_v}{E_v + U_i} \sin^2(\alpha)} = \frac{n\pi}{d} . \tag{35}$$

Squaring both sides yields:

$$E_v \cos^2(\alpha) + U_i - \Delta E + \Delta E \frac{E_v}{E_v + U_i} \sin^2(\alpha) = \frac{n\pi}{2d} . \tag{36}$$

Arranging terms in order of the power of E_v gives:

$$E_v^2 \cos^2(\alpha) + E_v(U_i \cos^2(\alpha) + U_i - \Delta E \cos^2(\alpha) - \frac{n^2\pi^2}{2d^2}) + (U_i^2 - \Delta E U_i - \frac{n^2\pi^2}{2d^2} U_i) = 0 . \tag{37}$$

The two solutions for E_v read:

$$E_{v,1,2} = \frac{-\cos^2(\alpha)(U_i - \Delta E) - (U_i - \frac{n^2\pi^2}{2d^2}) \pm \Delta}{2\cos^2(\alpha)} , \tag{38}$$

where
$$\Delta = \sqrt{[\cos^2(\alpha)(U_i - \Delta E)]^2 + (U_i - \frac{n^2\pi^2}{2d^2})^2 + 2\cos^2(\alpha)[\Delta E(U_i + \frac{n^2\pi^2}{2d^2}) - U_i(U_i - \frac{n^2\pi^2}{2d^2})]}.$$
This equation gives two possible solutions for which the von Laue condition is fulfilled. To verify which of the two branches corresponds to the physically

correct solution, the limiting case for $\Delta E \to 0$ was calculated:

$$\lim_{\Delta E \to 0} E_{v,1,2} = \frac{-\cos^2(\alpha)U_i - (U_i - \frac{n^2\pi^2}{2d^2}) \pm \Delta}{2\cos^2(\alpha))} \tag{39a}$$

$$\lim_{\Delta E \to 0} E_{v,1,2} = \frac{-\cos^2(\alpha)U_i - (U_i - \frac{n^2\pi^2}{2d^2}) \pm [\cos^2(\alpha) - (U_i - \frac{n^2\pi^2}{2d^2})]}{2\cos^2(\alpha))} \tag{39b}$$

$$\lim_{\Delta E \to 0} E_{v,1,2} = \begin{cases} \frac{1}{\cos(\alpha)}(\frac{n^2\pi^2}{2d^2} - U_i) & \text{for the positive branch} \\ -U_i & \text{for the negative branch} \end{cases} \tag{39c}$$

It follows that in the limiting case for low energy losses, the positive branch yields the identical solution as for purely elastically scattered electrons and will therefore be used to determine the energies for constructive interference in the L+D model.

With given experimental parameters (U_i, α and $A = \frac{n^2\pi^2}{2d^2}$) one can now calculate the energies at which one would expect constructive interference phenomena in the L+D channel using:

$$E_{LD} = \frac{-\cos^2(\alpha)(U_i - \Delta E) - (U_i - \frac{n^2\pi^2}{2d^2}) + \Delta}{2\cos^2(\alpha)} \quad . \tag{40}$$

From equation (40) follows no obvious or trivial connection between the von Laue condition and the energy loss. However, one can rearrange terms in equation (36) to obtain

$$\sqrt{2(E_v + U_i - \Delta E)}\cos(\beta) = \frac{n\pi}{d} \tag{41a}$$

$$E_{LD} = \frac{1}{\cos^2(\alpha)}\left(\frac{n^2\pi^2}{2d^2} - U_i + \Delta E \frac{\cos^2(\beta)}{\cos^2(\alpha)}\right) \quad . \tag{41b}$$

From this representation it follows immediately that in the L+D channel there is an energy shift ΔE_{Pos} of the Bragg peaks. Since $\beta < \alpha \,\forall \alpha \in]0, \frac{\pi}{2}[$ it follows strictly that the energy shift is towards higher energies and further, since

$$\frac{\cos^2(\beta)}{\cos^2(\alpha)} = \frac{1 - \frac{E_v}{E_v + U_i}\sin^2(\alpha)}{1 - \sin^2(\alpha)} > 1 \quad , \tag{42}$$

the shift is greater than the energy loss ΔE.

For the L+D model the kinematics for leaving the solid on the solid-vacuum interface are identical compared to the D+L model. There, the exit angle α',

under which the electron leaves the target, is given by equation 31. In strong contrast to the D+L mode, where the diffraction maxima $E_v(n)$ are identical to pure elastic scattering, the predicted energies in the L+D model are shifted to higher energies. The energy shift $E_{shift} = \Delta E \frac{\cos^2(\beta)}{\cos^2(\alpha)}$ is a function of the incident energy E_v, as plotted in figure 14 for $U_i = 16eV$ and $\alpha = 30, 60$. As this graph shows, the L+D model predicts for high energies (> few 100eV): $E_{shift} \rightarrow \Delta E$. This is in good agreement with experimental and theoretical observations and studies [1–3, 42, 43]. At lower energies, a strong deviation from the expected shift is predicted, since the L+D model predicts that the shift of the diffraction maxima is significantly larger than the energy loss. However, the modulation of the elastically and inelastically scattered electrons in this energy range is not determined by Bragg diffraction, but by other effects, such as the band structure of the target. It is nevertheless remarkable that with such a simple model, the same result (for E_v > few 100eV) can be obtained as with complex quantum field theory (QFT) calculations [2–5].

In summary, the models presented above both describe the case where an
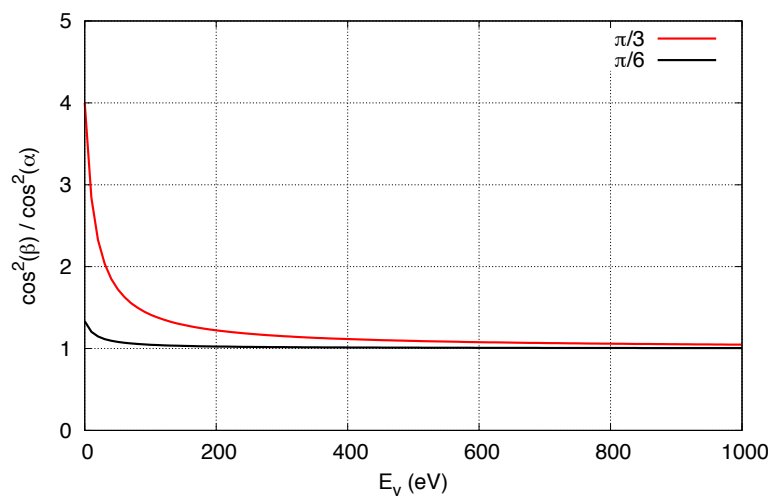
Figure 14: Factor $\frac{\cos^2(\beta)}{\cos^2(\alpha)}$ as a function of the incident energy E_v, using equation 42 with $U_i = 16eV$, $\alpha = 30°$(black) and $\alpha = 60°$(red).

electron is elastically diffracted at the lattice, but loses energy in the solid in a single inelastic scattering event. It was shown that it is decisive whether the electron loses energy before or after the elastic diffraction. This leads to the fact that for every purely elastic diffraction maximum, two diffraction maxima arise in the inelastic channels. Since there are no constraints that one of the two is

favoured, it is assumed that both cases occur with similar intensity. This can be experimentally verified by measuring the IV curves at certain energy losses. It is to be expected that the diffraction maxima that are in the $\Delta E = 0 eV$ curve separate into two twin peaks that are approximately $\Delta E \frac{\cos^2(\beta)}{\cos^2(\alpha)}$ apart.

4 Methods

4.1 Schematics

4.1.1 Overview

The main data sets in this work concern double differential IVLEED spectra of HOPG. These data were acquired on a secondary electron-electron energy loss coincidence spectroscopy (SE2ELCS) spectrometer at Technische Universität Wien, located in Vienna.

With this apparatus, it is possible to measure full energy spectra in reflection geometries. In order to accomplish this, a target is irradiated with a beam of electrons and the backscattered primary- and emitted secondary electrons are detected. Thereby, the energy of the electrons is measured and recorded via a digital setup. The energy of the electrons is determined in two different ways, firstly, with a time-of-flight (TOF) analyser and secondly with a hemispherical mirror analyser (HMA). This gives rise to spectra similar to that of reflected electron energy loss spectroscopy (REELS) spectra. Such measurements can be used to determine how the target responds to electron bombardment and thus infer the electronic properties of the sample.

The core components of the SE2ELCS include the vacuum system, the electron gun, the detectors and the electronics for digital data acquisition. In order to perform such electron scattering experiments, one must first study the composition of this spectrometer and characterise the working principles and limits for each component. Thus, in the following section, each component will be presented and discussed briefly. A more detailed overview of this specific spectrometer is given by Vytautas Astašauskas in [39].

4.1.2 Vacuum system

Experiments with electron beams require a high vacuum because the inelastic mean free path (IMFP) is strongly correlated with the quality of the vacuum. The IMFP can vary from a few microns at ambient pressure to a few meters in ultra
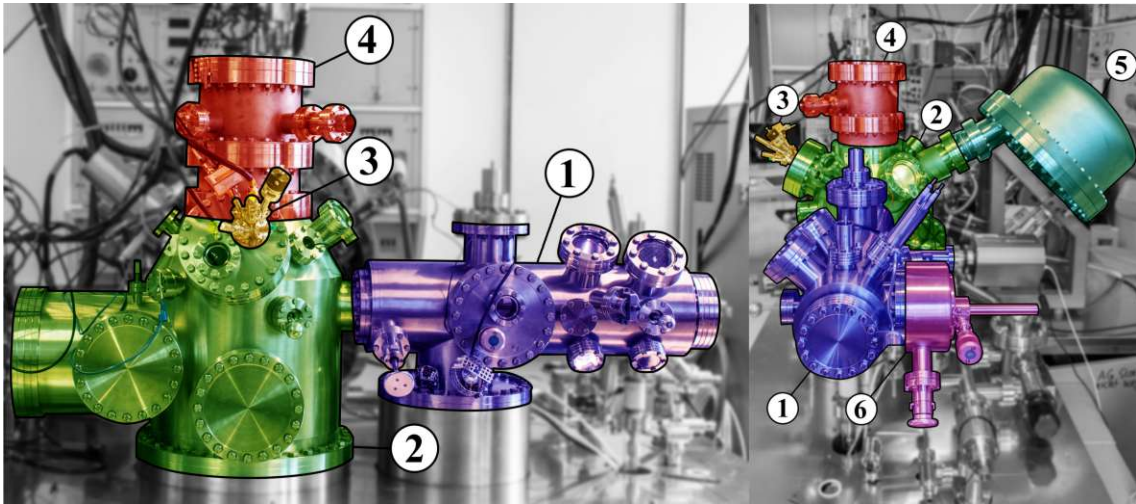
Figure 15: Front (left) and side (right) view of the SE2ELCS spectrometer at TU Wien. (1,purple) Preparation chamber; (2,green) analyser chamber; (3,yellow) electron source; (4,red) TOF drift tube; (5,cyan) HMA; (6,magenta) loadlock [39].
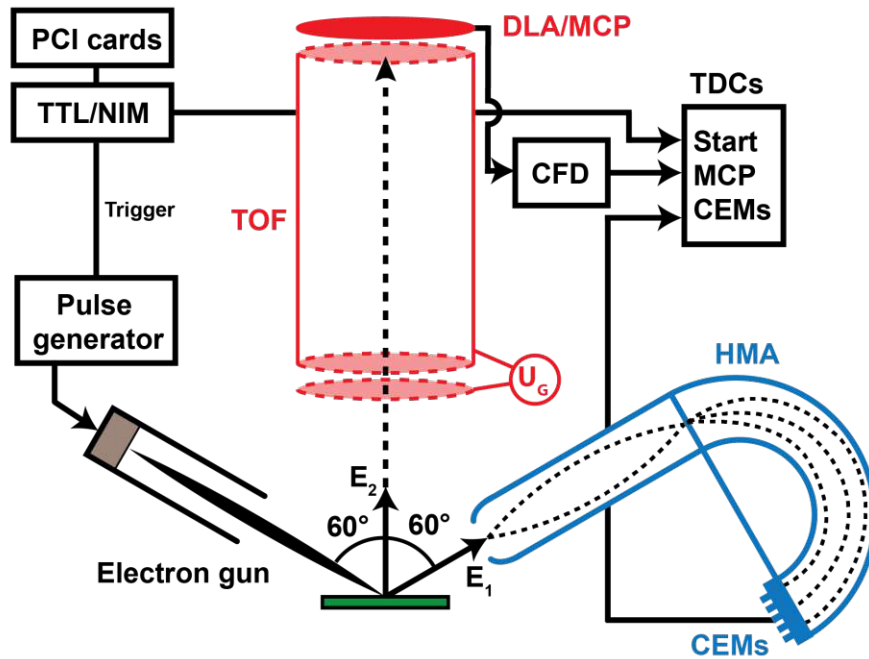

Figure 16: Schematic overview of the experimental set-up in the plane of the beam trajectory. The electron gun, the TOF and the HMA are in the same plane [39].

high vacuum (UHV) environments. Furthermore, residual gas atoms will diffuse through the surface of a solid and will deposit over time in the outermost layers of the specimen. Electrons with energies below 1keV only have a penetration depth of a few atomic layers, therefore, depositions can have a significant influence on the experimental results. Two procedures to improve the surface quality of the sample can be conducted: firstly, reducing the residual gas pressure in the vacuum chamber lowers the rate of deposition in solids and secondly, in-situ sample preparation (e.g. annealing at high temperatures or sputtering with Argon) ensures a clean and pure surface. The required pressure in the vacuum chamber is determined in such a way, that the IMFP of the electrons exceed the working distances in the experiment and that the rate of deposition is sufficiently low that the surface remains pure during the measurements. For the measurements performed in this work, a residual gas pressure of $2 \cdot 10^{-10}$mbar satisfied both objectives.

Photographs of the SE2ELCS are shown in figure 15. It consists of three sealable vacuum chambers: a lock load (6), a preparation chamber (1) and an analyser chamber (2). The load lock is used for introducing new samples into the spectrometer and can be vented down to 10^{-8}mbar. As soon as the pressure is sufficiently reduced, the sample will be transferred from the load lock into the preparation chamber. The sample is mounted on a rail-guided sample holder using wobble sticks. This chamber contains several vacuum pumps, an argon sputtering gun and a quadrupole mass spectrometer. The preparation chamber allows sample preparation through sputtering without secondary particles entering the chamber with the measuring instruments. Furthermore, the mass spectrometer can be used to inspect the vacuum system for leaks by externally spraying the chamber with helium ^4He. Because of the high diffusivity and the low natural concentration of helium, this gas easily penetrates the vacuum chambers through leaks. In case of a leak, a significantly increased ^4He concentration would be measured in the mass spectrometer. An ionic pump vents the preparation chamber down to the 10^{-10}mbar range. Once the pressure in the preparation chamber is low enough, the sample is allowed to be transferred to the analyser chamber. The analyser chamber is separated from the preparation chamber to avoid contaminants from traces of atmospheric water. This chamber contains several vacuum pumps, a thermionic electron source (e-gun), a time of flight (TOF) analyser, a hemispherical mirror analyser (HMA), an x-ray source, a sample stage and an additional argon sputtering gun. The sample stage can be manually moved, tilted and rotated to optimise the sample's position. The e-gun, the TOF and the HMA are in the same plane, as

shown in figure 16, allowing measurements in specular reflection geometries. Specular reflection geometries for the HMA can be achieved using an untilted, flat sample and for the TOF analyser by tilting the surface by 30° towards the electron source, as shown in figures 17. A more extensive and elaborate discussion of the vacuum system was conducted by Vytautas Astašauskas in [39]. The experiments in this work were conducted at a base pressure of $2 \cdot 10^{-10}$ mbar.
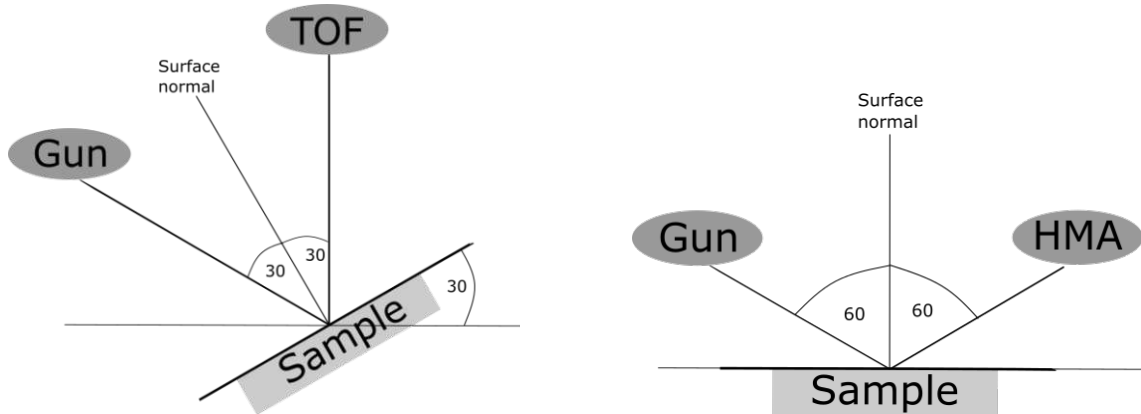
(a) Experimental set-up for a specular reflection geometry measurement with TOF. The sample is tilted by 30° torwards the electron source, so that the e-gun and the TOF drift tube are located at 30° with respect to the surface normal.

(b) Experimental set-up for a specular reflection geometry measurement with HMA. The e-gun and the HMA are both located at 60° with respect to the surface normal.

Figure 17: Specular reflection geometries for HMA and TOF experiments.

The pressure was measured with a hot filament ionisation gauge (HFIG). Since HFIG produce a significant number of stray electrons, the pressure was not monitored during ongoing experiments. This would not only negatively impact the experimental results, but moreover could inflict fatal and irreversible damage on the electron detectors, as their lifespan is characterised by total electron counts. The base pressure during an experiment with a duration of 1 month has risen only by $3 \cdot 10^{-10}$ mbar, indicating a high-quality vacuum system.

4.1.3 Electron source

The first step in specifying an electron spectrometer is to characterise the electron source. The SE2ELCS spectrometer uses a thermionic Kimbal Physics ELG-2 electron source (e-gun). The most important specifications are given in Table 1. In electron scattering experiments, the quality of the electron source contributes substantially to the experimental results, as inconsistencies in energy or intensity will have a direct impact on the acquired spectra. The employed e-gun is well suited for the experiments conducted in this work, since it provides an

Beam energy	1eV to 2keV
Energy spread	0.5eV
Beam current	1nA to 10μm
Energy stability	±0.01%
Beam stability	±0.1% per hour (with emission current control)
Pulse capability	Min. Pulse width 20ns
Spot size	0.5 mm to 5 mm (@2cm working distance)

Table 1: Overview of the most important specifications of the electron source [45].

electron beam with minimal energy and intensity fluctuations. A comprehensive overview of all specifications of the electron gun is given in the e-gun manual in [45]. The block diagram of the electron source is presented in figure 18. The
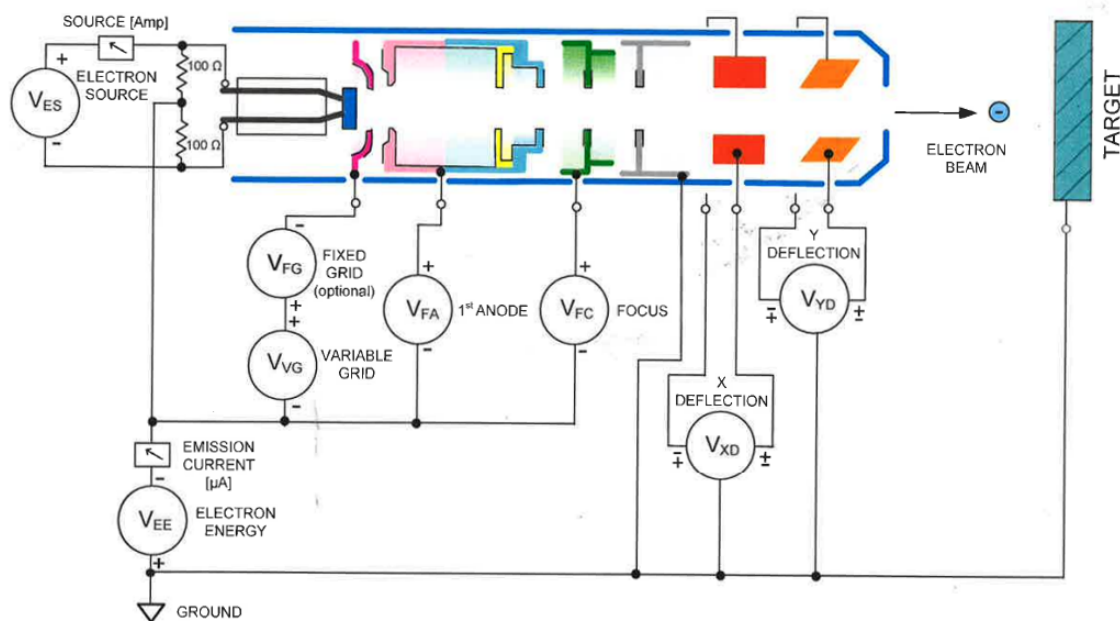

Figure 18: Block diagram of the electron gun [45].

electron beam is created and controlled in a five-step process, as followed:

- The electrons are generated by a thermionic cathode, consisting of a tantalum disk. The disk is heated by a tungsten hairpin filament to the emission temperature $T_{emission}$ = 2200K.

- The number of electrons being emitted by the cathode is controlled by a Wehnelt cylinder. Applying a negative voltage U_{Grid} to the cylinder results in the suppression of the electron emission. If the applied voltage is high enough, the electron emission is completely suppressed and the intensity of the electron beam diminishes to negligible levels. Hence, by supplying a

35

negative square wave signal to the cylinder, one can produce a time-pulsed beam, which is mandatory for time-of-flight measurements.

- The positively charged first anode extracts the electrons out of the Wehnelt cylinder and controls the intensity of the beam with the voltage V_{FA}.

- The focus unit acts as an electron lens and focuses the beam onto the surface of the target and, hence, determines the spot size and diameter of the beam. A typical spot size of 1-2mm was used during the conducted experiments.

- Lastly, the beam can be deflected in x and y direction by an electrostatic Field between two pairs of parallel metal plates.

The beam energy is determined by the potential difference between the sample and the cathode. Section 4.2 covers the energy scale of reference in detail.

Note that during the measurement procedure, it was observed that the energy of the elastic peak depends on the grid voltage. An investigation on this behaviour yielded a linear dependency of the elastic peak energy and the grid voltage, as shown in figure 19. However, no explanation for this phenomenon could be found, but this energy shift was considered in the scaling of the experimental data.
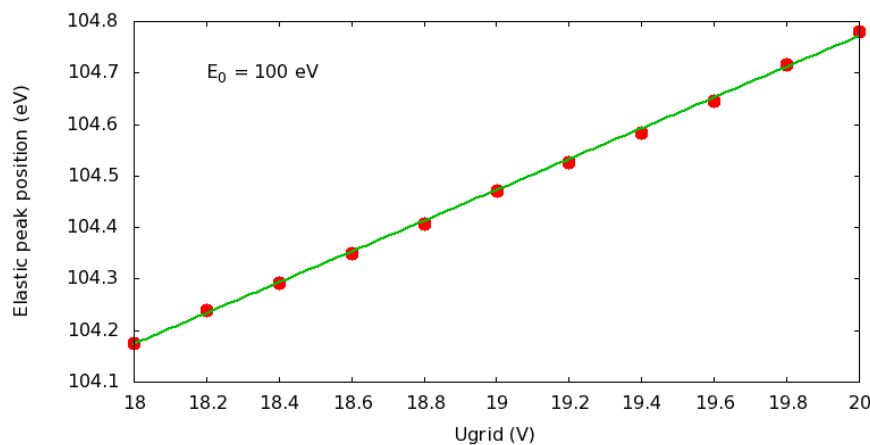

Figure 19: Demonstration of the grid Voltage dependence of the landing energy on the grid voltage. The red points represent the energy of the elastic peak measured at an acceleration voltage of $100V$. Note: the y-scale is given with respect to the Fermi-level. It is clearly observable that the landing energy increases linearly with the grid voltage. Originally published in [39].

4.1.4 Analysers

Time-of-Flight Analyser

The first discussed analyser is a time of flight (TOF) analyser.

TOF mechanical set up

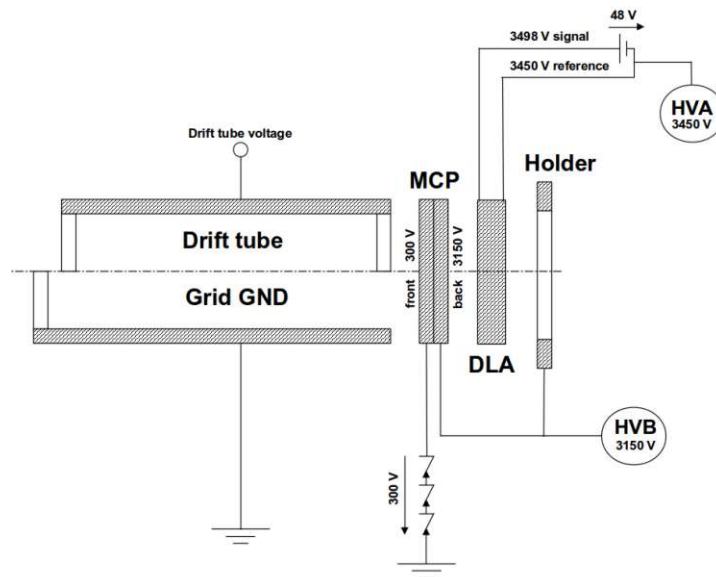The analyser consists of a field free drift tube, placed above the sample. On

Figure 20: Mechanical structure of the TOF: consisting of a drifttube, followed by the MCP and the DLA. Originally published in [39].

top of the drift tube, three Multi Channel Plates (MCP) are mounted. An MCP can be seen as an array of electron multipliers to increasing the signal strength. Once an electron hits the surface of the MCP, multiple electrons will be emitted, which in turn can emit several electrons and thus trigger a chain reaction. Thus, a cloud of electrons reaches the Delay Line Anode (DLA). The DLA is placed on top of the MCP. It consists of three stacked coiled wire-pairs and therefore can locate where and when the electron hits the DLA. This enables one to measure the exact position of the incoming electrons. The flight times are determined by measuring the time difference between the emission of a short electron pulse and the time until the electron cloud hits the DLA. The starting time is therefore well determined by the pulsed electron beam of the electron gun. After taking into account the runtimes of the evaluation electronics, the actual flight time of the electron can be calculated.

General consideration of TOF analysers

A TOF analyser measures the time it takes for an electron to travel from its

37

emission to the detector. The time measurement starts with the emission of a short electron pulse from the electron source and ends for the respective electrons with the detection at the delay line anode (DLA). The signal at the DLA is recorded in equidistant time intervals. Depending on the energy of the electrons, they will be detected in different time-bins, resulting in a time of flight spectrum. For non-relativistic particles with mass m and energy E the time of flight t can be estimated with:

$$E = \frac{mv^2}{2} = \frac{ms^2}{t^2} \tag{43a}$$

$$t = \sqrt{\frac{ms^2}{E}} \, , \tag{43b}$$

with the traveled distance s. This equation gives a qualitative description of the fact that the relationship between energy and time of flight is non-linear, however gives a good estimate for the conversion of the two quantities. Note, that the time of flight diverges for electrons with a kinetic energy of 0eV. Accurate and realistic conversion from time of flight to energy is analytically difficult because the trajectory of the electrons is not known due to the present electric and magnetic fields inside the vacuum chamber. However, one can perform electron trajectory simulations to obtain a suitable conversion of TOF to energy for a specific geometry. The results of such simulations are saved in look-up tables (LUT). It is important to add, that due to the non-linear relation of energy and time of flight, the resolution of the TOF depends on the energy of the electrons. The TOF analyser is best suited for low energy electrons, since the time-bins in the spectrum are constant and the energy resolution dE diminishes for higher energy:

$$dt = \frac{\partial}{\partial E} \sqrt{\frac{ms^2}{E}} dE \quad . \tag{44}$$

Hemispherical mirror analyser

The second analyser is a hemispherical mirror analyser (HMA), which uses 5 channeltron electron mutliplyers (CEM) as detectors, as shown in figure 16. The channeltrons are spaced in equidistant positions on the end of the HMA. The HMA consists of two parallel hemispherical metal shells and to each a high voltage potential can be applied. Consequentially, incoming electrons travel on Kepler trajectories, where the eccentricity depends on the kinetic energy of the electrons. The HMA can perform in two different modes: constant analyser energy (CAE) and constant retard ratio (CRR). In the CAE mode, the incoming electrons will be accelerated or decelerated by a retard voltage to a characteristic

CH1	E_{pass}-5%
CH2	E_{pass}-2.5%
CH3	E_{pass}
CH4	E_{pass}+2.5%
CH5	E_{pass}+5%

Table 2: Overview of the HMA energy resolution in CAE mode. Note that the energy resolution is independent from the electron energy.

pass energy E_{pass}. Consequently, electrons which reach the end of the HMA have a constant energy. Electrons with the pass energy will be detected in the centre channeltron. Electrons with slightly higher or lower energy will be detected as given in Table 2. By sweeping the retard voltage, one can acquire full energy range REELS spectra with constant energy resolution. This is a key advantage of the HMA over the TOF, as the resolution of the TOF diminishes with increasing energies. In CRR mode, the ratio between the retard voltage and the pass energy is kept constant. However, the experiments in this work were exclusively operated in the CAE mode using, as the CRR mode is only used in Auger electron spectroscopy (AES)[39].

Comparison of TOF and HMA spectra

Figure 21 shows a comparison of typical energy spectra of the two analysers at a primary energy of 99eV. One can clearly see that the resolution of in the TOF energy spectrum (blue) diminishes at higher energies, resulting in the broadening of the elastic peak. However, the strength of the TOF analyser is its high resolution in the low energy part of the spectrum ($E < 50eV$). In contrast, the HMA offers consistently good energy resolution over the entire energy range. In the discrete energy loss region, the plasmonic structure can be observed. Fig 17b presents the experimental set-up for a measurement in specular angle. The electron beam hits the surface of the solid at a polar angle of 60°.

4.1.5 Sample

The experiments in this work were conducted on highly oriented pyrolytic graphite (HOPG). HOPG is a synthetic, layered poly crystalline form of graphite. Regular graphite, and especially natural graphite, only has a short term order, but not a long term order, because water inclusions and other impurities lead to shifts, rotations and bending of the crystal lattice. HOPG is a highly pure and highly ordered variant of graphite that does not occur naturally in this form. It is produced at around 3000°C and under high pressure, whereby the number of defects is significantly reduced. The grains of HOPG are about 10μm in size [46]
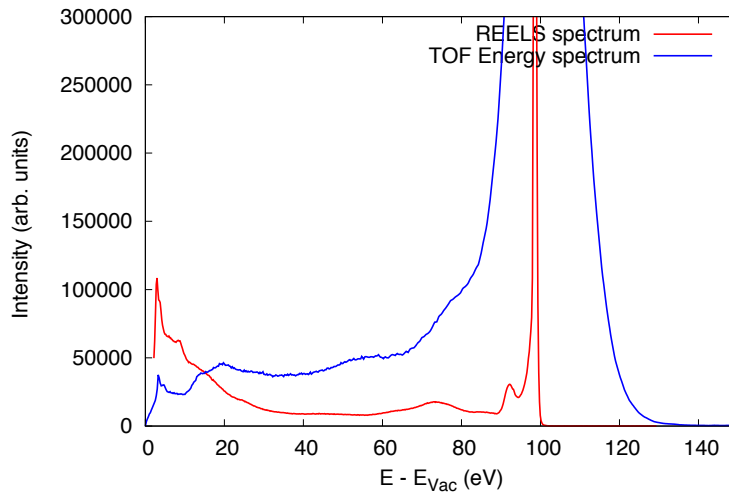
Figure 21: Comparison of a converted TOF energy spectrum and a HMA reflected electron energy loss (REEL) spectrum of HOPG with $E_{Land} = 99eV$. Note that the angle of incidence is not equal for both spectra (HMA: $\alpha = 60$; TOF: $\alpha = 30$ and thus a direct comparison can be misleading. However, the different characteristics strength of each analyser is still emphasised.

and are arranged arbitrarily in the lateral plane, but have a high degree of order along the c-axis. The mosaic spread in the c-axis of the HOPG sample used in this work is specified as 0.8 ± 0.2(ZYB quality). Owing to its high degree of order, HOPG is used as a magnification calibration substrate for scanning tunneling microscopes (STM) or as a monochromator for neutron and X-ray beams. In this work, HOPG is investigated for its electronic properties by means of inelastic very low energy electron diffraction (IVLEED).

The crystalline structure of HOPG is presented in figure 22a. The crystal consists of A,B carbon atoms arranged in hexagons in the x-y plane, forming the typical carbon honeycomb structure. In the c-axis, the planes are arranged in such a way that the B' of the upper layer is centred over the hexagon of the lower layer.

The carbon atoms in the lattice form three hybridised sp^2 orbitals [39]. Two of those orbitals, namely p_x and p_y, form dp^2 hybrid orbitals with the neighbouring atoms in the x-y plane in the characteristic 120° honeycomb structure . The third p_z orbital is perpendicular to the sp^2 hybrid states and forms weak π bonds with atoms of the next layers[39, 47]. This weak bond gives rise to weak Van der Waals (VdW) forces between the layers. Since even slight mechanical forces can cause the VdW bonds to break, graphite is used, for instance, in pencils. In addition,

this results in a unique form of sample preparation, namely the "Scotch-tape-method", wherein the sample can be exfoliated using adhesive tape; revealing an atomically flat and pure surface.

The bombardment of HOPG with electrons gives rise to oscillations in the charge density. Electrons in π orbitals prefer to oscillate between the layers, creating the π-plasmon. In contrast, electrons in the hybrid sp^2 orbitals prefer to oscillate in-plane, resulting in the $\pi + \sigma$-plasmon.
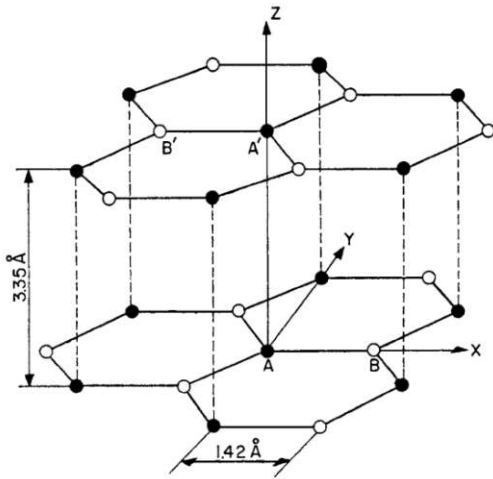
Crystalline structure of Graphite

The unit cell of the 3-dimensional crystal structure is presented in figure 22a. Graphite consists of many graphene layers stacked on top of each other in an ABAB sequence. These layers are bound to each other by weak Van der Waals bonds. Graphene is a flat 2D material, which is characterised by its typical honeycomb structure. The carbon atoms are arranged in two hexagonal sub lattices A and B, which are displaced with respect to each other. In the 3D graphite crystal, the graphene layers are not stacked directly on top of each other, but form a hexagonal symmetry in the space group P64/mmc(#194)[48]. The primitive lattice vectors in this space group are defined as follows:

$$\vec{a_1} = \frac{a}{2}\begin{pmatrix} 1 \\ -\sqrt{3} \\ 0 \end{pmatrix}, \quad \vec{a_2} = \frac{a}{2}\begin{pmatrix} 1 \\ \sqrt{3} \\ 0 \end{pmatrix}, \quad \vec{a_3} = c\begin{pmatrix} 0 \\ 0 \\ 1 \end{pmatrix}. \tag{45}$$

The magnitudes of these vectors are given by the lattice constants $a = 2.46\mathring{A}$ and $c = 6.71\mathring{A}$ [49, 50]. Note that the unit cell ranges over two graphene layers in c-axis and thus the interlayer spacing d is only half the value of c. The Volume of the unit cell is given by the scalar triple product:

$$V_e = \vec{a_1} \cdot (\vec{a_2} \times \vec{a_3}) = \frac{a^2 c \sqrt{3}}{2}. \tag{46}$$

In addition to the lattice, a corresponding base is required for the complete characterisation of a crystal. The base specifies how the A and B atoms are connected to each other in a unit cell. Figure 22a shows that there are four different atoms (A,A',B,B') per unit cell, where A,B and A',B' are on the same

(a) Idealised 3D crystal structure of graphite. Solid circles indicate atoms in the hexagonal sub lattice A and hollow circles the sub lattice B respectively. Primed letters indicate the atoms in the top layer. [49]
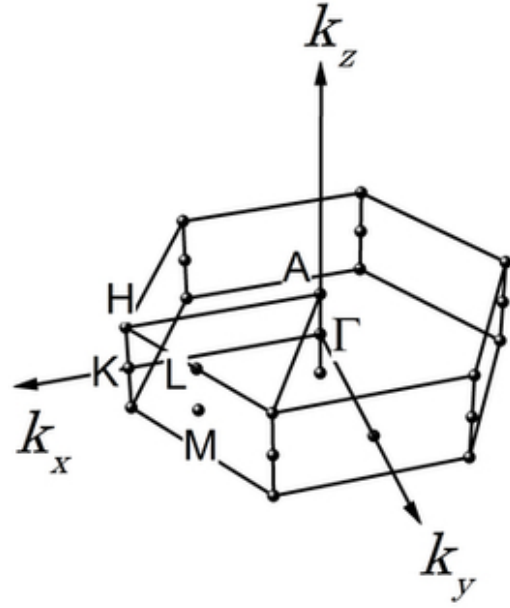
(b) Illustration of the 3D Brilliouin zone of Graphite with the main crystallographic directions [49]

Figure 22

plane. The position of the atoms is given by the following coordinates:

$$\vec{\rho_A} = (0,0,0), \quad \vec{\rho_B} = \frac{a}{2}(\frac{1}{\sqrt{3}}, 1, 0), \quad \vec{\rho_{A'}} = (0, 0, \frac{c}{2}), \quad \vec{\rho_{B'}} = (-\frac{a}{2\sqrt{3}}, -\frac{a}{2}, \frac{c}{2}) \quad (47)$$

The reciprocal space is spanned by the reciprocal lattice vectors $\vec{b_i}$ which are defined as follows:

$$\vec{b_1} = \frac{2\pi}{V_e}(\vec{a_2} \times \vec{a_3}) = \frac{2\pi}{a\sqrt{3}} \begin{pmatrix} \frac{1}{\sqrt{3}} \\ -1 \\ 0 \end{pmatrix} \quad (48a)$$

$$\vec{b_2} = \frac{2\pi}{V_e}(\vec{a_3} \times \vec{a_1}) = \frac{2\pi}{a\sqrt{3}} \begin{pmatrix} \frac{1}{\sqrt{3}} \\ 1 \\ 0 \end{pmatrix} \quad (48b)$$

$$\vec{b_3} = \frac{2\pi}{V_e}(\vec{a_1} \times \vec{a_2}) = \frac{2\pi}{c} \begin{pmatrix} 0 \\ 0 \\ 1 \end{pmatrix}. \quad (48c)$$

The first Brillouin zone (BZ) is defined as the primitive Wigner-Seitz cell in the reciprocal lattice and is plotted for graphite in figure 22b. The coordinates of the main crystallographic symmetry points are given in table 3, where $\vec{k} = u\vec{b_1} + v\vec{b_2} +$

$w\vec{b}_3$.

Symmetry points (u,v,w)	[kx,ky,kz]	Point group
Γ: (0,0,0)	[0,0,0]	6/mmm
A: (0,0,1/2)	[0,0,π/c]	6/mmm
K: (2/3,1/3,0)	[4π/3a,0,0]	62m
H: (2/3,1/3,1/2)	[4π/3a,0,π/c]	62m
M: (1/2,0,0)	[π/a,-π/$\sqrt{3}$a,0]	mmm
L: (1/2,0,1/2)	[π/a,-π/$\sqrt{3}$a,π/c]	mmm

Table 3: Overview of the main crystallographic symmetry points. The point groups are given in the Hermann–Mauguin notation.[51]

4.1.6 Sample preparation

A clean and planar surface is of utmost importance, especially at investigations concerning the surface barrier. Even the smallest deposition of contamination is able to change the outcome by a significant amount. Hence, a careful sample preparation is the key to success.

The specimen is placed on a heatable copper sample holder and is fixed by a

(a) Sample holder used for HMA measurements with incident angle of $\alpha = 60°$. Originally published in [39]

(b) Slanted sample holder used for TOF measurements in specular reflection with incidence angle $\alpha = 30°$. Originally published in [39]
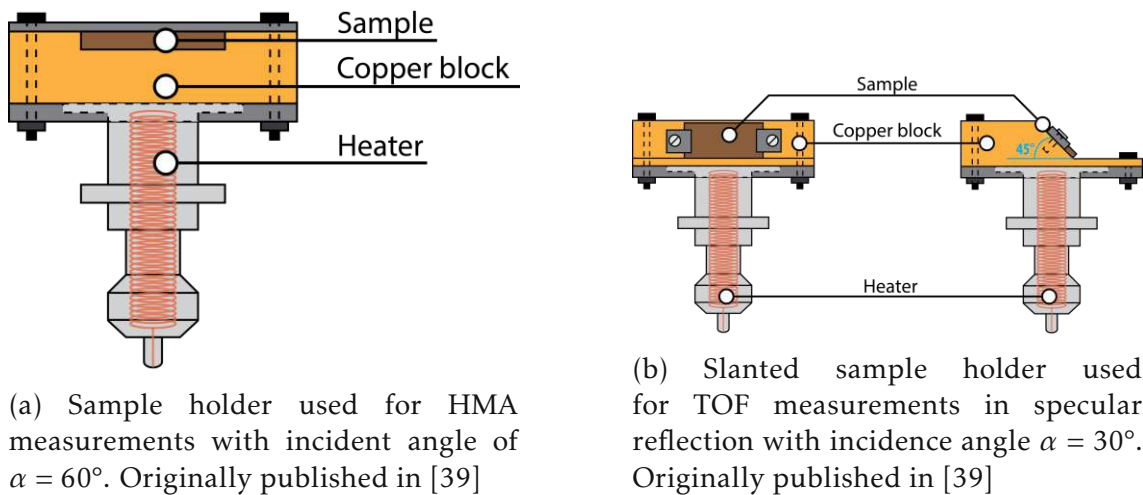
Figure 23

stainless steel ring and two screws as shown in figure 23. The sample holder is cleaned with an ultrasonic cleaner using acetone. One of the advantages of working with HOPG is, that the surface can be mechanically exfoliated with adhesive tape. If performed carefully, this procedure provides not only a clean and planar surface but even removes any ambient contamination on the surface. It is of utmost importance to introduce the prepared sample into vacuum as soon as possible to avoid eventual contamination.

For in-situ cleaning, the sample is annealed at a maximum temperature of about 400°C at a residual gas pressure of $10^{-9} mbar$ to $10^{-8} mbar$. A variable DC voltage is applied to the heating coil contacts of the sample holder. This causes a current to flow which heats up the specimen holder and subsequently the specimen. The temperature can be measured using a thermocouple mounted in the analyser chamber. As a result of the heating process, deposited impurities gas out of the surface, which increases the residual gas pressure in the analyser chamber. In order not to endanger the mounted devices, a well-established method is to increase the voltage only in small steps and wait till the vacuum pumps pumped down to a low enough residual gas pressure. This procedure ensures most of the deposited contaminants to be evaporated and pumped by the vacuum pumps without causing damage to the sample.

To verify the purity of the sample, a REELS spectrum was measured, as shown in figure 24. The red curve (after annealing) shows a more sharp and distinct spectrum, indicating a clean and ordered sample. Whereas the black curve (before annealing), the proportion of incoherent inelastic scattering is significantly higher, indicating an impure and disordered crystal.
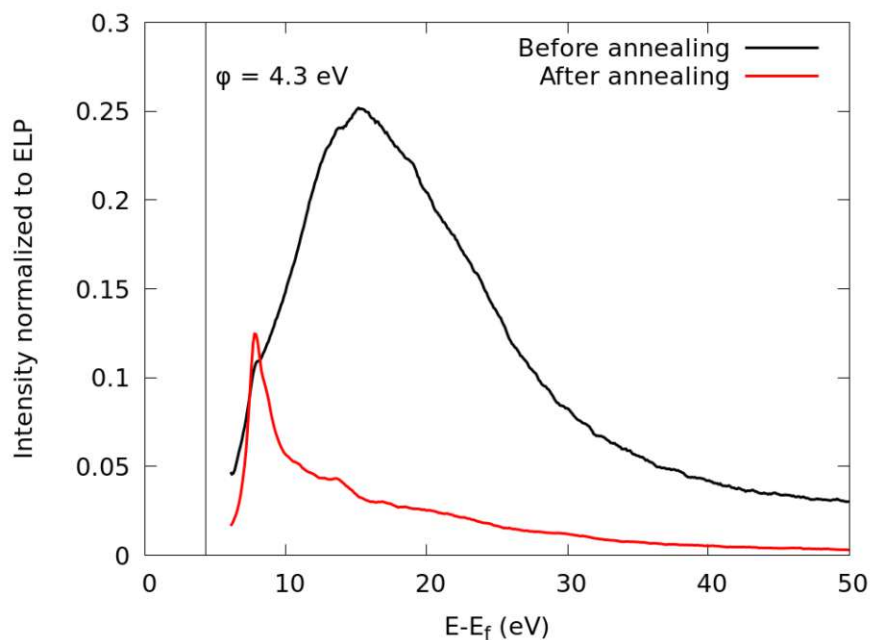

Figure 24: REELS spectra of HOPG with primary energy of 173eV and acquired with the HMA before (black) and after (red) annealing. Intensities are normalised to the elastic Peak (ELP) hight [39].

4.2 Energy scale of Reference

In electron scattering experiments, where both secondary and back scattered primary electrons are measured in a single spectrum, one must characterise the used energy scale of reference. Firstly, the kinetic energy of the impinging primary electrons are defined, taken three processes in to account. Firstly, section 4.2.1 discusses the contact potential difference (CPD) between two electrically attached metals. In section 4.2.2 the influence of the acceleration voltage on the kinetic energy is discussed in detail. The electron generation process itself also contributes to the kinetic energy of the primary electrons and is covered in detail in section 4.2.3. After the discussion of the kinetic energy, the potential distribution of the SE2ELCS spectrometer is presented in section 4.2.4 and a full energy scale of reference is established.
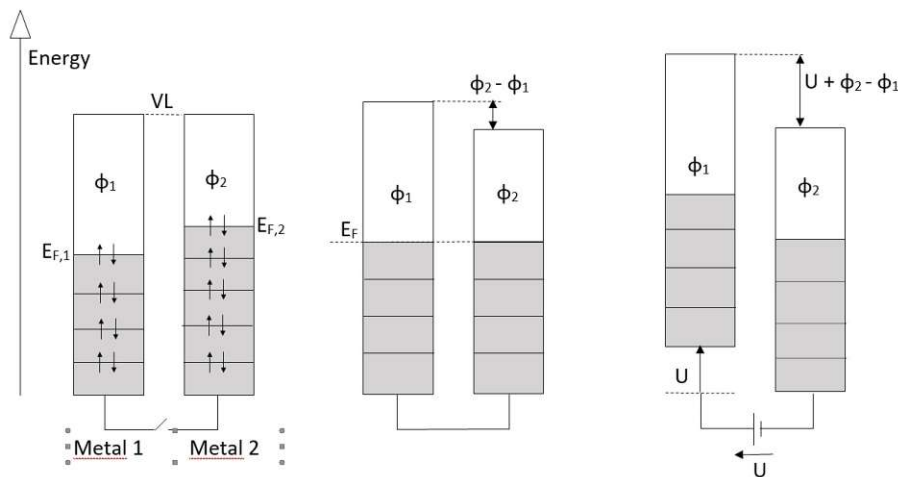
4.2.1 Contact potential

Figure 25: Schematic illustration of the contact potential difference of two metals. A metal contains filled electron states (gray areas) up to the Fermi level E_F and empty states above (white areas with the height of the work function $\phi_{1,2}$. Left: Two electrically isolated metals with different work functions have different Fermi levels $E_{F,1} \neq E_{F,1}$. Centre: Two electrically connected metals share a common Fermi level in thermodynamic equilibrium. Right: Applying an electrical voltage to metal 1 leads to a shift in the corresponding Fermi level and therefore also to a change in the CPD.

The theory of contact potentials is known since the late 18th century and was discovered by Alessandro Volta. Two electrically isolated metals with different work functions ϕ_1 and ϕ_2 share a common vacuum level (VL) [7–9], as shown in the left hand side in figure25. The vacuum level is defined as the energy of a free and stationary electron in a perfect, field-free vacuum outside the

material and the work function is defined as the energy required to move an electron from the Fermi level E_F to the vacuum level. When two metals are electrically attached to each other (either by direct contact or by conducting wires), electrons will flow from one metal to the other. Thereby, the direction of flux is from the higher (metal 2) to the lower (metal 1) Fermi level $E_{F,2} \rightarrow E_{F,1}$. As a consequence, the Fermi levels will equalise until they reach $E_{F,1} = E_{F,2}$. Once the net flux of electrons stops, the system is in thermodynamic equilibrium. Electrons will accumulate in the metals with the lower Fermi level, resulting in a potential difference, the so-called contact potential difference (CPD) or contact electrification. The height of the potential difference $\Delta\phi$ is given by the difference in work functions: $\Delta\phi = \phi_2 - \phi_1$ (see centre of figure 25).

Applying a bias voltage V to a metal causes a shift in the Fermi level by $E_F + qV$, where q is the charge of the electron. This shift can be used to control the CPD between two metals and subsequently to control the potential energy step between them (see right hand side in figure 25). This produces the operating principle of the acceleration voltage V_{Acc} of the electron source. Electrons generated by the e-gun have an energy close to the vacuum level of the emitting cathode. However, by applying a voltage to the cathode, the electrons are accelerated towards the sample and hit the sample with the energy

$$E_0 = q V_{Acc} + \phi_{sample} - \phi_{gun} \quad . \tag{49}$$

The following two sections will discuss the acceleration voltage and the energy levels in the thermionic electron generation process in detail.

4.2.2 Acceleration Voltage

The kinetic energy of an electron is mainly determined by the so-called acceleration voltage. Non-relativistic charged particles with charge q and velocity $\vec{v}$ feel the Lorentz force $F = q(\vec{E} + \vec{v} \times \vec{B})$ in the presence of electric $\vec{E}$ and magnetic $\vec{B}$ fields. In the classical approximation, this equation can be used to describe the kinematic of electrons. In a conservative electrostatic field[4] the work done by a charged particle is independent from its trajectory and depends only on the potential difference between the starting point P_1 and the end point P_2, resulting in an acceleration voltage $V_{acc} = \phi(P_2) - \phi(P_1)$. The potential difference causes the acceleration or deceleration of electrons to a certain energy. By applying a variable DC voltage between the electron source and the sample, one can control and specify the energy of electrons.

---

[4] $\frac{d\vec{E}}{dt} = 0$ and $\nabla \times E = 0$

4.2.3 Thermionic emission of electrons

In addition to the acceleration voltage, the electron generation process itself contributes to the kinetic energy [10–14]. As mentioned in chapter 4.1.3, a thermionic electron source was used during the experiments in this thesis. Due to the high temperatures that can occur in such an apparatus, one needs to consider a correction of the kinetic energy including the energy spread of the emitting electrons. Electrons in the solid state can be described using the free electron model. In this model electrons are considered quasi free particles forming a Fermi gas and thus following the Fermi-Dirac statistic. This theory states that at a temperature of $T = 0K$, every electronic state up to the Fermi level E_F is filled and empty if above E_F. At temperatures $T > 0K$ this behaviour changes and states above the Fermi level start to be partially occupied. If one increases the temperature even further, states above the vacuum level can be occupied in a reasonable amount, resulting in a thermionic electron emission (TEE). If an electron reaches such a state, it is allowed to leave the solid, since its energy is sufficient to overcome the work function of the material.

The energy of electrons generated via a thermionic electron source is close to the vacuum level of the emitting cathode. However, because of the high temperature of over 2000K, the emission current and the energy distribution depend on the temperature inside the e-gun. The emitted current density J is given by Richardson-Dushman's law in integral form[13]:

$$J = \int_0^\infty \frac{4\pi m q}{\hbar^3} \frac{E - \mu - \phi}{1 + e^{\frac{E-\mu-\phi}{k_B T}}} H(E - \mu - \phi) dE , \qquad (50)$$

where q, m are the charge and mass of an electron, $\hbar$ is the reduced Planck's constant, E is the kinetic energy above the vacuum level, μ is the chemical potential and is in this work equal to the Fermi level E_F, ϕ is the work function, $H(x)$ is the Heaviside step function and T is the temperature of the cathode [12, 13]. The electron emission intensity for any arbitrary energy $E > E_F + \phi$ is given by

$$\frac{dJ}{dE} = \frac{4\pi m q}{\hbar^3} \frac{E - E_F - \phi}{1 + e^{\frac{E-E_F-\phi}{k_B T}}} H(E - \mu - \phi) . \qquad (51)$$

Equation 52 defines the thermionic electron energy distribution (TEED) and it gives the thermal energy spread of the emitted electrons. Figure 26 schematically illustrates the TEED for $T = 10K, 300K$ and $2200K$. The TEED's maximum is

given by

$$\frac{d^2J}{dE^2} = 0 \tag{52a}$$

$$E_{max} = E_F + \phi + k_B T + W_n\left(\frac{1}{e}\right) \quad , \tag{52b}$$

where E_{max} is the energy at the maximum and W_n is the Lambert W function with integer the $n \in \mathbf{Z}$. Assuming only real and positive values for the energy, the Lambert W function results in $W_0\left(\frac{1}{e}\right) = 0.278...$. Thus, the maximum of the TEED is given by

$$E_{th} = E_F + \phi + 1.28 k_B T \tag{53}$$

and will be referred to as thermionic energy shift E_{th}. The most probable energy at which electrons are emitted at a emission temperature $T_{emission} = 2200K$ is about 0.24eV above the vacuum level. For the scope of this work, it is sufficient to consider the maximum of the TEED in the energy scaling process since this will directly cast to the maximum of the elastic peak in the energy spectra.

TEED at $T_{emission}$=10K, 300K and 2200K and ϕ = 4.1eV

/home/ziegler/gitrepos/philippbachelor/data/Sonstiges
TEED.g
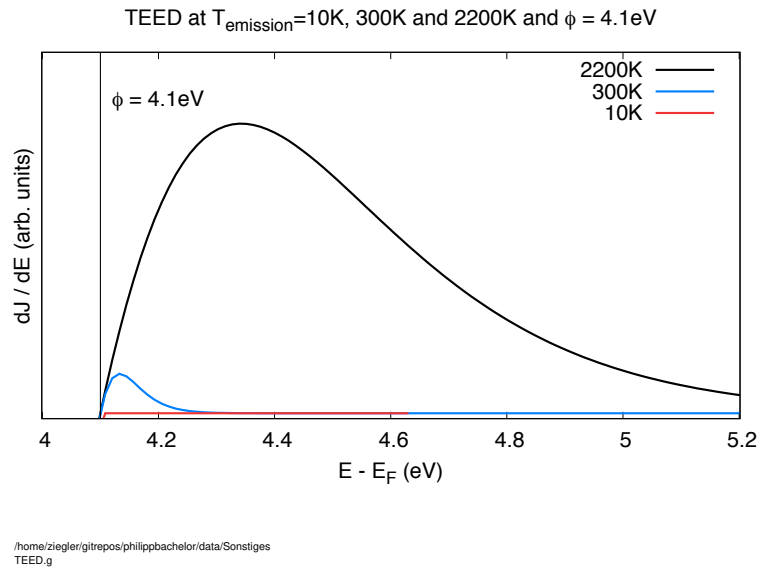
Figure 26: Theoretically predicted thermionic emission energy distribution of an electron gun with a work function $\phi = 4.1eV$ at different emission temperatures. As predicted, the maximum of the TEED shifts with increasing temperatures. At very low temperatures, the electron emission is almost fully suppressed.

4.2.4 Potential distribution in the SE2ELCS

As shown previously, the value of the kinetic energy of electrons depends on the respective energy scale of reference. Generally, the reference
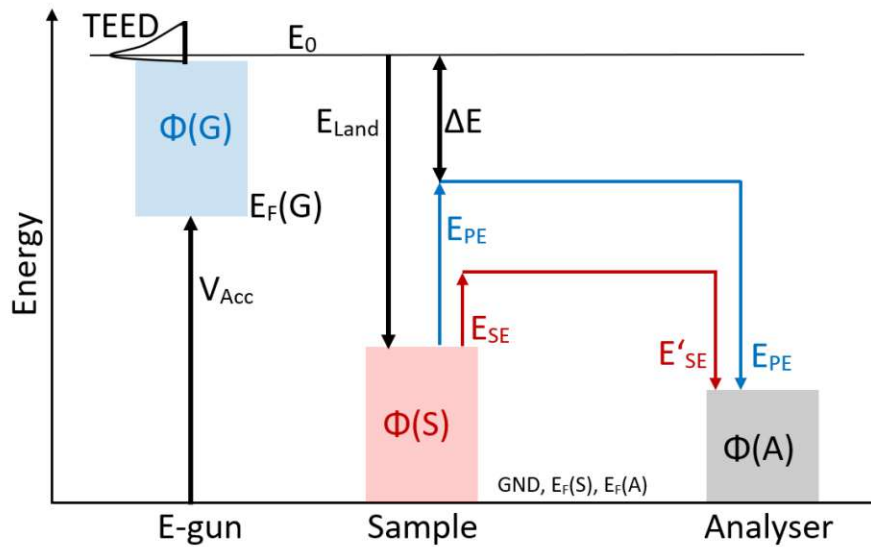
48

Figure 27: Energy level diagram of the used components. The acceleration voltage shifts the Fermi level of the electron gun by V_{Acc} and on top of the vacuum level, a schematic TEED indicates the energy spread due to the high temperatures in a thermionic electron gun. E_{PE} and E_{SE} represent the kinetic energy after leaving the sample where the corresponding primed quantity refers to the "detected" energy.

energy is the vacuum level of the emitting material. However, in electron scattering experiments, this principle no longer applies, because both primary and secondary electrons are detected and they are emitted from different materials with different work functions. However, owing to the fundamental indistinguishability of quantum particles, it is no longer possible to be certain whether an electron is a reflected primary electron or an emitted secondary electron. Thus, it is no longer clear to which energy reference point, the kinetic energy is associated with. In general, the choice of the energy reference point for the energy has no influence on the underlying physics. One thus has a certain freedom defining the energy reference point. There exist several valid approaches where, for instance, the Fermi level or the vacuum level of the analyser is taken as an energy reference point. In the framework of this thesis, the energy of an electron is always referred with respect to the vacuum level of the sample, unless it is specifically stated otherwise. As a consequence, the energies directly correspond to the (unoccupied) vacuum band structure of the target material.

The potential distribution of the SE2ELCS spectrometer is given in figure 27. The surface of both the HMA and the TOF analyser are covered with the same graphite coating, and hence, they are to be treated equally in terms of their energy scaling. All three components are electrically attached to each other and

connected to the common ground (GND) level. The Fermi level of the e-gun is shifted by the acceleration voltage V_{Acc}.

Considering the acceleration voltage V_{Acc}, the contact potential difference (CPD) and the thermionic energy shift E_{th}, one can define the kinetic energy of the impinging primary electrons with respect to the vacuum level of the sample (the so called landing energy E_{land}):

$$E_{Land} = qV_{Acc} + \phi_s - \phi_g + E_{th} \quad , \tag{54}$$

where q is the charge of the electron, ϕ_s, ϕ_g are the work function of the sample (s) and the e-gun (g). The work functions of the materials in use are given in table 4. The energy of the elastically back scattered electrons is given by

$$E_{elastic} = qV_{Acc} + \phi_a - \phi_g + E_{th} \quad , \tag{55}$$

where ϕ_a is the work function of the analyser. The energy in the elastic peak is independent of the target's work function, since in conservative electrostatic fields, the energy is only dependent on the potential difference between the starting and end point of the trajectory.

Assuming an incoming primary electron (PE) with energy E_{Land} hits the surface of the target and undergoes an inelastic single scattering with a bound secondary electron (SE). The energy of the PE and SE after the energy transfer ΔE is given by

$$E_{PE} = E_{Land} - \Delta E \tag{56a}$$

$$E_{SE} = E_b + \Delta E - \phi_s \quad , \tag{56b}$$

where E_b is the binding energy. Note that the binding energy is by definition negative with respect to the Fermi level. If $E_{SE} > 0$, the electron owns sufficient energy to overcome the work function and will eventually leave the solid, whereas otherwise it will remain as a hot electron inside the solid. The kinetic energy of secondary electrons is given by

$$E'_{SE} = E_{SE} + \phi_a - \phi_s \quad . \tag{57}$$

	HOPG	Tantalum (e-gun)	Graphite (Analyser)
$\Phi(eV)$	4.6	4.1	4.2

Table 4: Work function of materials used in the SE2ELCS experimental setup.

5 Experimental results

The main data sets in this work concern the double differential inelastic very low energy electron diffraction (IVLEED) spectra of highly orientated pyrolytic graphite (HOPG). These data are acquired by measuring full energy range spectra at varying landing energies in the range of 10-200eV for two different specular reflection geometries. For the interpretation of this complex data set, the typical features of an HOPG energy spectrum at a given landing energy will be presented and discussed in chapter 5.1. Section 5.2 then discusses the elastic IV curves of HOPG, i.e., the intensity of the elastic peak as a function of the landing energy. After the discussion of the single differential data sets, the full double differential IVLEED curves will be presented and analysed in section 5.3.

5.1 Single HOPG energy spectrum

Firstly, a single energy spectrum is analysed to study the typical effects that can occur and how they are determined in a spectrum. An energy spectrum, as used in this work, consists of (in-)elastically backscattered primary and emitted secondary electrons and contains the intensity as a function of the detected electron energy with respect to the vacuum level of the target. Figure 28a shows a characteristic energy spectrum for HOPG, recorded with the HMA in 60° specular reflection geometry at a landing energy $E_{Land} = 450eV$. It can be grouped into four characteristic categories: the elastic peak (yellow), discrete energy losses (blue), plural scattering (grey) and secondary electrons (red).

- The elastic peak (ELP) or zero-loss peak (ZLP) consists of elastically backscattered primary electrons. These electrons will exclusively participate in elastic collisions with the screened coulomb field of the nuclei. Energy losses caused by Bremsstrahlung can be neglected since the energy is well below the keV range. Moreover, the energy transfer during the collision with the nucleus can be neglected since the mass of the nucleus is four to five orders of magnitude larger than the mass of an electron. The energy of the ELP changes linearly with the landing energy and the shape is primarily determined by the thermionic electron energy distribution (TEED), as shown in chapter 4.2.3. When the time of flight spectra are transformed into energy spectra, the width of the elastic peak
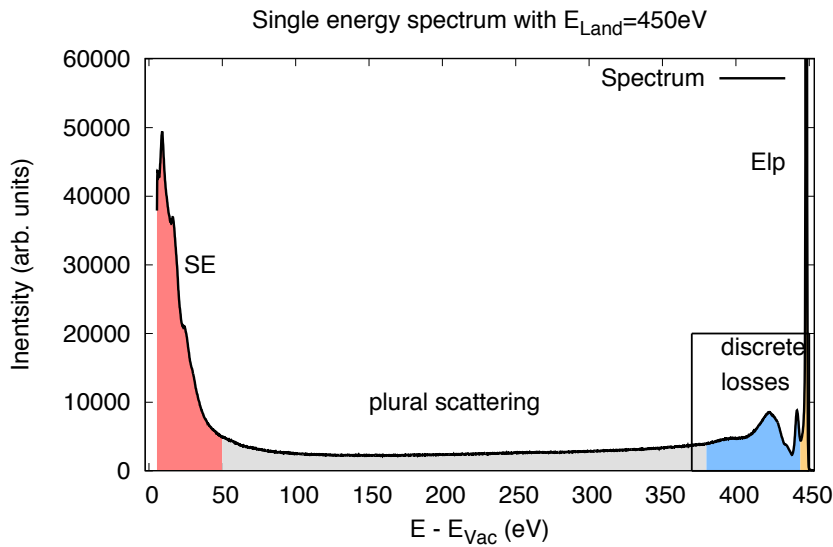
Single energy spectrum with $E_{Land}=450eV$

(a) Electron energy spectrum of annealed HOPG with $E_{Land}=450eV$ in 60° specular reflection using the HMA[a]. True secondary electrons (red), plural scattering (gray), discrete energy losses (blue) and elastic peak (yellow). The frame indicates the zoomed-in section in panel b). The elastic peak is cut off for a better scaling.

[a]This spectrum was measured by Vytautas Astašauskas on 6th April 2018
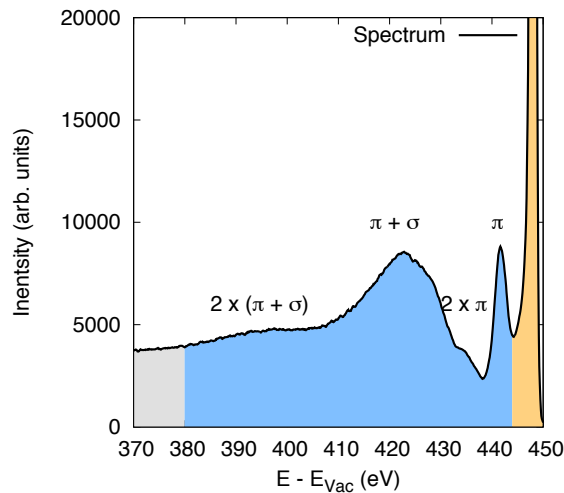
(b) Zoomed section of the black frame in a). Strong peaks at an energy loss of 6 and 25 eV referring to single excitation of π and $\pi + \sigma$ plasmons. Although the intensity in the plural excitation peaks is lower, they are still observable.

Figure 28: Single electron energy spectrum.

depends on the landing energy, resulting in the broadening of the peak at higher energies.

- The discrete energy losses seen in figure 28a arise from the excitation of plasmons in the target. Thereby, the energy loss is an n-fold of the plasmon resonance energy $E = \hbar\omega$ with $n \in \mathbf{N}$. In graphite samples, two types of plasmons exist: the π plasmon and the $\pi + \sigma$ plasmon. The prefixes indicate the associated orbitals in resonance [52]. The π plasmon is a collective oscillation of electrons in the π bond and therefore exists between the carbon atoms in the honeycomb structure. Its characteristic energy is $E_\pi = 6eV$. The $\pi + \sigma$ plasmon is an oscillation of the hybridised sp^2 orbital between the atomic layers and has a characteristic energy of $E_{\pi+\sigma} = 25eV$. The plasmon excitation energy is independent of the energy of the primary electron, and therefore, the excitation of a single plasmon gives rise to a discrete energy loss of the primary electron. In the energy spectrum, the discrete energy losses can be observed as peaks at $E_{Elp} - \hbar\omega$, and therefore, plasmonic energy losses are directly linked to the elastic peak. Besides single plasmon excitations, plural excitation also occurs in lower intensity, as shown in the zoomed section of figure 28b.

- In contrast to back scattered electrons, the secondary electrons are generally independent of the landing energy and follow the curve shown in figure 28a. The structure in the SE region is directly linked to the (vacuum) band structure of the target and will be explained in more detail in section 5.3.2. During inelastic collisions, secondary electrons are excited to higher energy states and eventually to states above the vacuum level. In anisotropic targets, the secondary emission depends on the observation angle between the surface of the target and the analyser. In an energy spectrum, back scattered primary electrons and secondary electrons cannot be distinguished, however, electrons below 50eV are referred to as true secondary electrons by convention.

5.2 Very low energy electron diffraction

As stated in the introduction, very low energy electron diffraction (VLEED) is a widely used method to investigate the unoccupied electron states in the band structure above the vacuum level. In VLEED measurements one only considers elastically scattered electrons, since the energy and the parallel component of the momentum are conserved during the coupling process between the vacuum wave functions and the Bloch waves [27, 39, 53]. However, this process is certainly

accompanied by inelastic scattering effects. The IVLEED measurements provide experimental data concerning both elastic and inelastic scattering, creating a causal link between them. Both aspects will be discussed in the following section.
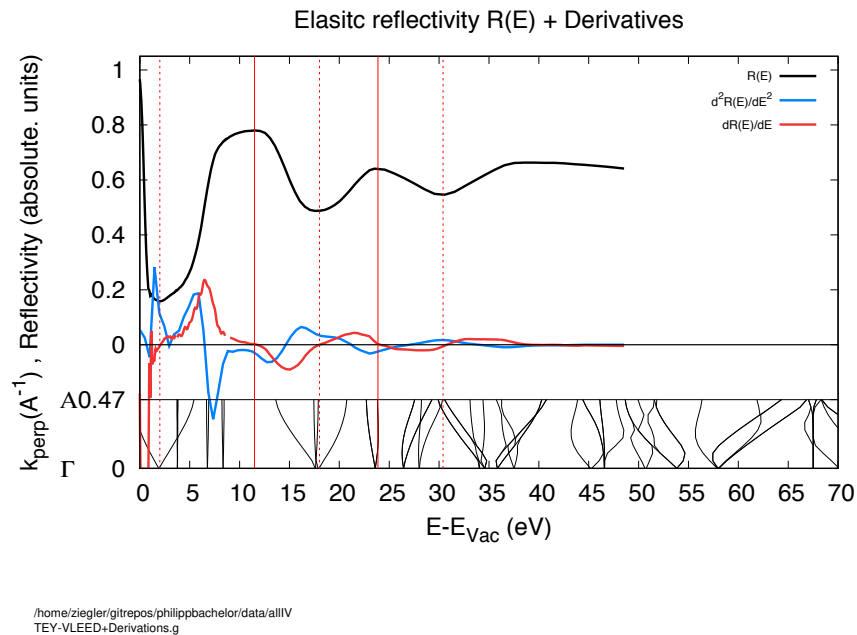
5.2.1 TEY

Figure 29: TEY curve of Bellissimo [36] compared to its first and second derivative and the band structure in ΓA direction (bottom). The data was measured in absolute units and at perpendicular incidence angle of the electron beam. The vertical lines indicate the maxima (solid) and minima(dashed) of the TEY curve.

Experimental VLEED data for HOPG was provided by Alessandra Bellissimo via a total electron yield (TEY) measurement [28, 29, 36]. The experiment was performed at perpendicular incidence and was measured in absolute units. In the region below 50eV, the TEY resembles mainly elastically and inelastically backscattered electrons, as the primary energy is not sufficiently high to generate a significant number of secondary electrons. Therefore, the TEY is very sensitive to the elastic reflectivity of primary electrons. Figure 29 shows the TEY curve (black) and its derivatives (blue and red) compared to the band structure along the ΓA direction. Dotted and solid vertical lines indicate the minima and maxima of the TEY curve. The minima at 2-6eV and 15-21eV align well with the interlayer states of graphite. This is consistent with the considerations of the matching formalism of chapter 3.1, as the primary electrons can travel far into the crystal and therefore have low probability of scattering back elastically. Therefore, it

can be concluded, that interlayer states play a decisive role in the formation of minima in the TEY curves.

The maximum at 7-14eV aligns with a wide band gap in the ΓA band structure. From the matching formalism, one would expect that the elastic reflectivity would be unity because in band gaps no Bloch waves exist that can couple to the vacuum wave functions. However, the reflectivity peaked at 0.8. Bellissimo wrote in her PhD thesis: *"However, due to the formation of surface states or to the presence of the interlayer states the external wave-function matching with these states decay exponentially into the interior of the crystal at energies where Bloch states are forbidden"*[29], which is in good agreement with the literature which states, that the primary electron can couple to surface localised states whose wave function decay into the crystal [25, 30–34]. The description via surface states is equivalent to the description that wave functions have an exponentially decreasing but continuous transition into forbidden regions, similar to Lambert-Beer's law for electrons, where the characteristic length is given by the imaginary part of the inner potential. his results in a high reflectivity, although not equal to unity.

The data collected in this work support the claim that electrons can enter forbidden regions, by providing reflected electron energy loss spectroscopy (REELS) spectra. Figure 30 shows two REELS spectra of HOPG, where the red spectrum is taken at a landing energy in a band gap and the black spectrum is taken at an energy corresponding to a minimum in the IV curve. Both curves are normalised to the elastic peak intensity. The graph shows clearly that waves which fall into forbidden regions (red spectrum) have a finite, non-zero intensity in the energy loss part. The intensity is by orders of magnitude lower, when compared to waves which match with allowed Bloch states (black spectrum). The lower energy loss intensity in forbidden regions indicates that external electrons can enter into the solid, but can travel only short distances.

In summary, this work provides data to qualitatively understand that the first order approximation of the matching formalism for VLEED fails in band gaps. It was shown by Bellissimo that the elastic reflectivity does not go back to unity in band gaps. In our REELS spectra it was shown that the primary electrons do indeed enter the crystal in forbidden regions, however the intensity is by orders of magnitude lower as when the electron falls into an allowed Bloch state. Nevertheless, a direct and causal link to the undergoing mechanism could not be found in our data and more theoretical as well as experimental research is required.
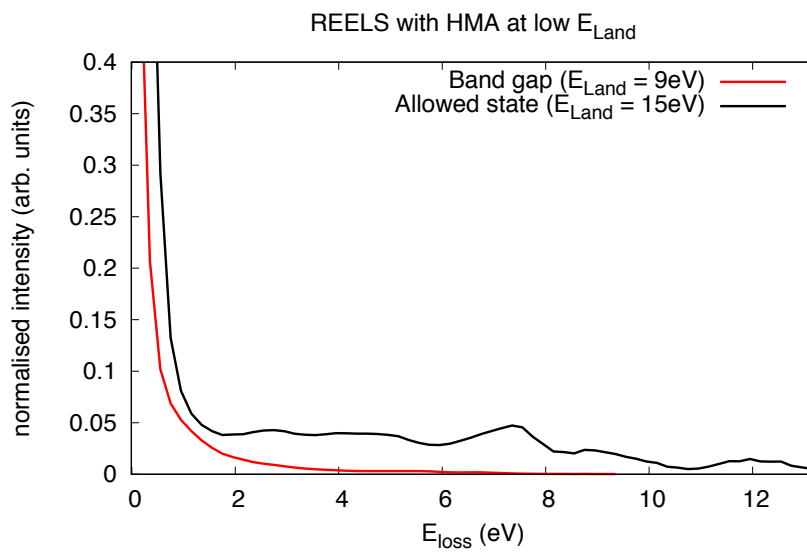
Figure 30: Red: REELS spectrum at E_{Land}=9eV corresponds to a strong maximum in the IV curve and aligns with a band gap in the ΓA band structure; Black: REELS spectrum at E_{Land}=15eV. The black curve corresponds to a minimum in the IV curve and the red one to a maximum. Both curves are normalised to the corresponding elastic peak height.

IV curves

The aim of the following chapter is to present two IV curves of HOPG, measured in different specular reflection geometries and discuss them with the findings of the aforementioned matching formalism for VLEED. The IV curves are obtained by plotting the elastic peak intensities as a function of the landing energy and hence, this curve directly corresponds to the elastic reflectivity of the primary electrons.

Figure 31 shows the IV curve, acquired using the TOF analyser at $\alpha = 30$

/home/ziegler/gitrepos/philippbachelor/data/allIV
0119VLEED+Derivation+Correctescale.g
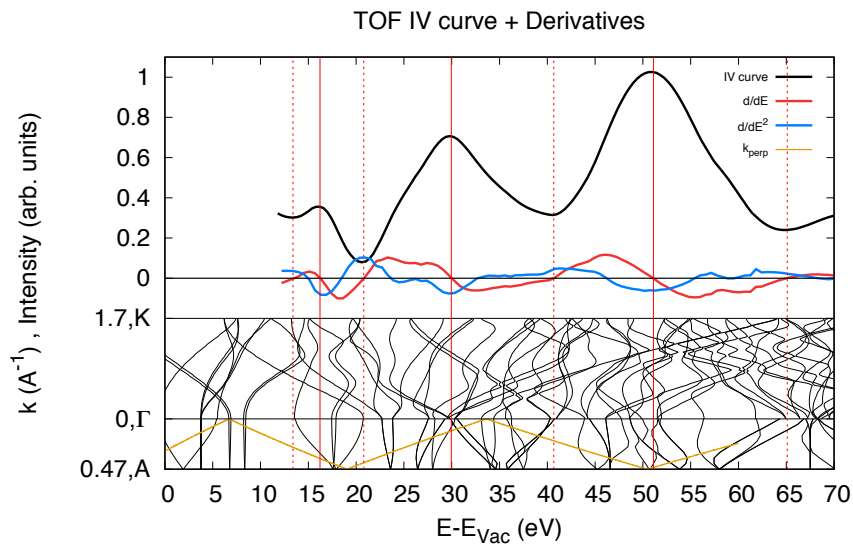
Figure 31: IV curve of the TOF(0119) measurement compared to its first and second derivative and the band structure in ΓA and ΓK direction (bottom). The vertical lines indicate the maxima (solid) and minima(dashed) of the IV curve. The orange line in the band structure indicates the perpendicular component of the momentum, calculated with equation 14.

incidence angle, compared to the band structure of HOPG in the ΓA and ΓK direction. The minima and maxima are again indicated using dashed and solid vertical lines and the derivations are plotted in red and blue and the perpendicular component of the momentum is plotted as a yellow line in the ΓA band structure. The maxima of this curve are located at 16eV, 30eV and 50eV, whereas the minima are located at 13eV, 21eV , 41eV and 65eV. The assignments of the maxima and minima to certain allowed and forbidden areas in the ΓA band structure can be misleading, as minima align with band gaps and maxima with allowed states respectively. Multiple effects can cause deviations in the expected

outcome. Firstly, the electron beam hits the surface no longer at a perpendicular angle. Therefore, a direct comparison to the ΓA band structure is no longer feasible, because the primary electron falls in states of non-high symmetry points in the band structure. Secondly, the broad band gap between about 5 and 13eV (which caused a strong peak of almost unity in the TEY curve) is not included in the present data set. Thirdly, it is not trivial to distinguish whether peaks are induced by the band structure or by Bragg scattering, as for instance, the maximum at 50eV can be either related to a Bragg peak (Bragg order n = 3) or to the band structure.

The IV curve acquired using the HMA at an incidence angle of $\alpha = 60°$ with
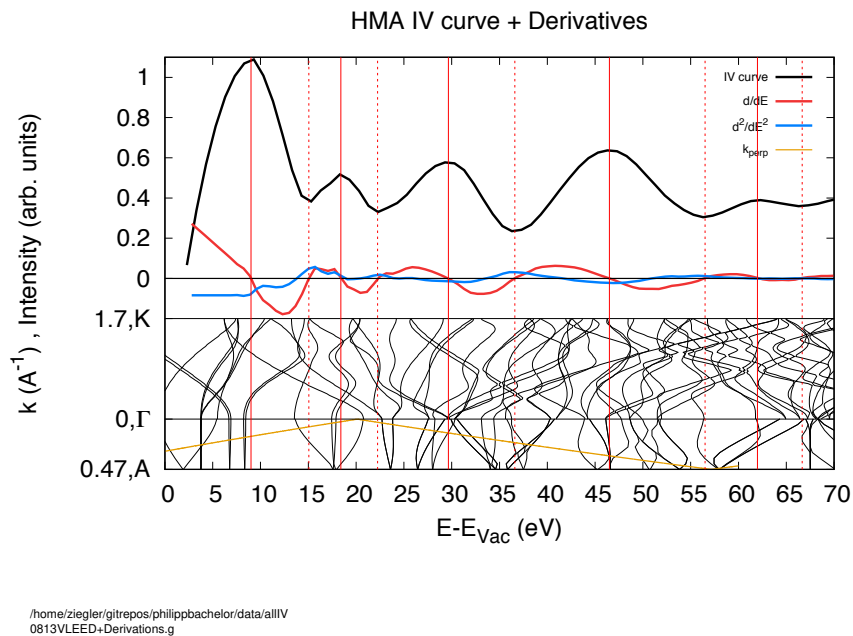
Figure 32: IV curve of the HMA(0813) measurement compared to its first and second derivative and the band structure in ΓA and ΓK direction (bottom). The vertical lines indicate the maxima (solid) and minima(dashed) of the IV curve curve. The orange line in the band structure indicates the perpendicular component of the momentum, calculated with equation 14.

respect to the surface normal is shown in figure 32. The maxima (indicated by solid lines) are located at 9, 18, 29, 47 and 63eV, whereas the minima are located at 15, 23, 37, 57 and 67eV. At the flat incidence angle of 60°, the comparison solely to the ΓA band structure can be misleading, however, the first maximum at $E - E_{Vac} = 9$eV aligns well with the broad band gap at $7 < E - E_{Vac} < 14$eV. This fit well with the prediction of the matching formalism. Although, peaks at higher energies cannot be assigned with certainty to individual regions in the ΓA
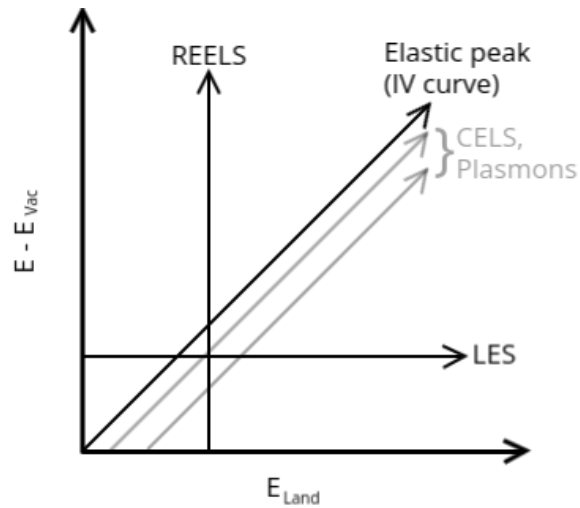
band structure.

5.3 IVLEED

Figure 33: Schematic illustration of an double differential IVLEED spectrum. The data are acquired by measuring a set of REELS spectra over a wide range of landing energies. A vertical cut corresponds to individual REELS spectra, where as horizontal cuts yield a novel spectrum type, the so called landing energy specta (LES). The elastic peak (ELP) at $E_{Land} = E - E_{vac}$ is located on the 45° diagonal and discrete energy losses are parallel to the elastic peak. A second novel spectrum type is the so called constant energy loss spectrum (CELS) which gives the intensity for constant energy losses as a function of the landing energy.

Very low energy electron diffraction and the matching formalism use exclusively elastically back scattered primary electrons and fully neglect inelastic events and emitted secondary electrons. However, elastic scattering is directly linked to inelastic scattering, as shown in chapter 3.3. Therefore, studying inelastically scattered electrons is essential to understand all the effects concerning the band structure. Secondary electrons can only leave the solid if they fill an unoccupied, allowed state in the band structure and are therefore well suited to the study of the unoccupied band structure above vacuum level. For this reason, double differential inelastic very low energy electron diffraction (IVLEED) spectra were measured in this work. Such measurements consist of a set of REELS spectra acquired over a wide range of landing energies. The individual REELS spectra were stacked so that the x-axis corresponds to the landing energy and the y-axis $E - E_{vac}$ to the energy of the detected electrons, respectively. The intensity is represented by a logarithmic colour scale. The double differential representation of the data can be used to obtain the intensity of any contiguous path. Needless to say, not all of these paths are of physical
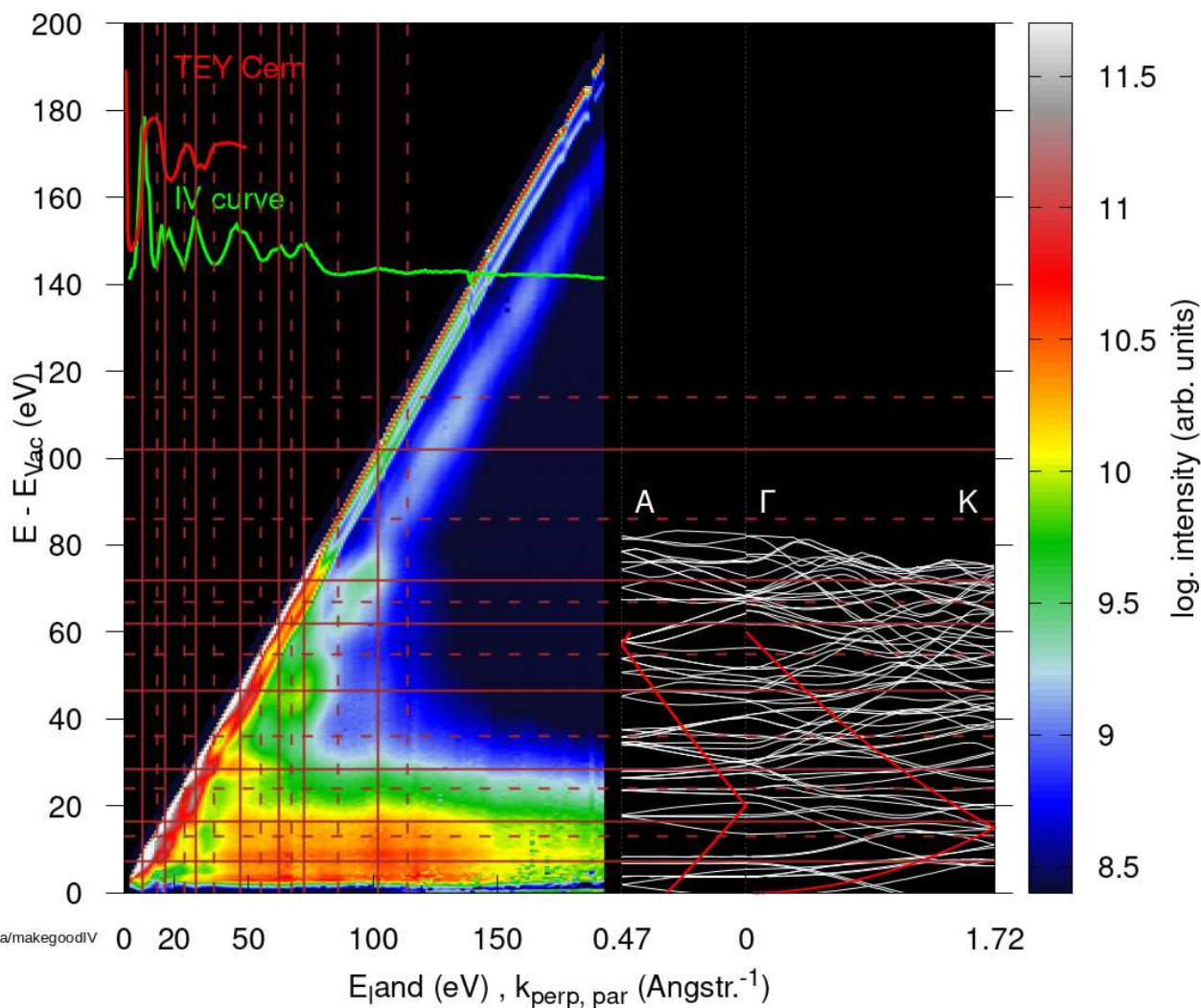
Figure 34: Result of IVLEED measurement of HOPG with HMA in 60° specular reflection on 13th Aug.2019. Note that intensity only exists below the elastic peak due to the conservation of energy. The top green line is the IV curve and for comparison, the red curve is the TEY curve from Bellissimo [29]. Vertical and horizontal lines: minima (dashed) and maxima (solid) of the IV curve. On the right panel, Band structure in $A\Gamma K$ direction (white lines) and the momentum of the incoming electron (red lines) calculated with 27b
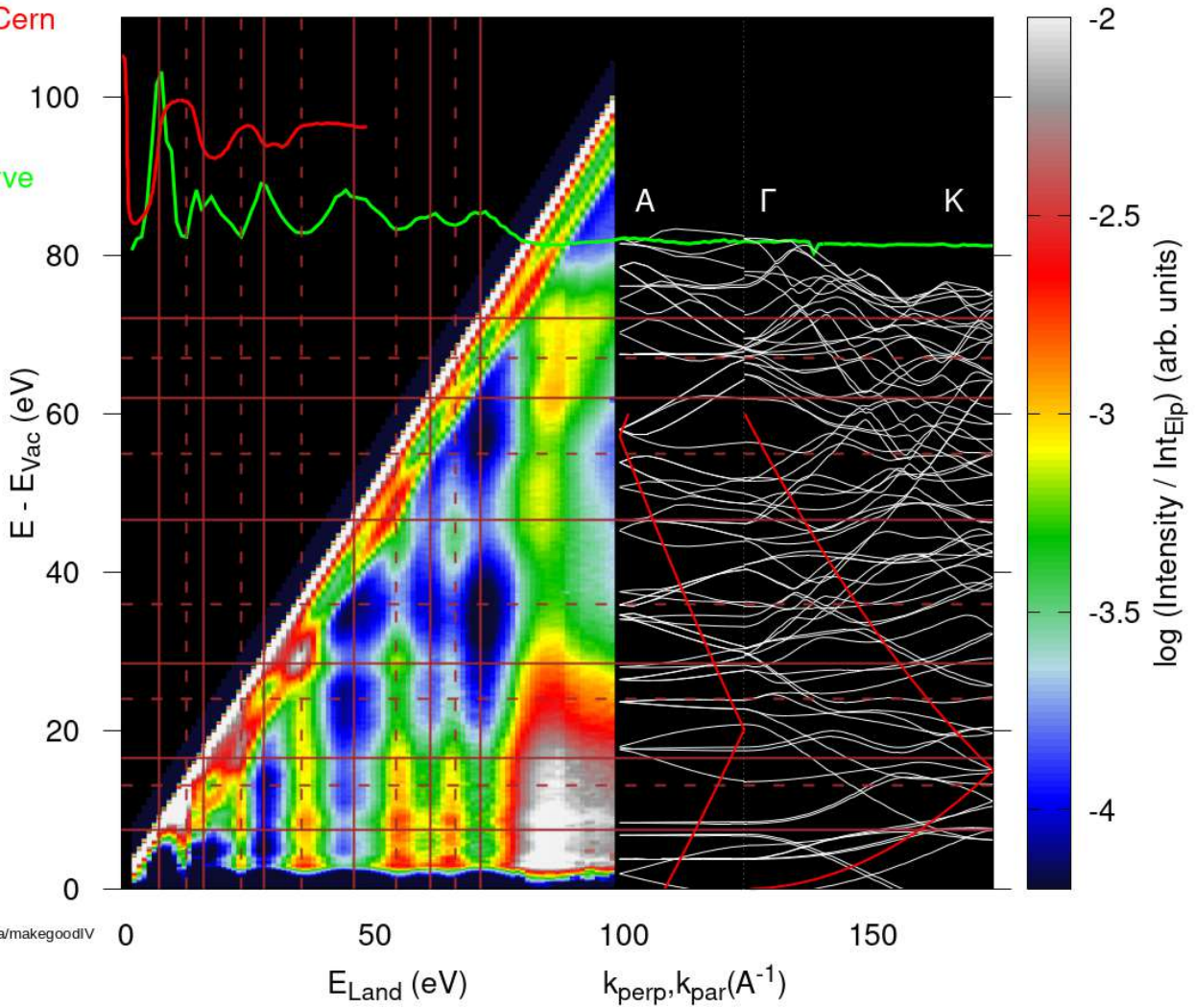
Figure 35: Normalised IVLEED data from previous figure. The intensity gives the ratio of intensity to the intensity of the elastic intensity in logarithmic colour scale. On top, IV curve (green) and TEY curve (red). Vertical and horizontal lines: minima (dashed) and maxima (solid) of the IV curve. On the right $A\Gamma K$ bandstructure (white) and momentum of the incoming electron in the solid (red).
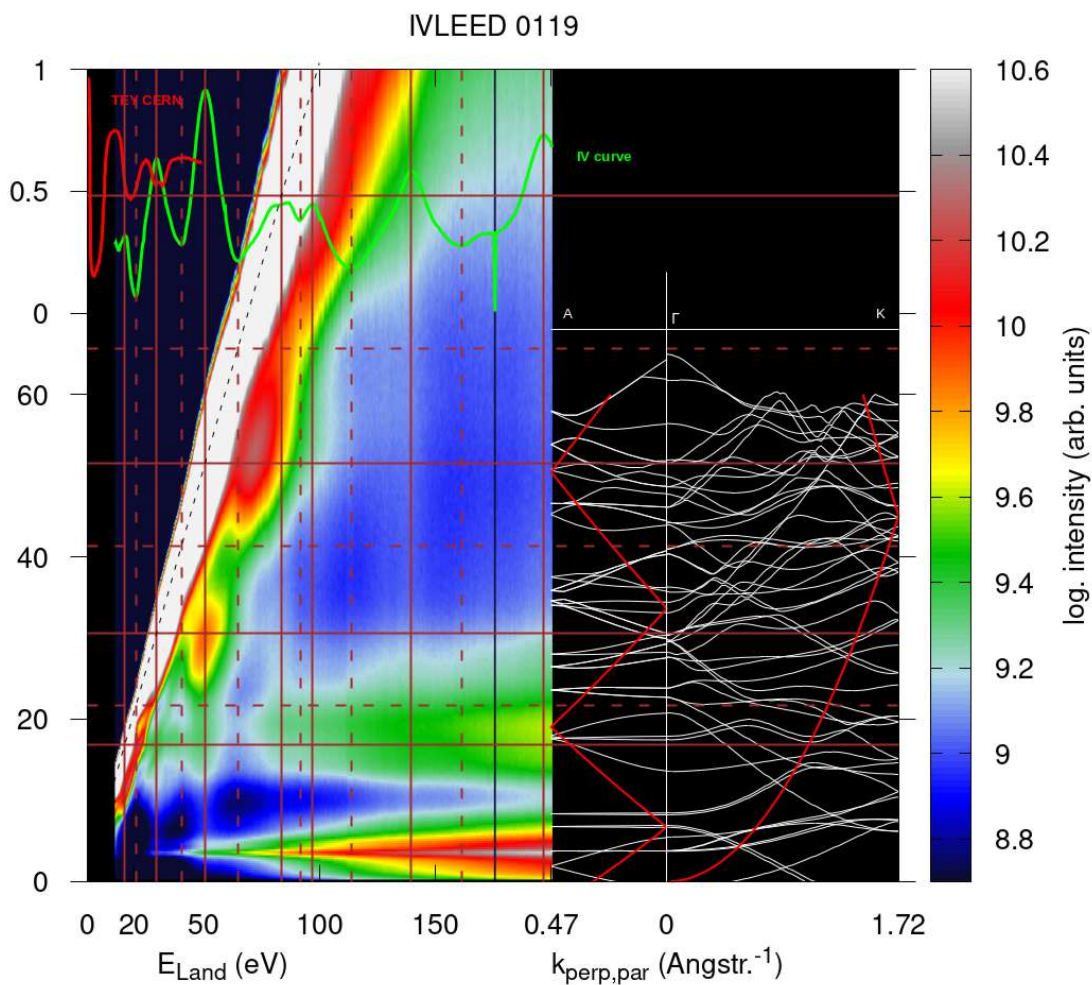
Figure 36: Result of IVLEED measurement of HOPG with TOF in 30° specular reflection on 19^{th}Jan.2019. Same scheme as in previous figures. Note that the elastic peak broadens at higher energies because of the conversion from time-of-flight spectra into energy spectra. This measurement was performed by Wolfgang Werner.
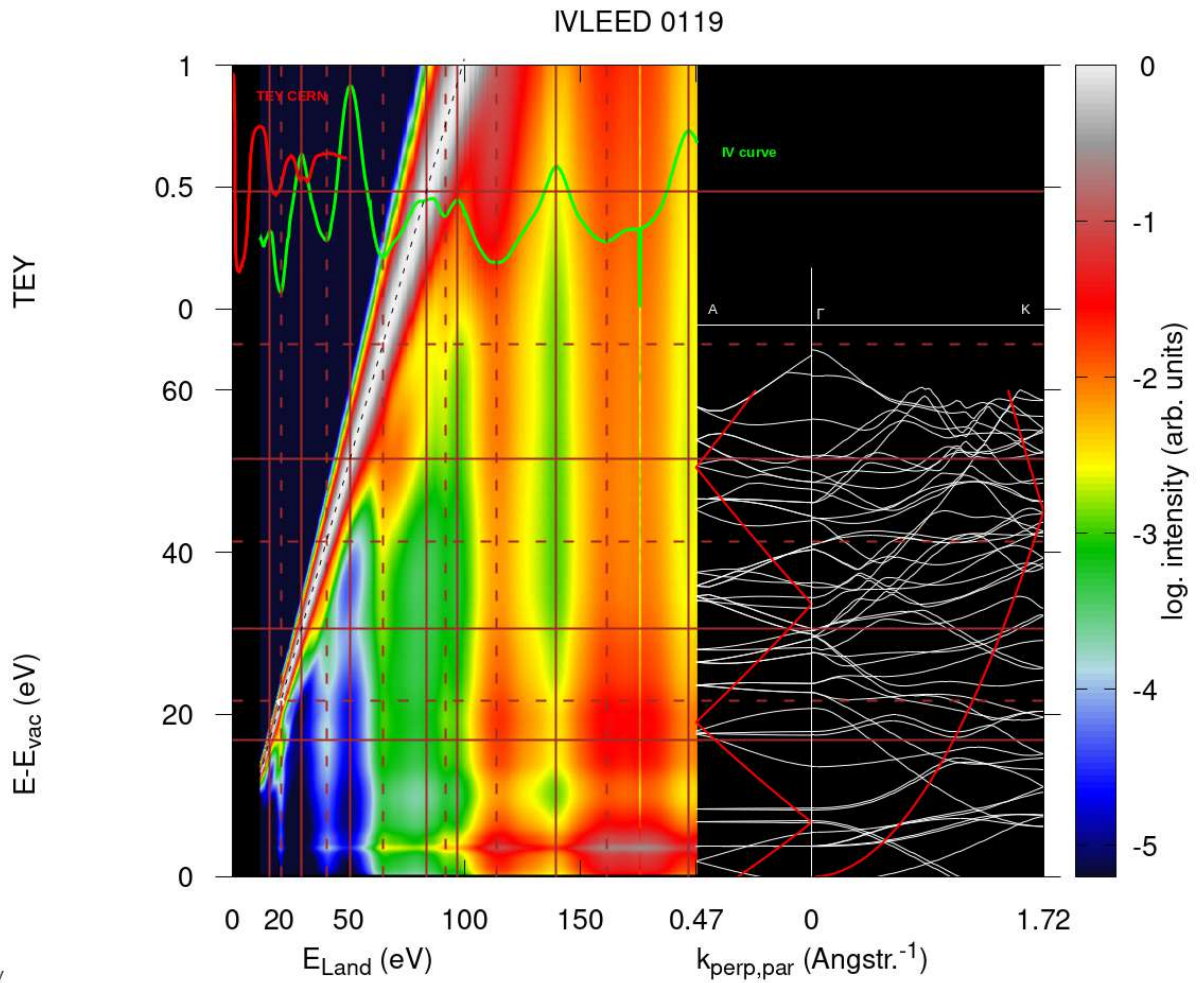
Figure 37: Result of nIVLEED measurement of HOPG with TOF in 30° specular reflection on 19^{th}Jan.2019. Same scheme as in previous figures. This measurement was performed by Wolfgang Werner.

relevance, however, some of these paths represent novel spectra that have not been found in the literature before. A schematic illustration of the representation format is shown in figure 33. The intensity along a vertical cut (i.e. $E_{Land} = const.$) through the spectrum yields a single REELS spectrum. A horizontal cut (i.e. $E - E_{Vac} = const.$) yields landing energy spectra (LES), which are a novel type of spectra. It gives the intensity of electrons at constant final state energy as a function of the landing energy. The elastic peak of the individual REELS spectra can be identified as the 45° diagonal. The intensity along this diagonal as a function of the landing energy is referred to as IV curve. Discrete energy losses (i.e. plasmon excitation) are identified as features parallel to the elastic peak. The intensity of constant energy loss as a function of the landing energy is referred to as constant energy loss spectrum (CELS). Thus, the CELS represent the intensity of a linear function parallel to the elastic peak but shifted to a negative ordinate. The C-source code for obtaining both LES (h2d) and CELS (2dfit) from the IVLEED data is presented in the appendix A.

Figures 34 and 36 show the IVLEED data recorded with the HMA and TOF, respectively. The brown vertical lines indicate the minima (dashed) and maxima (solid) of the IV curve (green, top). Horizontal lines are drawn at the cross section between the elastic peak and the vertical lines. This allows one to compare the IV curve to the band structure in $A\Gamma K$ direction (right hand side). Secondary electron effects are identified as horizontal stripes, as they occupy final states with a fixed energy $E - E_{vac}$. Normalising the data to the intensity of the elastic peak yields the ratio of inelastic to elastic scattering. The normalised IVLEED (nIVLEED) data are shown in the figures 35 for the HMA and in figure 37 for the TOF. The following subsections are devoted to the interpretation of these double differential data. At first, in chapter 5.3.1, the VLEED considerations of the previous chapter are extended to include inelastic scattering. Afterwards, in chapter 5.3.2 the mechanisms behind the secondary electron emission are presented and discussed. Chapter 5.3.3 discusses the discovery of a novel mechanism in which primary electrons suffer discrete energy losses that depend on the landing energy, which is in strong contrast to plasmonic excitation. Finally, chapter 5.3.4 discusses the transition between regions where band structure and Bragg scattering are dominant, respectively.

5.3.1   Inelastic VLEED

This chapter extends the VLEED interpretation of the previous chapter to also include inelastic scattering. First, figure 34 is considered, where the IV curve is plotted in the upper part. In the double differential spectra, the IV curve

2dfit specatra for various energy losses
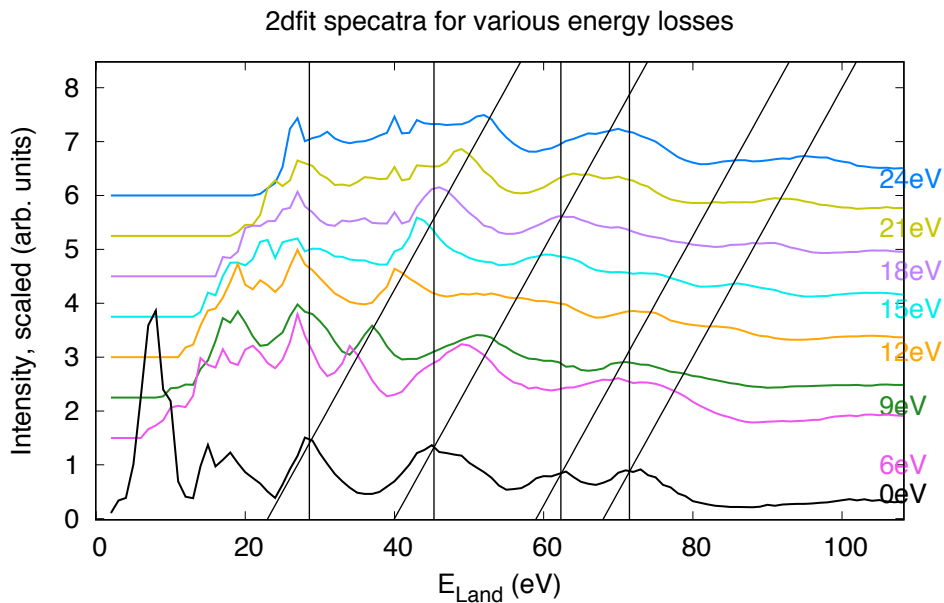
/home/ziegler/gitrepos/philippbachelor/data/2dfitauswertungen
08132dfitfinal.g

Figure 38: IV curve (black) and constant energy loss spectra (CELS) for energy losses ΔE from 6eV to 24eV, both taken from the HMA IVLEED data from figure 34. The vertical lines indicate the maxima of the IV curve and the diagonals indicate an energy shift of the maxima by ΔE. Note that the diagonals only serve as visual guidelines and should be used with caution

2dfit specatra for various energy losses
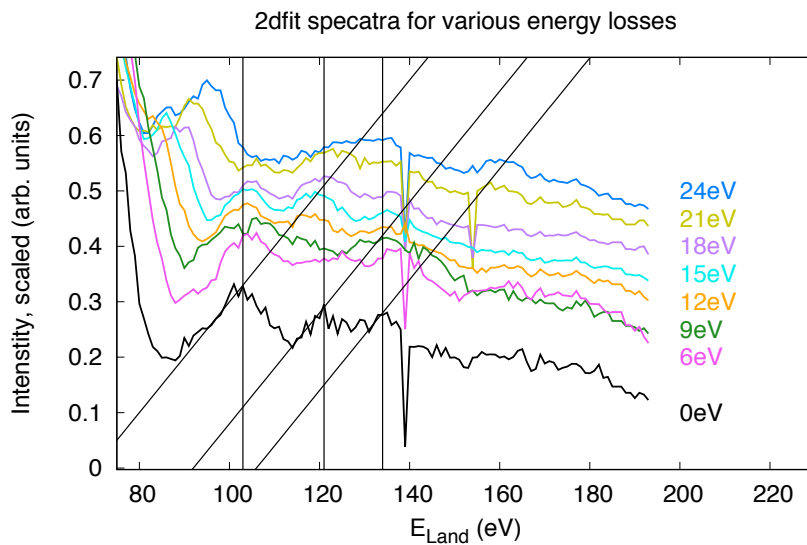
/home/ziegler/gitrepos/philippbachelor/data/2dfitauswertungen
08132dfitfinal2.g

Figure 39: Same scheme as in figure 38, but for higher landing energies.

corresponds to the intensity along the 45° diagonal. The brown verticals indicate the minima and maxima of the IV curve, and at the intersection with the elastic peak, horizontal straight lines have been drawn to provide a visual comparison with the band structure.

Generally, electrons that travel only a short distance in the solid have low probability of suffering high energy losses and vice versa for electrons that travel long distances in the crystal. Recalling the matching formalism, electrons which fall into a maximum of the IV curve are expected to travel only short distances in the solid. In first order approximation, electrons are not allowed to exist in regions of band gaps. However, in figure 34 a finite, non-zero intensity can be observed in the areas of band gaps ($7eV < E_{Land} < 14eV$), implying that electrons can indeed enter the solid and thus undergo inelastic collisions.

The nIVLEED spectrum in Figure 35 shows the ratio of inelastic to elastic intensity. It can be observed that t strong differences in the behaviour exist between the regions of minima and maxima of the IV curve. In IV curve minima (dashed vertical lines) electrons can penetrate easily into the crystal, resulting in more inelastic intensity per primary electrons and therefore a high intensity in the normalised data. Furthermore, high energy losses are more likely to occur in regions of minima in the IV curve (dashed vertical. In contrast, along the solid vertical lines (IV curve maxima), high energy losses are significantly less likely to occur. With the help of the horizontal lines, a comparison can be made with the band structure. Chapter 5.2 already covered the relation between IV curve and the band structure in detail. In short, it can be said that in regions of IV curve maxima (solid lines) external electrons have no or only few allowed states and are therefore driven out of the material, resulting in a high intensity in reflection geometry. In contrast, allowed Bloch states exist in regions of IV curve minima (dashed lines), thus permitting electrons to penetrate deeper into the material. Along the dashed vertical lines, one can observe that they have a certain fine structure. Thereby, local maxima form at intersections of dashed vertical lines with solid horizontal lines (e.g. at E_{Land} =57eV, 67eV and 80eV). This can be explained by the fact that electrons that fall into such a region of the band structure do not have an allowed state and are thus increasingly driven out of the crystal, resulting in a high intensity. In contrast, local minima can be observed at the intersection of two dashed lines, indicating that electrons occupy favoured states. Therefore, they penetrate deeper into the solid and have a higher probability of suffering further energy losses. A quantitative determination of the distances traveled at this point is impossible with the available data and further

research in this direction is required.

The (n)-IVLEED data from the TOF measurement (Figures 36 and 37) are consistent with the above interpretations.

Another way to interpret the data is to compare the elastic IV curve with constant energy loss spectra (CELS). Figure 38 shows the IV curve and several CEL spectra for the energy losses ΔE from 6 to 24eV in the low energy range, extracted from figure 34.

The vertical lines indicate the maxima of the elastic IV curve ($\Delta E = 0$eV) and the diagonals indicate a linear shift by the corresponding energy loss. The diagonals serve only as a visual guide and should therefore be used with caution. It can be seen in this graph that peaks form in some of the loss IV curves along the verticals. Suppose a primary electron with the energy E_{Land} hits a forbidden or weakly to vacuum coupling state of the band structure, resulting in a high elastic reflectivity. Electrons that lose the energy ΔE fall into other regions of the band structure. If allowed states exist for the inelastically scattered electrons, they can penetrate further into the solid, which reduces the intensity in the IV curves. However, if no allowed states exist, then a high intensity arises in the loss IV curves at E_{Land}.

Considering the diagonals, one can recognise that peaks shift linearly with the energy loss. Assuming that at energy E' exists an unfavourable region of the band structure, which results in a maximum in the IV curve. However, if an electron with $E_{Land} > E'$ loses energy such that $E' = E_{Land} - \Delta E$, the inelastic scattered electron falls in unfavoured regions, resulting in an observable peak. This leads to the fact that the peak shifts linearly with the energy loss ΔE in the loss IV curves.

Figure 39 shows the IV curves for the energy losses from 0 to 24eV in the high energy range. Because of the low and noisy intensities, interpretation in this region is impossible. At this energy, a transition between the band structure dominated and the Bragg scattering dominated region takes place.

At this point it is worth mentioning that these processes are fundamentally different from those in the inelastic interference models, although the peak formation suggests that they are. The models for inelastic interference involve a purely kinematic model, which describes the separation of Bragg peaks in the

event of inelastic scattering. The first observable Bragg peak in 60° specular reflection geometry occurs at a landing energy of 160eV. Furthermore, the 2dfit evaluation is only reasonable for the HMA measurement, since a constant energy resolution is required. In the TOF IVLEED measurement, the broadening of the elastic peak would lead to significant distortions in the loss IV curves.
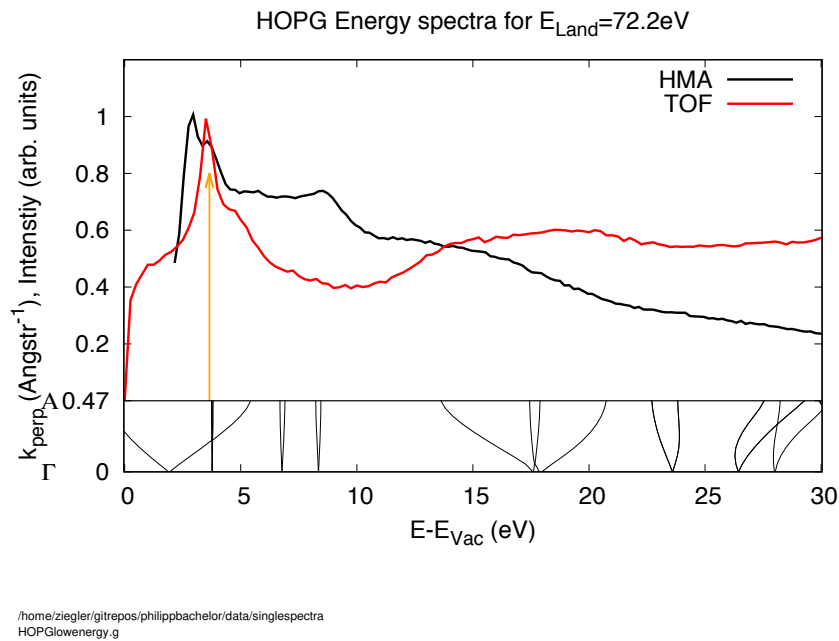
5.3.2 Secondary electrons

/home/ziegler/gitrepos/philippbachelor/data/singlespectra
HOPGlowenergy.g

Figure 40: Low energy spectra of HOPG at E_{Land}=72.2eV in 30° (red) and 60° (black) angle of incidence compared to the band structure along ΓA. Yellow arrow indicates peaks in red curve at 3.7eV.

In this chapter the effects concerning the secondary electron emission (SEE) are discussed on the basis of the IVLEED data. The SEE is directly linked to the band structure above the vacuum level, since secondary electrons must occupy an allowed band before they can leave the solid. The measured SEE depends on the angle between the detector and the surface of the sample, as this sets the direction within the band structure [54, 55]. Hence, the TOF and HMA measurements differ in their secondary electron energy distribution. The measurements have been made in specular reflection geometry, so the analyser and electron source include the same angle to the sample. In figure 40 two secondary electron spectra of HOPG at a landing energy of 72eV are shown and compared with the ΓA band structure. In the TOF spectrum (red) curve it is shown that the intensity decreases strongly in the band gap, indicating that allowed states do not exist for

secondary electrons. The yellow arrow indicates the position of the sharp peak at 3.7eV. In general, a causal link between the secondary electrons and the band structure is difficult to establish. However, very recently, the origin for the yellow marked peak was found in Reference [53]. Plasmon induced symmetry breaking causes a hybridisation of an interlayer state with an atom-like state, leading to the emission of secondary electrons with well defined energies and almost no dispersion. Since this SE generation mechanism is a novelty, it will be discussed in more detail in the following section. In the HMA spectrum (black curve), an additional peak can be observed at 8eV, whose origin probably stems from the band structure along non-high-symmetry axes. Because of the large exit angle of 60° in the HMA measurement, a direct comparison to the ΓA band structure can be misleading. In the IVLEED spectra (see figures 34 and 36) secondary electron features can be identified as horizontal stripes at $E - E_{Vac} = 3.7$eV and 17eV, as the energy of their final state is independent on the landing energy.

Figure 41 shows a secondary electron spectrum (blue) and a total electron yield (TEY) curve (green; see chapter 5.2 for more information of this curve) and compares them with the ΓA band structure. The position of the first yellow arrow is given with 3.7eV, which is in very good correspondence with the intersection of two bands. One of the bands has almost no dispersion, similar to bound electrons in atoms and thus this band is referred to as atom-like band. Electrons in atom-like states are localised in space and have a high density of states (DOS), implying that it is a favoured state for initially bound electrons. The second band is a so called interlayer state (I.S.). Stacking two or more graphene layers on top gives rise to interlayer states in which electrons can move quasi freely between atomic layers. I.S. are highly dispersive between layers (c-axis of the crystal) and are very transmissive for external electrons. Hence, electrons in interlayer states couple well to vacuum wave functions of incoming electrons. Electrons in such mulit-quantum well states behave similarly to light in a Fabry-Pérot interferometer.

If a $\pi + \sigma$ plasmon is excited by an incoming primary electron, the symmetry of the one-electron band structure breaks and a hybridisation occurs between the overlapping interlayer state and atom-like state. In figure 41b it is shown how the transmission T changes due to the symmetry breaking. The hybrid state combines the properties of both bands. This state has a high density of states from the flat atom-like band, making it a preferred final state, and it possesses the high mobility of the interlayer state which permits coupling to vacuum and consequently the emission of electrons. Thus, the hybridisation leads to a favorable final state with high mobility, resulting a non-dispersive peak. Werner

et al. predicted that a similar process leads to a peak at the second yellow arrow ($E - E_{Vac}$=17eV). Since the energy of the hybrid state is given by the overlapping bands in the electronic band structure, the peak is independent from the landing energy. Therefore, the secondary electron peaks can be observed as horizontal stripes in the IVLEED data (figures 34 and 36). The 3.7eV stripes is observable for landing energy greater than 25eV, which corresponds well to the excitation energy of the $\pi + \sigma$ plasmon.

5.3.3 Atypical Peak

In the previous subchapter it was shown that secondary electron effects are characterised by a fixed final state. Figure 42 shows a zoomed-in section of the HMA IVLEED data (see figure 34). One can observe a horizontal stripe around $E - E_{Vac}$=28eV, implying the existence of a favorable final state for secondary electrons. However, this peak seems to disappear for higher landing energies, which is untypical for true secondary electron effects, since SE features remain constant throughout the entire range of landing energies. Owing to this behaviour, it is referred to as "atypical peak". Figure 43 illustrates how the peak emerges from the π plasmon. In the REELS spectra for $E_{Land} > 37$eV (light blue) it can be observed that the π plasmon peak starts to become asymmetric and for even higher landing energies a distinct peak will form at around $E - E_{Vac} = 28$eV.

Figure 44 shows a landing energy spectrum (LES) at $E - E_{Vac} = 29$eV and compares it to several REELS spectra from the HMA IVLEED data(see figure 42). The vertical arrows indicate the position of the atypical peak in the REELS spectra and point to the LES curve. It is shown that discrete energy losses (such as the π plasmon at $E_{Loss} = 6$eV) remain in the same position in all REELS spectra, whereas the atypical peak shifts as a function of the landing energy. Furthermore, the atypical peak is difficult to identify as an independent peak in REELS spectra with $E_{Land} >$55eV, as the signal becomes too noisy in this region. This graph also shows a curve for the diferential inverse inelastic mean free path (DIIMFP) (primary energy $E = 55$eV) which is related to the energy loss function and was calculated from empirical optical data using the Penn model. In essence, the DIIMFP indicates the probability of suffering a certain energy loss.

Figure 45 shows the LES at $E - E_{Vac} = 29$eV from the HMA IVLEED spectrum (figure 42) and compares it to two DIIMFP curves for primary energies of 55 and 160eV. It can be observed that the strange peak does not have a step-like decrease in intensity, as suggested in the IVLEED spectrum (figure 42) but that it is rather an exponential decrease. The LES shows that the Atypical Peak and the
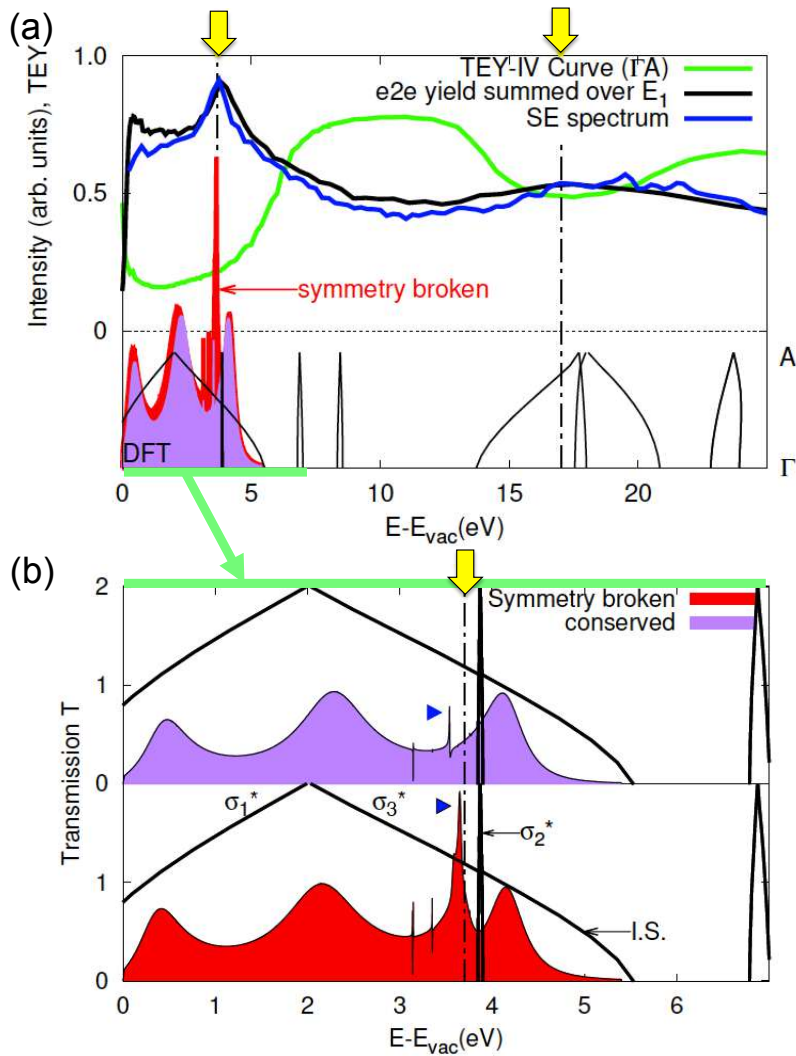
Figure 41: (a) shows a secondary electron energy spectrum (blue) and the total electron yield (TEY) curve from Bellissimo [28]. The yellow arrows indicate the peak maximum at $E - E_{Vac}$=3.7eV and 17eV. Purple area shows the theoretical total transmission of the graphite surface without symmetry breaking, whereas the red area shows it with the symmetry broken. (b) enlarged section. At the blue triangles a sharp peak with very high transmission develops in the broken symmetry case. This graph was originally published in [53].
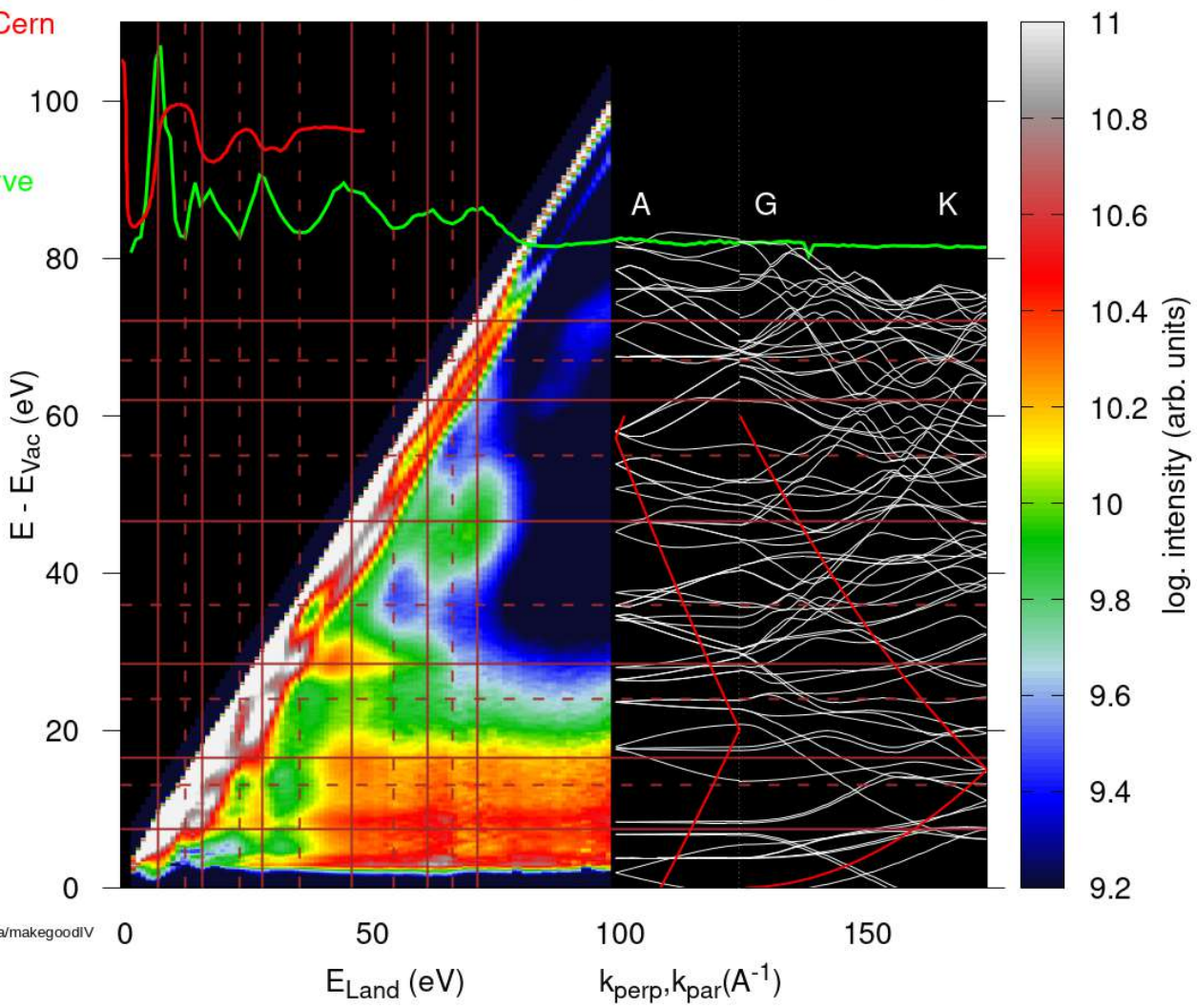
Figure 42: Result of IVLEED measurement of HOPG with HMA in 60° specular reflection on 8th Aug.2019. Same graph as in figure 34 but zoomed in lower landing energies to highlight the strange peak.
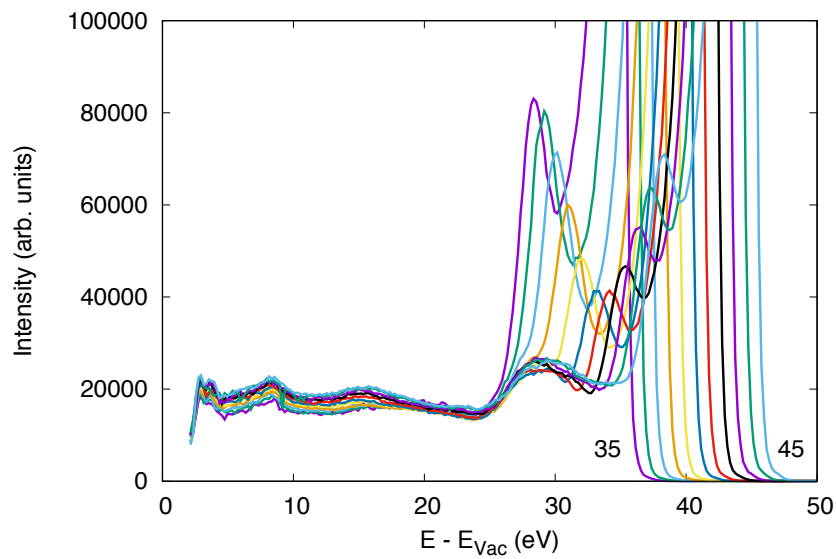
/home/ziegler/gitrepos/philippbachelor/data/Bragg$_6$0$_H$opg/0809/REELS
28eVpeak0809.g

Figure 43: HOPG REELS spectra of in 60° specular reflection at landing energies ranging from 35eV to 45eV. True secondary electron peaks in the region bellow 20eV appear at fixed energies, where as the π plasmon follows the elastic peak (cut off). Atypical peak evolves from π plasmon and stays at fixed energy about $E - E_{Vac}$=29eV.
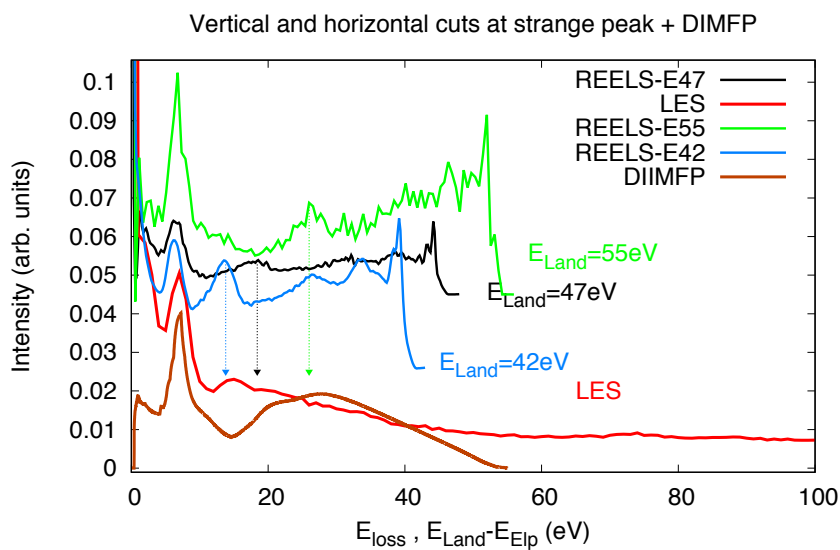
Figure 44: Comparison of various REELS spectra with a LES at $E - E_{Vac} = 29$eV and a calculated DIIMFP curve for primary energy E=55eV. The coloured arrows indicate the position of the strange peak in the REELS spectra and point to the LES curve. The energy scale of the LES is chosen in such a way that the elastic peak corresponds to 0eV.

DIIMFP curve exhibit roughly identical behaviour. This suggests that the atypical peak originates from primary electrons that suffer a specific energy loss to reach this favoured final state. At higher landing energies, the probability of suffering sufficiently high losses is too low to exist as an independent peak (as indicated by the DIIMFP). At an energy loss of about 55eV (corresponding to E_{Land}=84eV), the limit of the atypical peak is defined.

The origin of this strange peak is not yet fully understood, as it is a novel and still a largely unexplored phenomenon. However, the comparison of the horizontal cut with the DIIMFP shows that the occurrence of the peak is related to the appearance of the $\pi + \sigma$ plasmon. The DIIMFP curves show that the width of the plasmon roughly corresponds to the width of the strange peak. However, this relation alone does not result in the formation of a peak at constant energy. For this to happen, a preferred final state must exist within the band structure, which will be occupied by either inelastically scattered primary electrons or highly excited secondary electron. A primary electron would have to lose just enough energy to occupy this state with fixed energy, and therefore energy loss must be a function of landing energy. Somehow this specific inelastic event must be preferred over other types of inelastic scattering. If this peak stems from highly excited secondary electrons, the primary electron must thereby transfer almost all of its energy to a bound solid state electron. Whether this state is occupied by "captured" primary electrons or by highly excited secondary electrons cannot be determined. Similar strange peaks are also observed at about $E - E_{Vac}$=45eV and 70eV. Whether this process is a process similar to the 29eV strange peak is not yet clear and therefore, it offers a promising avenue for continuing research.

5.3.4 Sharp transition: band structure - Bragg-like

The last aspect discussed is the abrupt transition in the HMA IVLEED data of figure 34 between the $E - E_{Land}$ <100eV and the >100eV region. In the region $E_{Land} < 100$eV, on can observe several characteristic inelastic scattering and secondary electron features, for instance the atypical peak and secondary electron peaks. However, at higher landing energies, almost no inelastic intensity was measured. Also, there is a significant drop in intensity in the IV curve at $E_{Land} = 100$eV. This indicates that a sharp transition occurs between the low energy range, where the electronic band structure of the solid dominates the intensity and at higher energies, the Bragg-like region where electrons form constructive and destructive interference patterns on the atomic lattice. A physical explanation for the sharp transition remains unclear and subsequent experimental and theoretical research is suggested.
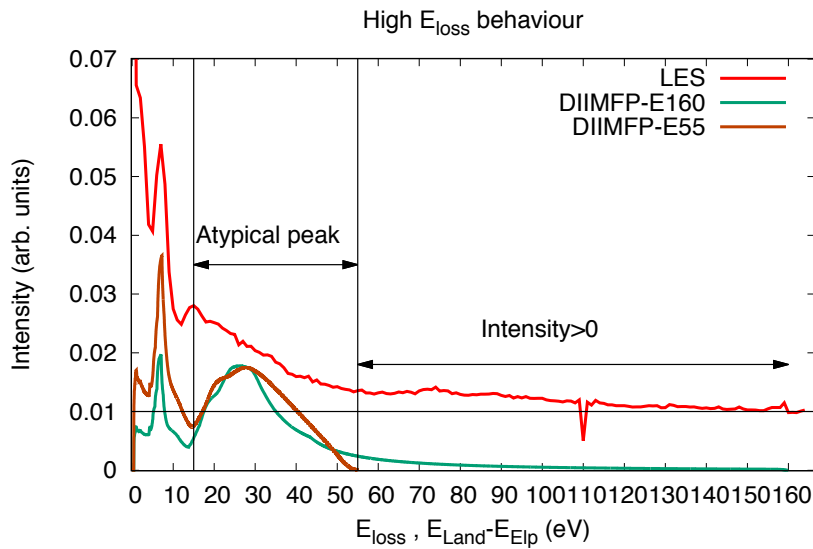
Figure 45: Comparison of a LES at $E - E_{Vac} = 29eV$ with two DIIMFP curves for primary energies of 55eV and 160eV. The horizontal line indicates the asymptotic behaviour of the atypical peak in the LES.

6 Conclusion

The main goal of this work was to investigate the unoccupied band structure of highly oriented pyrolytic graphite using inelastic very low energy electron diffraction (IVLEED) experiments. The investigation of the elastic peak intensities created a qualitative picture, which explains how far external electrons are allowed to propagate inside a solid. A model based on the matching formalism was created to understand the coupling between the wave functions of primary electrons in vacuum and inside the crystal. Furthermore, it was shown external electrons can indeed enter into the crystal at energies where Bloch states are forbidden, despite their wave function being strongly damped. This work provides convincing experimental data of the effects predicted by the wave function matching formalism by Slater [33]. In numerous works, the real component of the inner potential has been determined, for instance by Bragg scattering experiments [27], but with our data, the imaginary component of the inner potential is also revealed. The experimental data showed good agreement with the theoretical model.

IVLEED measurements allow one to measure full double differential energy spectra and therefore, this technique can be used to investigate Bragg diffraction

patterns for elastically as well as for inelastically scattered electrons. In this work, two models where used to predict the diffraction maxima for inelastically diffracted electrons. The theoretical models were able to predict diffraction maxima in a way that is consistent with existing experimental and theoretical studies [1–5]. Although this work aimed to provide data to validate the present models, the acquired data was not suited for this purpose, since the investigated energy range was too low.

This work revealed a novel type of electron emission at constant energy. For this to happen, a preferred final state must exist within the band structure, which will be occupied by either inelastically scattered primary electrons or highly excited secondary electron. A primary electron would have to lose just enough energy to occupy this state with fixed energy, and therefore energy loss must be a function of landing energy. Somehow this specific inelastic event must be preferred over other types of inelastic scattering. If this peak stems from highly excited secondary electrons, the primary electron must thereby transfer almost all of its energy to a bound solid state electron. Whether this state is occupied by "captured" primary electrons or by highly excited secondary electrons remained unclear. For further research it may be suggested to include negatively biased samples. A bias voltage would shift the Fermi level of the target (see chapter 4.2 for details). Therefore, features which stem from the electronic band structure shift in the REELS spectra, whereas the elastic peak and discrete losses would remain at the same energy. Consequently, one can distinguish between true primary electrons (elastic peak and discrete energy losses) and true band structure effects. Furthermore,

In summary, this work covered many different aspects concerning the unoccupied band structure above the vacuum level and provided plenty of ideas and starting points for further research. For instance, measuring IVLEED data for higher energies could validate the models for inelastic diffraction, created in this work. Furthermore, the novel and atypical peak offers countless possible directions of subsequent studies, for instance via e,2e coincidence spectroscopy, which allows one to fully measure momentum and energy of initial and final state of electrons.

References

[1] A. Ruocco et al. "Scattering mechanism of electrons interacting with surfaces in specular reflection geometry: Graphite". In: *Phys. Rev. B* 59 (20 May 1999), pp. 13359–13364. DOI: 10.1103/PhysRevB.59.13359. URL: https://link.aps.org/doi/10.1103/PhysRevB.59.13359.

[2] C. B. Duke and G. E. Laramore. "Quantum Field Theory of Inelastic Diffraction. I. Low-Order Perturbation Theory". In: *Physical Review B* 3.10 (May 1971), pp. 3183–3197. DOI: 10.1103/physrevb.3.3183. URL: https://doi.org/10.1103/physrevb.3.3183.

[3] G. E. Laramore and C. B. Duke. "Quantum Field Theory of Inelastic Diffraction. II. Two-Step Inelastic Diffraction". In: *Physical Review B* 3.10 (May 1971), pp. 3198–3213. DOI: 10.1103/physrevb.3.3198. URL: https://doi.org/10.1103/physrevb.3.3198.

[4] C. B. Duke and U. Landman. "Quantum Field Theory of Inelastic Diffraction. III. Dynamical Theory". In: *Physical Review B* 6.8 (Oct. 1972), pp. 2956–2967. DOI: 10.1103/physrevb.6.2956. URL: https://doi.org/10.1103/physrevb.6.2956.

[5] C. B. Duke and U. Landman. "Quantum Field Theory of Inelastic Diffraction. IV. Applications to Al(100) and Al(111)". In: *Physical Review B* 6.8 (Oct. 1972), pp. 2968–2977. DOI: 10.1103/physrevb.6.2968. URL: https://doi.org/10.1103/physrevb.6.2968.

[6] Pulickel Ajayan, Philip Kim, and Kaustav Banerjee. "Two-dimensional van der Waals materials". In: *Phys. Today* (2016).

[7] Christian Lotze. "Fundamental Processes in Single Molecule Junctions". PhD thesis. 2014. DOI: 10.17169/REFUBIUM-11283. URL: https://refubium.fu-berlin.de/handle/fub188/7084.

[8] O Pellegrino et al. "Oligothiophene films under electron irradiation: electron mobility and contact potentials". In: *Materials Science and Engineering: C* 22.2 (Dec. 2002), pp. 367–372. DOI: 10.1016/s0928-4931(02)00207-2. URL: https://doi.org/10.1016/s0928-4931(02)00207-2.

[9] J Lowell. "Contact electrification of metals". In: *Journal of Physics D: Applied Physics* 8.1 (Jan. 1975), pp. 53–63. DOI: 10.1088/0022-3727/8/1/013. URL: https://doi.org/10.1088/0022-3727/8/1/013.

[10] Jacques Cazaux. "Reflectivity of very low energy electrons (¡ 10 eV) from solid surfaces: Physical and instrumental aspects". In: *Journal of Applied Physics* 111.6 (2012), p. 064903. DOI: 10.1063/1.3691956. eprint: https://doi.org/10.1063/1.3691956. URL: https://doi.org/10.1063/1.3691956.

[11] M. Liehr et al. "Characterization of insulators by high-resolution electron-energy-loss spectroscopy: Application of a surface-potential stabilization technique". In: *Phys. Rev. B* 33 (8 1986), pp. 5682–5697. DOI: 10.1103/PhysRevB.33.5682. URL: https://link.aps.org/doi/10.1103/PhysRevB.33.5682.

[12] Patrick T. McCarthy, Ronald G. Reifenberger, and Timothy S. Fisher. "Thermionic and Photo-Excited Electron Emission for Energy-Conversion Processes". In: *Frontiers in Energy Research* 2 (Dec. 2014). DOI: 10.3389/fenrg.2014.00054. URL: https://doi.org/10.3389/fenrg.2014.00054.

[13] Kishore Uppireddi et al. "Thermionic emission energy distribution from nanocrystalline diamond filmsfor direct thermal-electrical energy conversion applications". In: *Journal of apllied physics* 106 (2009), pp. 1475–1489. DOI: https://doi.org/10.1063/1.3204667.

[14] J. W. Gadzuk and E. W. Plummer. "Field Emission Energy Distribution (FEED)". In: *Reviews of Modern Physics* 45.3 (July 1973), pp. 487–548. DOI: 10.1103/revmodphys.45.487. URL: https://doi.org/10.1103/revmodphys.45.487.

[15] *Overview of Electron Microscopy, 1931-2000.* https://authors.library.caltech.edu/5456/1/hrst.mit.edu/hrs/materials/public/ElectronMicroscope/EM_HistOverview.htm. Accessed: 2022-01-10.

[16] *CLEAR study paves the way for novel electron-based cancer therapy.* https://home.cern/news/news/knowledge-sharing/clear-study-paves-way-novel-electron-based-cancer-therapy. Accessed: 2022-01-10.

[17] P. J. Ouseph et al. "Electron interaction with matter". In: *American Journal of Physics* 50.4 (Apr. 1982), pp. 341–343. DOI: 10.1119/1.13038. URL: https://doi.org/10.1119/1.13038.

[18] Ludwig Reimer. *Scanning Electron Microscopy.* Springer Berlin Heidelberg, 1998. DOI: 10.1007/978-3-540-38967-5. URL: https://doi.org/10.1007/978-3-540-38967-5.

[19] Michel A. Van Hove, William H. Weinberg, and Chi-Ming Chan. *Low-Energy Electron Diffraction*. Springer Berlin Heidelberg, 1986. DOI: 10 . 1007 / 978 – 3 – 642 – 82721 – 1. URL: https : / / doi . org / 10 . 1007 / 978 – 3 – 642 – 82721 – 1.

[20] C. Davisson and L. H. Germer. "Diffraction of Electrons by a Crystal of Nickel". In: *Physical Review* 30.6 (Dec. 1927), pp. 705–740. DOI: 10 . 1103 / physrev . 30 . 705. URL: https://doi.org/10.1103/physrev.30.705.

[21] H. Bethe. "Theorie der Beugung von Elektronen an Kristallen". In: *Annalen der Physik* 392.17 (1928), pp. 55–129. DOI: 10 . 1002 / andp . 19283921704. URL: https://doi.org/10.1002/andp.19283921704.

[22] E.E. Krasovskii. "The band structure theory of LEED and photoemission". In: Solid-State Photoemission and Related Methods. 2003, pp. 220–246. DOI: https://doi.org/10.1002/9783527602506.ch7.

[23] V. N. Strocov et al. "New Method for Absolute Band Structure Determination by Combining Photoemission with Very-Low-Energy Electron Diffraction: Application to Layered VSe2". In: *Phys. Rev. Lett.* 79 (3 1997), pp. 467–470. DOI: 10 . 1103 / PhysRevLett . 79 . 467. URL: https : //link.aps.org/doi/10.1103/PhysRevLett.79.467.

[24] V. Strocov. "Unoccupied Band Structure of Layered Materials by Very-Low-Energy Electron Diffraction: Implications in Photoemission". In: vol. 24. Apr. 2006, pp. 161–207. ISBN: 0-7923-6526-7. DOI: 10 . 1007 / 0 – 306 – 47126 – 4_4.

[25] Hans Lüth. *Solid Surfaces, Interfaces and Thin Films*. Springer Berlin Heidelberg, 2010. DOI: 10 . 1007 / 978 – 3 – 642 – 13592 – 7. URL: https : / / doi.org/10.1007/978-3-642-13592-7.

[26] D. Geelen et al. "Non-universal Transverse Electron Mean Free Path through Few-layer Graphene". In: *Phys. Rev. Lett. 123, 086802* (2019). URL: https://arxiv.org/abs/1904.13152.

[27] P. Ziegler. "Measurement of the inner potential of highly oriented pyrolytic graphite with differential inelastic very low energy electron diffraction measurements (Bachelor Thesis)". In: (2020).

[28] Alessandra Bellissimo et al. "Secondary electron generation mechanisms in carbon allotropes at low impact electron energies". In: *J Electron Spectrosc Relat Phenom* (2020). DOI: file:///home/ziegler/ownCloud/literatur/ 2020 _ secondary – electron – generation – mechanisms – in – c _ 2020 _ journal-of-electron-spect.pdf.

[29] Alessandra Bellissimo. *Multiparameter Analysis of Genesis and Evolution of Secondary Electrons produced in the Low Energy Regime*. Feb. 2019. DOI: 10.5281/zenodo.3924096. URL: https://doi.org/10.5281/zenodo.3924096.

[30] H. P. Hughes and H. I. Starnberg, eds. *Electron Spectroscopies Applied to Low-Dimensional Materials*. Springer Netherlands, 2000. DOI: 10.1007/0-306-47126-4. URL: https://doi.org/10.1007/0-306-47126-4.

[31] Wolfgang Schattke and Michel A. Van Hove, eds. *Solid-State Photoemission and Related Methods*. Wiley, Oct. 2003. DOI: 10.1002/9783527602506. URL: https://doi.org/10.1002/9783527602506.

[32] M. Lindroos, H. Pfnür, and D. Menzel. "Theoretical and experimental study of the unoccupied electronic band structure of Ru(001) by electron reflection". In: *Physical Review B* 33.10 (May 1986), pp. 6684–6693. DOI: 10.1103/physrevb.33.6684. URL: https://doi.org/10.1103/physrevb.33.6684.

[33] J. C. Slater. "Damped Electron Waves in Crystals". In: *Physical Review* 51.10 (May 1937), pp. 840–846. DOI: 10.1103/physrev.51.840. URL: https://doi.org/10.1103/physrev.51.840.

[34] J B Pendry. "The application of pseudopotentials to low-energy electron diffraction II: Calculation of the reflected intensities". In: *Journal of Physics C: Solid State Physics* 2.12 (1969), pp. 2273–2282. DOI: 10.1088/0022-3719/2/12/310. URL: https://doi.org/10.1088/0022-3719/2/12/310.

[35] G. Arduini et al. "High Luminosity LHC: challenges and plans". In: *Journal of Instrumentation* 11.12 (Dec. 2016), pp. C12081–C12081. DOI: 10.1088/1748-0221/11/12/c12081. URL: https://doi.org/10.1088/1748-0221/11/12/c12081.

[36] Alessandra Bellissimo et al. "Secondary electron generation mechanisms in carbon allotropes at low impact electron energies". In: *Journal of Electron Spectroscopy and Related Phenomena* 241 (2020). Sources, Interaction with Matter, Detection and Analysis of Low Energy Electrons (SIMDALEE2), p. 146883. ISSN: 0368-2048. DOI: https://doi.org/10.1016/j.elspec.2019.07.004. URL: https://www.sciencedirect.com/science/article/pii/S0368204819300039.

[37] Olga Yu. Ridzel, Vytautas Astašauskas, and Wolfgang S.M. Werner. "Low energy (1-100 eV) electron inelastic mean free path (IMFP) values determined from analysis of secondary electron yields (SEY) in the incident energy range of 0.1-10 keV". In: *Journal of Electron Spectroscopy and Related*

Phenomena 241 (May 2020), p. 146824. DOI: 10.1016/j.elspec.2019.02.003. URL: https://doi.org/10.1016/j.elspec.2019.02.003.

[38] D. Coello-Fiallos et al. "DFT comparison of structural and electronic properties of graphene and germanene: monolayer and bilayer systems". In: *Materials Today: Proceedings* 4.7 (2017), pp. 6835–6841. DOI: 10.1016/j.matpr.2017.07.011. URL: https://doi.org/10.1016/j.matpr.2017.07.011.

[39] Vytautas Astašauskas. "Emission of low energy electrons from solid surfaces studied by means of spectroscopy with individual as well as correlated electrons". In: 2019.

[40] N. David Mermin Neil W. Ashcroft. *Solid State Physics*. Sauder College Publishing, 1976. ISBN: 0030839939 (College Edition).

[41] J. Fiddler E. Bauer Ch. Eisenmenger-Sittner. *Materialwissenschaften für Technische Physiker*. Technische Universität Wien, 2017.

[42] John C. Turnbull and H. E. Farnsworth. "The Inelastic Scattering of Slow Electrons From a Silver Single Crystal". In: *Physical Review* 54.7 (Oct. 1938), pp. 509–514. DOI: 10.1103/physrev.54.509. URL: https://doi.org/10.1103/physrev.54.509.

[43] D. K. Saldin. "Angle-resolved electron-energy-loss spectroscopy: Atomic-core excitations at adsorbates on surfaces". In: *Physical Review Letters* 60.12 (Mar. 1988), pp. 1197–1200. DOI: 10.1103/physrevlett.60.1197. URL: https://doi.org/10.1103/physrevlett.60.1197.

[44] *momentum transfer resolved electron energy-loss spectroscopy*. https://www.jeol.co.jp. Accessed: 2021-10-09.

[45] Kimbal physics. "ELG-2 / EGPS-1022 ELECTRON GUN / POWER SUPPLY". In:

[46] László P Biró and Philippe Lambin. "Grain boundaries in graphene grown by chemical vapor deposition". In: *New Journal of Physics* 15.3 (Mar. 2013), p. 035024. DOI: 10.1088/1367-2630/15/3/035024. URL: https://doi.org/10.1088/1367-2630/15/3/035024.

[47] Gina Peschel. *Carbon-carbon bonds: Hybridization - physik.fu-berlin.de*. URL: https://www.physik.fu-berlin.de/einrichtungen/ag/ag-reich/lehre/Archiv/ss2011/docs/Gina_Peschel-Handout.pdf?ad=semD&an=msn_s&am=modifiedbroad&q=sp3+hybridization+carbon&o=29593&qsrc=999&l=sem&askid=0c06243d-f933-4c9f-ad7f-e545614b44f9-0-ab_msm.

[48] *The Hexagonal Graphite (A9) Crystal Structure.* `https://www.atomic-scale-physics.de/lattice/struk/a9.html`. Accessed: 2021-03-02.

[49] D. D. L. CHUNG. "Review Graphite". In: *Journal of material science* 37 (2002), pp. 1475–1489.

[50] D. Gray, A. McCaughan, and B. Mookerji. "Crystal Structure of Graphite , Graphene and Silicon". In: 2009.

[51] *The first Brillouin zone of a (simple) hexagonal lattice.* `http://lamp.tu-graz.ac.at/~hadley/ss1/bzones/hexagonal.php`. Accessed: 2022-02-20.

[52] Xiaoguang Luo et al. "Plasmons in graphene: Recent progress and applications". In: *Materials Science and Engineering: R: Reports* 74.11 (2013), pp. 351–376. ISSN: 0927-796X. DOI: `https://doi.org/10.1016/j.mser.2013.09.001`. URL: `https://www.sciencedirect.com/science/article/pii/S0927796X13000879`.

[53] Wolfgang S.M. Werner et al. "Secondary Electron Emission by Plasmon Induced Symmetry Breaking in Highly Oriented Pyrolitic Graphite (HOPG)". In: *Phys. Rev. Lett. 125, 196603* (2020). DOI: `10.1103/PhysRevLett.125.196603`.

[54] A.J. Dekker. "Secondary Electron Emission". In: *Advances in Research and Applications.* Ed. by Frederick Seitz and David Turnbull. Vol. 6. Solid State Physics. Academic Press, 1958, pp. 251–311. DOI: `https://doi.org/10.1016/S0081-1947(08)60728-6`. URL: `https://www.sciencedirect.com/science/article/pii/S0081194708607286`.

[55] Ding Zejun et al. "On the Energy Distribution of Secondary Electrons Emitted from Metals". In: *J Surf Anal* 15 (Jan. 2008). DOI: `10.1384/jsa.15.186`.

List of Figures

List of Tables

Appendices

A   2dfit and h2d Source code

```
//############# Find Elp: Maxiumum in range  E ~ E_land
    for(i=0;i<hist->nloss;i++){
        elpy[i]=0;
        elpx[i]=0;
    for (j=0;j<hist->nt;j++){
// printf("%f",hist->tscale[j]);
            if(hist->yield[i][j][0]>elpy[i]&& (hist->lossscale[i]*0.8 <=
    hist->tscale[j]) && ((hist->lossscale[i]*1.2) >= hist->tscale[j])){
            // if(hist->yield[i][j][0]>elpy[i]&& (hist->escale1[i]*0.8 <=
    hist->escale2[j]) && ((hist->escale1[i]*1.2) >= hist->escale2[j])){
            elpy[i]=hist->yield[i][j][0];
 // printf("\nIch bin hier: %f",hist->tscale[j]);
            elpx[i]=hist->escale2[j]  ;
            }
        }
        if(ipd.ilev>3){
            printf("Elastic Peak at (X/Y): %lf %lf \n",elpx[i],elpy[i]);
        }
    }
int maxk=50;
int k;
    for(k=0;k<maxk;k++){
        //Summe rel zum elp!!!!!!
//###############################
//###############################
//      2dfit
//###############################
//###############################

```

85

```
28          for(i=0;i<hist->nloss;i++){
29              sum[k][i]=0;
30              for (j=0;j<hist->nt;j++){
31                  if(hist->tscale[j] >= (elpx[i]-k) && hist->tscale[j]<=
    (elpx[i]-k+1)){
32                  //      if(hist->escale1[j] >= (elpx[i]-k) && hist->escale1[j
    ]<= (elpx[i]-k+1)){
33                      // if(hist->escale2[j] >= (elpx[i]-k) && hist->escale2[j
    ]<= (elpx[i]-k+1)){
34                      sum[k][i]+=hist->yield[i][j][0];
35                      //  printf("\nIch bin hier:  e1=%lf   loss=%lf  e2=%lf
    tsc=%lf",hist->escale1[i],hist->lossscale[i], hist->escale2[j],hist
    ->tscale[j]);
36                  }
37              }
38              if(ipd.ilev>3){
39                  printf("%d Sum from %lf   is: %lf \n",k,hist->lossscale[
    i] ,sum[k][i]);
40                  //printf("%d Sum from %lf   is: %lf \n",k,hist->escale1[
    i] ,sum[k][i]);
41              }
42          }
43 }
44 //################################
45 //################################
46 //       h2d
47 //################################
48 //################################
49
50 maxk=100;
51   for(k=0;k<maxk;k++){
52          for(i=0;i<hist->nloss;i++){
53              sum2[k][i]=0;
54              for (j=0;j<hist->nt;j++){
55              //printf("%d %lf %lf %lf %lf \n",j, hist->lossscale[j],
    hist->escale[j], hist->escale2[j],hist->tscale[j]);
56                  if(hist->tscale[j] >= (k) && hist->tscale[j]<= (k+1)){
57                  // if(hist->escale1[j] >= (k) && hist->escale1[j]<= (k
    +1)){
58                      // if(hist->escale2[j] >= (k) && hist->escale2[j]<= (k
    +1)){
59                      sum2[k][i]+=hist->yield[i][j][0];
60                  //  printf("\nIch bin hier:  e1=%lf   loss=%lf  e2=%lf   tsc
    =%lf",hist->escale1[j],hist->lossscale[i], hist->escale2[j],hist->
    tscale[j]);
61                  }
62              }
```

86

```
63            if(ipd.ilev>3){
64                printf("%d Sum from %lf   is: %lf \n",k,hist->lossscale[
   i]  ,sum2[k][i]);
65                //printf("%d Sum from %lf   is: %lf \n",k,hist->escale1[
   i]  ,sum2[k][i]);
66            }
67        }
68    }
```